An Alternative Blocking Layer for

Titanium Dioxide (TiO$_2$)

Solar Cell Applications

Dissertation

zur Erlangung des Grades

Doktor der Naturwissenschaften

Am Fachbereich Chemie Pharmazie und Geowissenschaften der

Johannes Gutenberg-Universität in Mainz

Mine Memeşa

geboren in Bursa, Türkei

Mainz (2008)

II

Zusammenfassung

In hybrid-organischen Solarzellen ist zwischen der transparenten Elektrode und nanokristallinen Titania-Partikeln eine Barriereschicht erforderlich, um elektrische Kurzschlüsse sowie auftretenden Stromverluste aufgrund von Rekombination an der Elektrodenoberfläche zu vermeiden. In der vorliegenden Arbeit wird die Herstellung einer hybriden Barriereschicht vorgestellt, die aus leitfähigen Titania-Nano-Partikeln in einer isolierenden polymer-abgeleiteten Keramic besteht. Die Barriereschicht wird durch Sol-Gel-Chemie präpariert, wobei ein amphiphiles Blockcopolymer als Templat fungiert. Hierzu wurde ein neuartiges Polydimethylsiloxan, das das amphiphile Blockcopolymer Poly(ethylenglycol)methylethermethacrylat-block-poly(dimethylsiloxane)-block-poly(ethylenglycol)methylethermethacrylat synthetisiert. Durch Plasmabehandlung wurde die Titania-Schicht vom Polymer entfernt. Tempern bei 450°C unter Stickstoff führte zu Anatas zusammen mit einer aus dem PDMS Block abgeleiteten Silizium-Oxycarbid-Keramik. Elektrische Charakterisierung der Leitfähigkeit durch Rastersondenmikroskopie zeigte ein perkolierendes Titania-Netzwerk, das durch eine isolierende Keramic-Matrix getrennt ist. Rastersonden-Kelvin-Kraftmikroskopie zeigte die Existenz von Titania-Partikeln auf der Oberfläche, welche somit eine breite Fläche zur Farbstoffaufnahme bereitstellt. Die einheitlichkeit der perkolierender Strukturen wurde durch "Microbeam Grazing Incidence Small Angle X-Ray Scattering" nachgewiesen. Die ersten Anwendungen an hybriden organischen Solarzellen haben gegenüber den konventionellen Anwendungen mit einer blokierenden Schichten von Titanium-Dioxide eine 15-fache Effizienzsteigerung erreicht.

Poly(dimethylsiloxan)-block-poly(ethylenglycol)methylethermethacrylat und poly(ethylene-oxid)-poly(dimethylsiloxan) methyl methacrylat diblock copolymere wurden ebenso synthetisiert. Ihre Titania-Nanocomposit-Schichten wurden mit der integrierten blokierenden Schicht verglichen. Die Blockcopolymere, welche einen linearen Poly(Ethylenoxid) Block enthielten ergaben dabei stark geordnete schaum-ähnliche Strukturen.

Der Einfluss der Temperatursteigerung bis zu 600°C und 1000°C auf die Morphologie von Titania wurde durch Rasterelektronenmikroskopie und Rasterkraftmikroskopie sowie durch Röntgenstreuung untersucht. Sol-gel-Gehalt, sowie Säure, Titania-Präkursor und Triblock-Copolymer gehalt wurden dabei variiert, um deren Einfluss auf die Titania-Morphologie zu beobachten. Durch Erhöhung des Polymergehalts wurden Titania-Partikel mit Durchmesser von 15-20 nm gebildet.

Abstract

In hybrid organic solar cells a blocking layer between transparent electrode and nanocrystalline titania particles is essential to prevent short-circuiting and current loss through recombination at the electrode interface.

Here the preparation of a uniform hybrid blocking layer which is composed of conducting titania nanoparticles embedded in an insulating polymer derived ceramic is presented. This blocking layer is prepared by sol-gel chemistry where an amphiphilic block copolymer is used as a templating agent. A novel poly(dimethylsiloxane) containing amphiphilic block copolymer poly(ethyleneglycol)methylethermethacrylate-block-poly(dimethylsiloxane)-block-poly(ethyleneglycol)methylethermethacrylate has been synthesized to act as the templating agent. Plasma treatment uncovered titania surface from any polymer. Annealing at 450°C under nitrogen resulted in anatase titania with polymer derived silicon oxycarbide ceramic. Electrical characterization by conductive scanning probe microscopy experiments revealed a percolating titania network separated by an insulating ceramic matrix. Scanning Kelvin probe force microscopy showed predominant presence of titania particles on the surface creating a large surface area for dye absorption. The uniformity of the percolating structures was proven by microbeam grazing incidence small angle x-ray scattering. First applications in hybrid organic solar cells in comparison with conventional titanium dioxide blocking layer containing devices revealed 15 fold increases in corresponding efficiencies.

Poly(dimethylsiloxane)-block-poly(ethyleneglycol)methylethermethacrylate and poly(ethyleneoxide)-poly(dimethylsiloxane)methylmethacrylate diblock copolymers were also synthesized. Their titania nanocomposite films were compared with the integrated blocking layer. Liner poly(ethyleneoxide) containing diblock copolymer resulted in highly ordered foam like structures.

The effect of heating temperature rise to 600°C and 1000°C on titania morphology was investigated by scanning electron and force microscopy and x-ray scattering. Sol-gel contents, hydrochloric acid, titania precursor and amphiphilic triblock copolymer were altered to see their effect on titania morphology. Increase in block copolymer content resulted in titania particles of diameter 15-20 nm.

Table of Contents

Abbreviations and Symbols

ITO	Indium tin oxide
FTO	Fluorine doped tin oxide
SnO_2	Tin oxide
TiO_2	Titanium dioxide
PDMS	Poly(dimethylsiloxane)
PS-PEO	Poly(styrene)-block-poly(ethyleneoxide)
SiOC	Silicon oxycarbide
χ	Flory-Huggins segment-segment interaction parameter
k_B	Boltzmann constant
ε_{AB}	Interaction energy per monomer units between A and B monomers
Z	Number of nearest neighbor monomers to a copolymer configuration
r_{AB}	Segment-segment separation
α	Segment polarizability
I	Ionization potential
H	Enthalpy
S	Entropy
G	Gibbs free energy
N	Total degree of polymerization
V	Segment volume
ρ	Polymer density
M	Polymer molecular weight
f	Volume fraction of a component in a block copolymer
R_g	Radius of gyration

ODT	Order to disorder transition
PS-PI	Poly(styrene)-block-poly(isoprene)
τ	Symmetry parameter
PRE	Persistent radical effect
ATRP	Atom transfer radical polymerization
k_{act}	Rate constant of activation
k_{deact}	Rate constant of deactivation
k_t	Rate constant of termination
k_p	Rate constant of propagation
THF	Tetrahydrofuran
BuLi	Butyllithium
DPE	1,1-diphenylethylene
TEA	Triethylamine
CuBr	Copper bromide
PMDETA	N,N,N',N',N''-pentamethyldiethylenetriamine
TTIP	Titanium(IV) tetraisopropoxide
HCl	Hydrochloric acid
(PEO)MA	Poly(ethyleneglycolmethylethermethacrylate)
Al_2O_3	Aluminum oxide
$CDCl_3$	Diteuriated chloroform
NMR	Nuclear Magnetic Resonance
^{1}H-NMR	Proton NMR
GPC	Gel permeation chromatography
DSC	Differential scanning calorimetry

TGA	Thermal gravimetric analysis
DLS	Dynamic light scattering
HPLC	High performance liquid chromatography
SEM	Scanning electron microscopy
TEM	Transmission electron microscopy
SFM	Scanning force microscopy
SKPM	Scanning Kelvin probe microscopy
CPM	Conductive probe scanning force microscopy
FIB	Focused ion beam
WAXS	Wide angle X-ray scattering
SAXS	Small angle X-ray scattering
GISAXS	Grazing incidence small angle X-ray scattering
μGISAXS	Microbeam grazing incidence small angle X-ray scattering
CPD	Contact potential difference
ac	Alternating current
dc	Direct current
NBS	N-hydroxysuccinimidyl
PEDOT:PSS	Poly(3,4-ethylenedioxythiophene)poly(styrenesulfonate)
PEO-MA(PDMS)	Poly(ethyleneoxide)-poly(dimethylsiloxane)methylmethacrylate
PDMS-MA(PEO)	Poly(dimethylsiloxane)-block-poly(ethyleneglycol)methylethermethacrylate
(PEO)MA-PDMS-MA(PEO)	Poly(ethyleneglycolmethylethermethacrylate)-block-poly(dimethylsiloxane)-block- poly(ethyleneglycolmethacrylate)

1   Introduction

In an organic solar cell, the photoactive layer is sandwiched between two dissimilar electrodes with different work functions. One of these electrodes needs to be transparent for light transmission. An electron-hole pair is generated by optical excitation, followed by subsequent dissociation and collection at electrodes. Charge carrier pathways are key factor in the performance of solar cells[1-3]. Dye-sensitized titanium dioxide solar cells developed by Grätzel et. al.[1] where liquid electrolyte is used for charge transport are among the most efficient organic solar cells[4]. However the presence of liquid electrolyte as the charge transport medium creates sealing problems which motivated the research for an alternative hole transporting media. As alternative solutions conjugated p-type polymers, hole transport compounds with triarylamine structural unit, low molecular weight spiro-compounds or inorganic p-type semiconductors are tested instead of the liquid electrolyte as charge transport medium to prepare solid state solar cells[5-10]. Sealing problems were solved by switching to the solid state. However the short circuiting and current loss through recombination at the interface between the transparent electrode and the hole transport medium resulted in intrinsically inefficient solar cells. FTO [F doped tin oxide (SnO_2)] or indium tin oxide (ITO) are commonly used as transparent anodes for organic solar cells. Both ITO and FTO surfaces show the characteristic morphology of tin oxide crystals. The electronic properties of ITO/FTO depend on the preparation and cleaning methods employed[11]. The ITO/FTO roughness increases the probability of having short circuits. ITO/FTO acts as an oxygen and metal ion source with direct contact of a photoactive polymer[12]. In order to minimize these effects Grätzel and co-workers put an additional compact layer of TiO_2 between FTO and nanocrystalline TiO_2 layer[8]. There had been attempts to replace FTO and they were not very succesfull[13]. Recently, graphite was used to replace FTO[14]. Although it seemed promising for solar device applications, use of a blocking layer was inevitable because of the ohmic contact formed, which means that the charge carriers will recombine at the interface between graphite and hole conducting material. The blocking layer in between the nanocrystalline TiO_2 layer and the FTO electrode increased the current output to three to four orders of magnitude. Suppression of electron leakage at the interface of ITO/FTO and TiO_2 nanoparticles plays an important role in the improvement of electron conversion efficiency, especially in the increase of the open circuit voltage of the organic-inorganic hybrid solar cells[15]. The blocking layer in solid state dye sensitized solar cells is unavoidable at the moment. Moreover, it needs to be of an optimum thickness. A too thin barrier layer gives rise to the possibility of cracking thus

electrical shorts, while too thick barrier layer increases the series resistance thereby reduces the photocurrent amplitude and fill factor[16]. Schematic representation of a prototype dye sensitized hybrid organic solar cell is shown in Scheme 1.1.
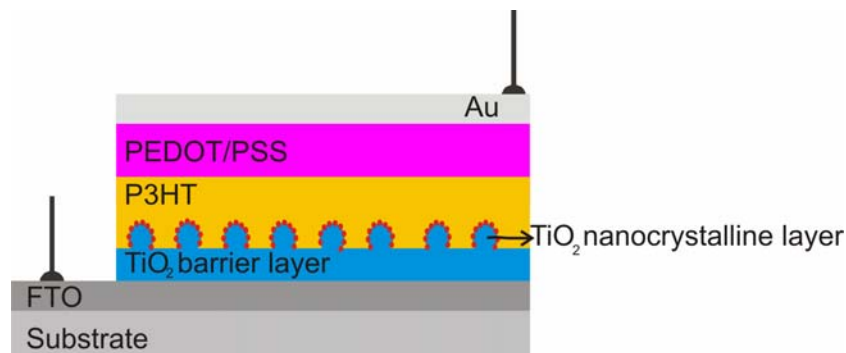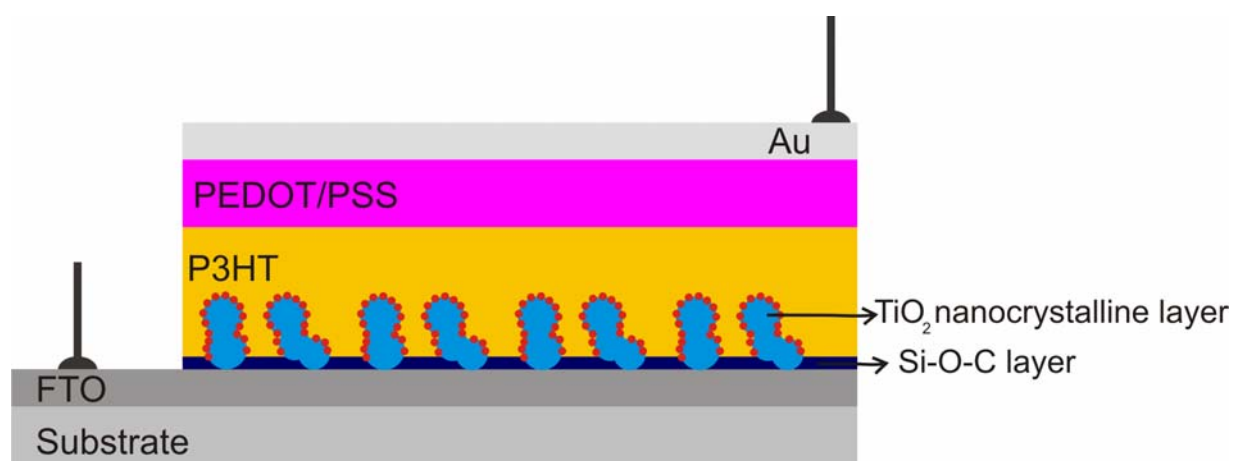

Scheme 1.1. *Schematic representation of a prototype dye sensitized solar cell.*

TiO_2 thin films are currently subject to great interest due to their potential applications such as sensors, photocatalysts, and optical coatings due to their high dielectric constant, high refractive index and good optical transmittance[17-19]. Moreover, incorporation of nanostructured inorganic semiconductors as electron transporting material into organic solar cells has attracted growing interest due to promising high efficiencies. A wide band gap oxide semiconductor TiO_2 (3.2 eV for the anatase polymorph of TiO_2) has been the most widely studied one among the electron transporting metal oxides in hybrid photovoltaics[20, 21]. Ordered TiO_2 nanocrystals are present over a compact TiO_2 barrier layer as seen in Scheme 1.1. The morphology of the nanocrystalline TiO_2 layer greatly influences the efficiency of the devices[22]. Hence, the preparation of the nanostructured TiO_2 thin films has gained special significance[23]. Mesoporous metal alkoxides are prepared with controlled morphology by using amphiphilic block copolymers as templating agents in combination with sol-gel chemistry[24, 25]. This strategy was also extended to the preparation of titania nanoparticles with poly (styrene)-block-poly (ethylene oxide) (PS-b-PEO) amphiphilic block copolymer as the structure directing agent[23, 26, 27]. The titania precursor reacts with the PEO in the sol-gel, and during a heating step PEO decomposes leaving anatase titania behind.

Poly (dimethylsiloxane) (PDMS), $[-Si(CH_3)_2O-]_n$, is the most widely investigated and commercially applied siloxane polymer due to its low surface tension, low glass transition and melting temperatures[28]. Furthermore, PDMS is one of polymeric precursors of the general

formula ($R_xSi(OR`)_{4-x}$) containing Si-C bonds. This Si-C bond is present from the beginning in the sol-gel processes and preserved in the glass structures. These silicon oxy-carbide gels were heat treated to intermediate temperatures to obtain silicon oxy-carbide (Si-O-C) glasses[29]. The latter property makes PDMS a promising alternative to prevent short circuits by building an insulating layer between the hole conducting polymer and the transparent anode, across the ordered TiO_2 nanoparticles in hybrid organic solar cells. This is illustrated in Scheme 1.2.

Scheme 1.2. Schematic representation of the prototype hybrid organic solar prepared by proposed blocking layer. SiOC layer is drawn not to scale.

The ability of PDMS to turn into Si-O-C after being heated to elevated temperatures and well established synthesis of titania nanoparticles via sol-gel chemistry using an amphiphilic block copolymer as the templating agent are combined through synthesis of a PDMS containing amphiphilic block copolymer. Poly (ethyleneglycol) methyl ether methacrylate-block-PDMS-block-poly (ethyleneglycol) methyl ether methacrylate [(PEO)MA-PDMS-MA(PEO)] triblock copolymer was synthesized for this purpose. In this way, conventional TiO_2 compact blocking layer can be replaced by our titania/(PEO)MA-PDMS-MA(PEO) hybrid blocking layer.

In this PhD thesis, we tried to prove if we can replace the conventional compact TiO_2 blocking layer by combining the insulation property of PDMS after annealing, with the sol-gel chemistry in titania nanoparticle preparation. "PDMS"-"PEO" containing block copolymer synthesis constitutes the starting point. The theory of block copolymer phase

separation and block copolymer synthesis is explained in Chapter 2. The experimental techniques with their working principles and corresponding instruments are presented in Chapter 3. Chapter 4 starts with the synthesis trials which did not work and continues with synthesis of (PEO)MA-PDMS-MA(PEO) triblock copolymer followed by the synthesis of PDMS-MA(PEO) and PEO-MA(PDMS) diblock copolymers. The explanation of an integrated blocking layer preparation with testing of the plasma etching step is given in Chapter 5. This is followed by integrated blocking layer preparation as the titania/(PEO)MA-PDMS-MA(PEO) nanocomposite films with their electrical and morphological characterization. Effect of sol-gel components on titania morphology in titania/(PEO)MA-PDMS-MA(PEO) nanocomposite films and characterization of nanocomposite films prepared from diblock copolymers are also presented in the same chapter. In Chapter 6, solid state hybrid organic solar cells and their working principle are explained. The device application by titania/(PEO)MA-PDMS-MA(PEO) nanocomposite films and their efficiency measurements are compared with conventional TiO_2 blocking layer containing devices. Summary of all the presented work and related outlook are given in Chapter 7.

2 Theory

2.1 Block copolymer phase separation

Block copolymers are made by covalent bonding of two or more polymeric chains which are in most cases thermodynamically incompatible. This incompatibility results in a variety of microstructures in bulk and in solution. These microstructures are in the order of the size of the block copolymers, thus related to their physical and chemical properties[30].

Block copolymers from two different monomers can form linear block copolymers, graft block copolymers and star block copolymers as depicted in Scheme 2.1, taken from Ref.31.
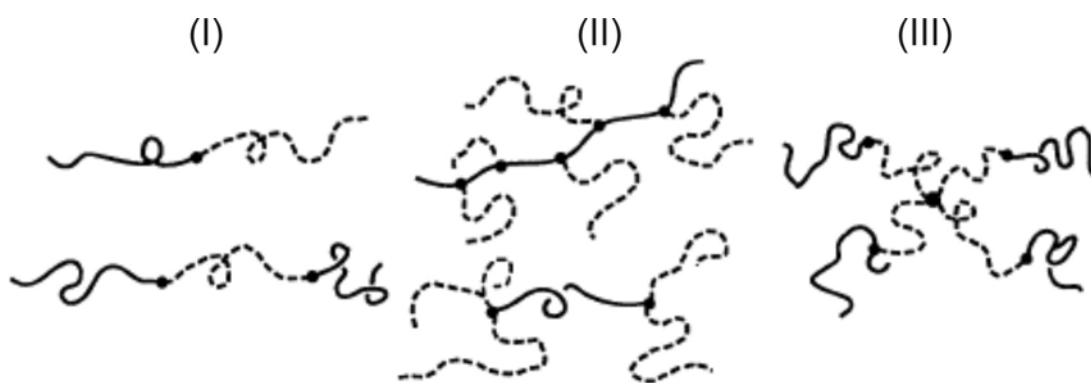
Scheme 2.1. *Schematic representation of block copolymer types: (I)linear (II)graft (III)star[31].*

The covalent bond between different monomers restricts macroscopic separation of chemically different polymer blocks. This leads to the formation of microscopic heterogeneities in molecular dimensions. Polymer-polymer phase behavior is controlled by the choice of monomers, molecular architecture, composition and molecular size[31].

The Flory-Huggins segment-segment interaction parameter, χ_{AB}, and the total degree of polymerization, N, are two essential parameters influencing the block copolymer behavior. χ_{AB} gives the free energy cost per monomer of contacts between A and B monomeric units:

$$\chi_{AB} = \frac{Z}{k_B T}\left(\varepsilon_{AB} - \left(\frac{\varepsilon_{AA} + \varepsilon_{BB}}{2}\right)\right) \qquad \text{Eqn.2.1}$$

where k_B is the Boltzmann constant, ε_{AB} is the interaction energy per monomer units between A and B monomers and Z is the number of nearest neighbor monomers to a copolymer

5

configuration cell. When *A-B* contacts lower the system energy than the sum of *A-A* and *B-B* contacts, mixing of unlike monomers is favored and χ has a negative value. In most cases, *A-B* contacts increase the system energy compared to pure components and χ has a positive value showing repulsion between *A* and *B* monomers. In non-polar polymers, like poly (ethylene), poly (styrene) or poly (isoprene), the interaction energy results from van der Waals forces and represented by

$$\varepsilon_{AB} = -\sum_{A,B} \frac{3}{4} \frac{I_A I_B}{I_A + I_B} \frac{\alpha_A \alpha_B}{r_{AB}^6}$$ Eqn.2.2

where r_{AB} is the segment-segment separation, α is the segment polarizability and I is the ionization potential. In a cubic lattice with $I_A = I_B \cong I$, where no volume change upon mixing is assumed and all but Z nearest contacts are neglected, χ_{AB} may be rewritten as

$$\chi_{AB} = \frac{3}{16} \frac{1}{k_B T} \frac{Z}{V^2} (\alpha_A - \alpha_B)^2$$ Eqn.2.3

From Eqn.2.3, it can be concluded that polymer mixtures having only dispersive interactions will phase separate, since $\chi \geq 0$.

In reality, these assumptions made above are seldom realized since volume and entropy of the system when A and B come into contact are not identical to the pure state, a temperature dependent χ expression is used:

$$\chi(T) = C + \frac{D}{T}$$ Eqn.2.4

where temperature independent term C represents the entropy loss and D is the experimentally determined enthalpy. χ_{AB} varies inversely with temperature. For large *N* loss of configurational and translational entropy reduces A-B monomer contacts and leads to local ordering.

The Gibbs free energy of the system is made up of the enthalpic (*H*) and entropic (*S*) factors[32, 33].

$$G = H - TS$$ Eqn.2.5.

The entropic contribution to free energy scale as N^{-1} and enthalpic contribution scale as χ. The phase state is governed by a balance between the two factors. Thus, the product χN is very important for the block copolymer phase state[30, 31]. *f* and χN determine the equilibrium thermodynamic state of a diblock copolymer melt. Volume fraction of a component, which is

denoted by f, is characteristic of the block copolymer. Segment volume V corresponds to the repeat unit volumes (V_A or V_B). Thus, number of segments per polymer molecule is

$$n = \frac{\rho V N}{M}$$
Eqn.2.6

where ρ is polymer density, M is polymer molecular weight, N is the Avogadro's number. Hence, volume fraction of a component A is
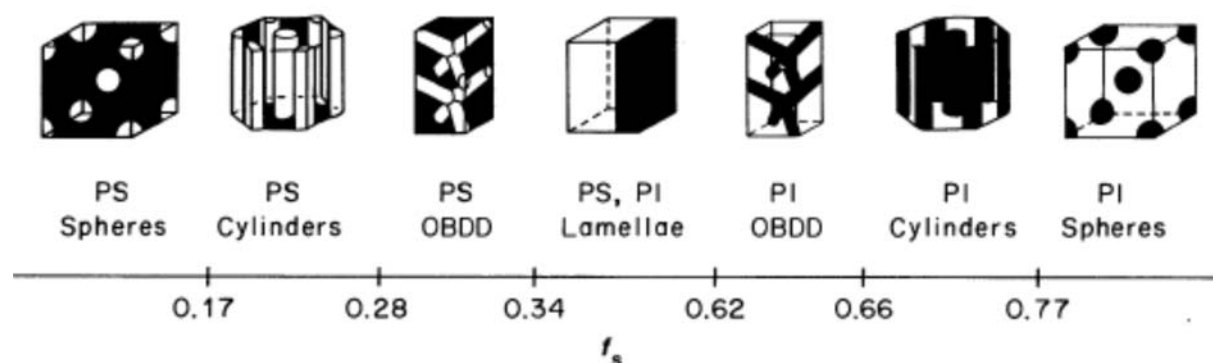
$$f_A = \frac{n_A}{n}$$
Eqn.2.7.

For a symmetric diblock copolymer with f=0.5, when χN<<10, entropic factors dominate and a spatially homogeneous state exist in the bulk polymer[34] (Scheme 2.2, taken from Ref.31). Local composition fluctuations start on a scale proportional to the radius of gyration of the polymer ($R_g^2 = R_{g,A}^2 + R_{g,B}^2$) by an increase in χ or N in the region $\chi N \leq 10$. In case of $\chi N \sim 10$, there is a balance between entropy and enthalpy. A first order transition from disordered to ordered state is observed by a further increase of χN[34, 35]. Here a periodic mesophase is formed from disordered microstructures. This phase transition is called the order to disorder transition (ODT). Further increase in χN results in sharper microdomain boundaries. As χN>>10, energetic factors dominate and ordered microstructures with narrow interfaces and flat composition profiles are formed[31].
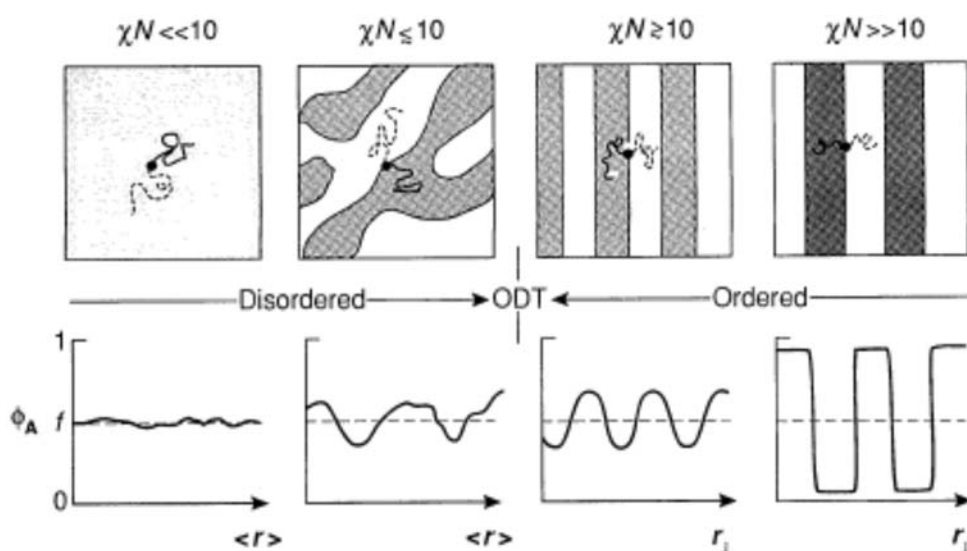
Scheme 2.2. *Structure evolution with the combined parameter χN for a symmetric diblock copolymer with f=0.5. When χN~10, small variations in system entropy (~N^{-1}) or energy (~χ) results in ordered (χN≥10) or disordered (χN≤10) states. A homogeneous composition profile (ϕ_A vs r) is obtained when entropic factors dominate (χN<<10), whereas a strongly microphase separated pattern characterizes the limit when energetic factors prevail (χN>>10)[31].*

Changes in the block copolymer composition, *f*, influences the shape and packing symmetry of ordered microstructures, except near ODT where it is uncorrelated with χN[31]. Since the system is changed by altering the composition of the block copolymer, unequal packing and chain stretching constraints on individual blocks result in new ordered structures over a composition range. The system of poly (styrene)-poly (isoprene) (PS-PI) has seven different ordered phases by variation in the composition of the block copolymer, as seen in Scheme 2-3, taken from Ref.31.

| PS | PS | PS | PS, PI | PI | PI | PI |
| Spheres | Cylinders | OBDD | Lamellae | OBDD | Cylinders | Spheres |

0.17   0.28   0.34   0.62   0.66   0.77

f_s

Scheme 2.3. *Effect of composition change on the ordered phase symmetry in poly (styrene-poly (isoprene) (PS-PI) diblock copolymer[31].*

8

The effects of changing f and χN are combined in the PS-PI diblock phase diagram shown in Figure 2.1.
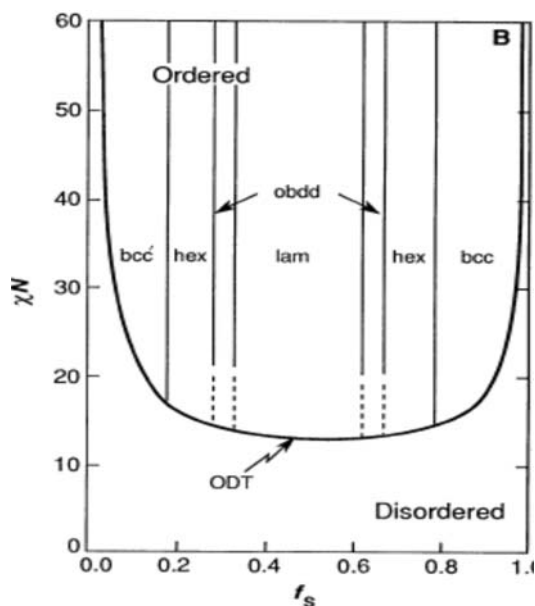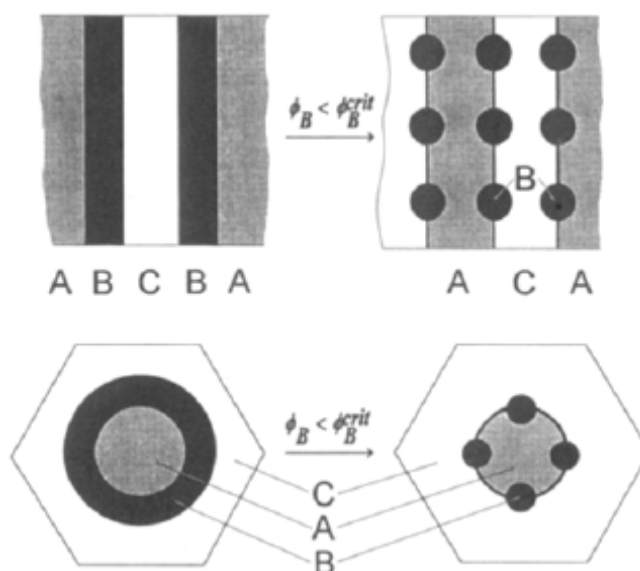

Figure 2.1. *Phase diagram of PS-PI diblock copolymers[31]. Ordered phases correspond to those illustrated in Scheme 2-3.*

In binary block copolymers the composition determines the equilibrium microphase morphology. In ternary block copolymers two independent composition variables have to be considered. The mesoscopic assembly of ABC triblock copolymers are not only governed by composition but also strongly influenced by the by the balance of three binary interaction parameters (χN_{AB}, χN_{BC}, χN_{AC}) or interfacial energies between different polymer pairs as represented by the surface tensions γ_{AB}, γ_{BC}, and γ_{AC}, respectively[36]. Poly (styrene)-block-poly (butadiene)-block-poly (methyl methacrylate) (SBM) is an example of ABC triblock copolymers where the morphologies are determined by the balance of the surface tensions. In this system PS and PMMA are strongly incompatible with PB but weakly incompatible with each other. As a consequence of this thermodynamic imbalance, new types of ordered morphologies result. A lamellar morphology is observed for a symmetric block copolymer with equal amounts of the tree components ($f_A \sim f_B \sim f_C$). If the fraction of the center block (f_B) is reduced below a critical volume fraction, the minimization of the free energy results in curved PS/PB (A/B) and PB/PMMA (B/C) interfaces and an additional PS/PMMA (A/C) interface although A and C are not directly linked. The driving force for the morphological

9

transition is the substitution of the enthalpically unfavored AB and BC contacts by AC contacts. For a polymer with $f_A \sim f_C \sim 0.4$, and $f_B \sim 0.2$, the major components A and C form a lamellar structure with B cylinders located at the lamellar A/C interface as illustrated in Scheme 2.4, taken from Ref.36. The transition depends on the ratio of the surface tensions $\gamma_{AC}/(\gamma_{AB}+\gamma_{BC})$.

Scheme 2.4. *Schematic representation of the morphology transition in ABC block copolymers with composition $f_A \sim f_C \sim 0.4$, and $f_B \sim 0.2$[36].*

The triblock phase diagram was also calculated[37] as shown in Figure 2.2, taken from Ref.37, for two ABA triblocks with τ=0.25 and τ=0.5, where τ is the symmetry parameter ($\tau = \dfrac{f_A}{f_A + f_B}$ and the cases of τ=0 or 1 reduce to a pure diblock case).
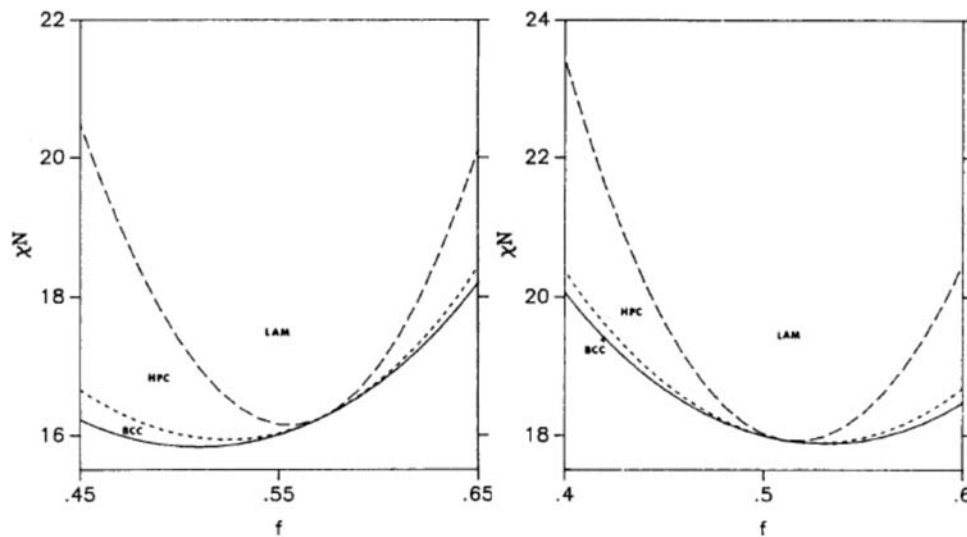
Figure 2.2. *Phase diagram of ABA triblock copolymer melts with τ=0.25 (left) and τ=0.5 (right). Solid lines give the order to disorder transition as a function of (χN) and (f)[37].*

The triblock phase diagrams in the Figure 2.2 are very asymmetric due to the deformation of the central *B* blocks to accommodate outer *A* blocks into *A* domains. At f=0.5, a diblock copolymer goes from disordered phase directly to the lamellar, whereas, for a diblock copolymer with τ=0.25 at the same composition, there are large zones of bcc and hex phases. These regions become narrower for more symmetric triblock copolymers.

The hydrophilic (*A*) and hydrophobic (*B*) blocks, which do not like each other, in an amphiphilic block copolymer result in a positive χ value. The decrease in *A-B* segment contacts reduces the system enthalpy *H*, thus *A* and *B* microdomains tend to form. At the same time, this is opposed by an entropy loss due to localizing *A-B* contacts at the interface and stretching of the polymers to maintain a uniform polymer density in the domains.

2.2   Block copolymer synthesis

Nature uses the combination of hydrophobic and hydrophilic chain end to form interfaces and micelles. However very few well-defined, synthetic, amphiphilic copolymers are commercially available. Living polymerization techniques and their development allow synthesis of novel block copolymers in terms of shape and properties. One can obtain different sized microstructures having desired properties for application in diverse areas, such

as information storage, drug delivery, photonic crystals as well as thermoplastic elastomers, high-impact plastics, pressure sensitive adhesives, additives, etc[30].

Anionic living polymerization has been the most powerful synthetic tool for preparation of well defined polymers in terms of narrow molecular weight distribution with controlled molecular weight, composition, microstructure and architecture for more than half a century. The elimination of chain transfer and termination reactions from chain growth polymerization formed the basis of Szwarc's discovery in 1950s. These chain breaking processes were avoided with the development of special high vacuum techniques to minimize traces (<1 ppm) of moisture and air in the anionic polymerization of non-polar vinyl monomers[38-40]. Anionic polymerization proceeds by organometallic sites, carbanions (or oxanions) with metallic counterions. Carbanions are nucleophiles. Thus, monomers having an electro attractive substituent on the polymerizable double bond can be polymerized by this method.

Initiation of polymerization is accomplished by organometallic compounds fulfilling the requirement of rapid reaction with the monomer at the initiating step with a reaction rate larger than that of propagation step. All active sites start polymerizing the monomer almost at the same time. This results in polymers with narrow molecular weight distributions. The nucleophilic attack of a carbanionic site onto a monomer reforms the first anionic active center and propagation continues with repetition of the same steps. The situation is similar in the case of the ring opening polymerization of cyclic monomers containing heteroatoms such as oxiranes, lactones, thiiranes, and siloxanes. Under appropriate experimental conditions, due to the absence of termination and chain transfer reactions, anionic sites remain active after complete consumption of monomer. This gives the possibility of block copolymer formation, in the simplest case, by introduction of a second monomer into the polymerization mixture.

Besides anionic polymerization controlled living radical polymerization employs concepts of living radical polymerization where chain breaking reactions are minimized and simultaneous growth of all chains can be achieved by instantaneous initiation. Fast initiation and absence of termination resemble the case in anionic polymerization. Intermittent formation of active propagating species is in dynamic equilibrium with dormant species[41, 42]. Radicals may be reversibly trapped in deactivation/activation process according to Scheme 2.2.1, taken from Ref.46. This approach relies on persistent radical effect (PRE)[42-45], which is a peculiar kinetic feature providing a self-regulating effect in controlled radical polymerization systems.
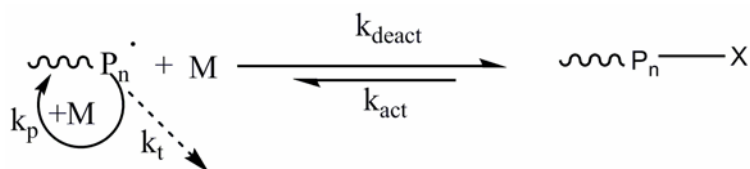
Scheme 2.2.1. Persistent radical effect [46].

Propagating radicals *Pn** are trapped in deactivation by species *X. X* is a stable radical such as a nitroxide[47, 48] or an organometallic species such as a cobalt porphyrin[49]. The dormant species are activated (k_{act}) either thermally, in the presence of light or with an appropriate catalyst as in ATRP to reform the growing centers. Radicals can propagate (k_P) but also terminate (k_t). However, persistent radicals (*X*) cannot terminate with each other but only reversible cross-couple with the growing species (k_{deact}). Every radical-radical termination is accompanied by irreversible accumulation of *X*. Its concentration progressively increases with time, following a peculiar 1/3 power law. As a result, concentration of radicals as well as the probability of termination decreases with time. Growing radicals react with *X* rather than with themselves, since *X* is present in >1000 times higher concentration. ATRP operates via PRE where a steady state of growing radicals is established through activation-deactivation process rather than initiation-termination as in conventional radical polymerization. A general mechanism for ATRP is shown in Scheme 2.2.2, taken from Ref.46. Active species are generated through a reversible redox process catalyzed by a transition metal complex (M_t^n—Y/Ligand, where Y may be another ligand or counterion) which undergoes one electron oxidation with abstraction of a halogen atom *X* from a dormant species, *R—X*, with rate constants of activation, k_{act}, and deactivation, $k_{deact.}$ Polymer chains grow by addition of intermediate radicals to monomers with a rate constant of k_p. Termination reactions (k_t) occur through radical coupling and disproportionation which are less than a few percent of polymer chains. Increased chain length and viscosity of the medium lead to a significant decrease in termination rate coefficients, thus termination decreases. Termination decreases even more because of the PRE[46, 50].
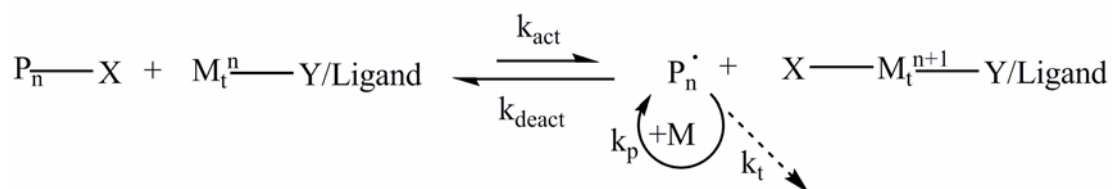
Scheme 2.2.2. Schematic representation of consecutive steps in ATRP and propagation accompanied by reversible activation/deactivation and termination [46].

3   Experimental

3.1   Materials

Tetrahydrofuran (THF) was distilled from THF, butyllithium (BuLi) and 1,1-diphenylethylene (DPE) mixture; anhydrous triethylamine (TEA) was distilled just before the macroinitiator preparation. Copper(I) bromide (CuBr, Aldrich, 98%, Steinheim, Germany) was purified by boiling in a mixture of 1:1 v/v Millipore water/glacial acetic acid for a short time and subsequent filtration. The precipitate was rinsed with Millipore water, ethanol and diethyl ether respectively, and dried under reduced pressure for 24 h[21]. N,N,N',N',N''-pentamethyldiethylenetriamine (PMDETA) (Aldrich, 99%) was purified by distillation under reduced pressure. Ethyl 2-bromoisobutyrate (Aldrich, 98%), titanium(IV) tetraisopropoxide (TTIP) (Aldrich, 99.9%), hydrochloric acid 37% (HCl, Acros, Geel, Belgium), isopropanol (Acros) and THF (for film preparation, extra dry from Acros) were used without further purification. Poly (ethyleneglycol) methyl ether methacrylate [(PEO)MA] (Aldrich) with molecular weight of ~476 g/mol was passed through Al_2O_3 column before polymerization. Hydroxyl terminated PDMS was obtained from ABCR Gelest (Karlsruhe, Germany) and used without further purification; number average molecular weight of this compound was 4200g/mol with a polydispersity of 1.87. Monomethacryloxypropyl terminated poly (dimethyl siloxane), (PDMS)MA, monomer was purchased from ABCR Gelest with a molecular weight of 1000 g/mol and used as received. Poly (ethylene oxide) macroinititator was prepared at Max Planck Institute for Polymer Research by anionic polymerization of ethylene oxide and stopping with ethyl 2-bromoisobutyrate. Absolute ethanol (>99.8%, Aldrich), acetone (>99.5, Acros), chlorobenzene (>99.5%, Fluka), ter-butyl alcohol (99.5%, Riedel-de Haën), poly (3,4-ethylenedioxythiophene) poly (styrenesulfonate) (PEDOT:PSS, Baytron P) (Bayer), Alconox powder (Aldrich) were used as received. FTO on normal soda-lime glass substrate with a thickness of ~600 nm was obtained from Hartford Glass Co., USA. Crystalline titania particles, Ti-Nanoxide-T, were purchased from Solaronix, Switzerland with particle size 13nm.

3.2   Characterization

The macroinititators, monomers, synthesized polymers and titania/polymer nanocomposite films were characterized with the methods and corresponding instrumental details below.

3.2.1 Nuclear Magnetic Resonance Spectroscopy

The structure of the compounds can be determined by interpretation of nuclear magnetic resonance spectra peaks. NMR is a very selective technique distinguishing among many atoms in a molecule which differ only in terms of their local chemical environment.^{1}H NMR spectra of the monomers, macroinitiator and the block copolymers were recorded on a Bruker DRX-300 NMR instrument using $CDCl_3$ as the solvent.

3.2.2 Gel Permeation Chromatography (GPC)

Gel permeation chromatography (GPC) is a separation technique based on hydrodynamic volume (size in solution)[51]. It is often used for molecular weight and polydispersity index determination of polymers. Molecules are separated from one another based on the differences in their molecular size. Two phases exist inside the GPC column; a stationary phase of an inert gel porous beads and a mobile phase which is the eluent run through the column. A dilute polymer solution is injected into the solvent stream, and then it flows through the columns composed of inert porous material of controlled pore size. The larger molecules are excluded from most of the pores. Consequently they follow a shorter path, and elute first. They are detected by suitable detectors to form an elution curve, usually concentration versus elution time. The molecular weight of each eluted fraction can be determined by calibration of the instrument with standards of the same chemical composition. Molecular weight distributions of the macroinitiator and the triblock copolymer were determined by GPC in a setup comprising a Waters 515 pump equipped with one linear polymer standard service column (SDV) with dimensions 0.8×30 cm or three polymer standard service columns (SDV) in series with the same dimensions and porosity 5×10^2, 10^5, 10^6 Å respectively, filled with poly (styrene/divinylbenzene) calibrated with very low polydispersity poly (dimethylsiloxane) standards and a differential refractive index detector (ERC RI-101) using toluene as eluent with a flow rate of 1,0 ml/min at an operating temperature of 30°C.

3.2.3 Thermal Analysis

3.2.3.1 Differential Scanning Calorimetry

Differential scanning calorimetry is used to study the thermal transitions of a polymer. The thermal transitions can be first order, where both a latent heat and a change in the heat capacity of the material observed, like melting and crystallization. Second order transitions involve a change in heat capacity without a latent heat, like the glass transition[52]. Differential scanning calorimetry (DSC) measurements were done with a Mettler Toledo DSC 822 instrument under nitrogen.

3.2.3.2 Thermal Gravimetric Analysis (TGA)

Thermal gravimetric analysis is an analytical technique that measures the weight loss (or weight gain) of a material as a function of temperature. The measurement atmosphere can be oxygen or nitrogen to observe drying, structural water release, structural decomposition, carbonate decomposition, gas evolution, sulfur oxidation, fluoride oxidation and re-hydration[53]. Thermogravimetric analysis was carried out with a Mettler Toledo TGA 851 device under nitrogen.

3.2.4 Particles size distribution in solution

Dynamic light scattering (DLS) is used to determine the size distribution profile of titania particles in prepared sol-gel[54]. A Neon-Helium laser (25 mW) at the wavelength of 633nm with ALV correlator was used.

3.2.5 Rheology measurements

Rheology sensitively investigates the order to disorder transition, different ordered phases and phase transformation kinetics between ordered and disordered phases of block copolymers due to the measurable large viscoelastic contrast from different phases[55, 56]. An advanced rheometric expansion system (ARES) (Rheometric Scientific) was used in parallel plate geometry with a diameter of 6 mm disks. The gap between them was 0.87 mm. Frequency of 10 rad/s at variable strain by 2°K/min heating rate temperature measurements were performed. For frequency measurements at 30°C and 140°C, strain was 3% and 10 %, respectively.

3.2.6 High Performance Liquid Chromatography (HPLC)

High performance liquid chromatography is used for separation of low to moderate molecular weight compounds. In our case, this technique was used to determine the components of the block copolymers. The HPLC column was Reversed Phase C8 (Merck, Darmstadt). An Agilent 1100 pump was connected in the feed to the PL-ELS light scattering detector. A gradient of THF/H_2O was run with a flow rate of 1ml/min.

3.2.7 Photoluminescence (PL)

Photoluminescence (PL) spectroscopy depends on electronic excitations and gives information about the electro-optic and photoelectric properties of materials[27]. PL is used to detect the surface defects occurring on titania nanoparticles. Photoluminescence spectra were recorded on a Spex FLUOROLOG II (212) using a Xenon discharge lamp at 400 W. Emission spectra were collected at an excitation wavelength of 350 nm.

### 3.2.8 Scanning Electron Microscopy (SEM)

Scanning electron microscopy (SEM) images samples by collecting the secondary electrons emitted from the sample after scanning a focused electron beam onto the sample. SEM images were obtained on field emission SEM (LEO 1530 "Gemini") which allows obtaining images with high magnification at low operating voltages. Thus, resolution of 6-8 nm can be achieved. The accelerating voltage was 3 kV. The contrast of the images was adjusted using the Image J 1.39a software[57].

3.2.9 Transmission Electron Microscopy (TEM)

Transmission electron microscopy (TEM) is a kind of microscopy technique where a beam of electrons transmitted through an ultra thin specimen. Electrons interact with the specimen passing through it, and an image is formed from the transmitted electrons. Sample preparation techniques to obtain en electron transparent region include ion milling and wedge polishing by focused ion beam. For TEM measurement, a lamella from 2%TTIP plasma treated/annealed at 450°C sample was cut by FIB, put on a TEM grid by FIB-induced Pt deposition. Then this lamella was imaged by TEM (FEI Tecnai F20).

3.2.10 Scanning Force Microscopy (SFM)

Scanning force microscope (SFM), also called atomic force microscope (AFM), operates by measuring attractive or repulsive forces between a tip and the sample[58]. In its repulsive contact mode, the instrument lightly touches the sample with a tip at the end of a cantilever. As a raster-scan drags the tip over the sample, a beam deflection set-up measures the vertical deflection of the cantilever, which is proportional to the local sample height. Thus, in contact mode the SFM measures repulsion forces between the tip and sample. In non-contact (tapping) mode, the SFM derives topographic images from measurements of attractive forces; the tip is in intermittent contact with the surface[59], as depicted in Scheme 3.2.6-a and c, taken from Ref.60. In tapping mode, the probe is driven into an oscillation at its resonance frequency, by a small piezoelectric element. The tip is located at the end of the cantilever and the bending of the cantilever (contact mode) or damping of its oscillation amplitude (tapping mode) in response to the repulsive and attractive forces between the tip and the sample is monitored by an optical lever. A laser beam, focused on the cantilever is reflected onto a four-quadrant photo detector, with pairs of sectors (A, B) and (C, D) arranged to detect bending deflection, bending oscillation, and torsion of the cantilever (Scheme 3.2.6-b). In contact mode, the feedback raises or lowers the tip and keeps the cantilever deflection at the set-point value. In tapping mode (Scheme 3.2.6-c), the oscillation amplitude, which is reduced from the amplitude of the freely oscillating probe by tip-to-sample repulsive interactions that occur each cycle, is kept at the set-point value by adjusting the vertical position of the tip with the piezoelectric drive. The variations of the z-position of the tip during scanning are plotted as a function of the x,y position of the tip to create the height image, where gray or color contrast is used to show the z-variations[60].
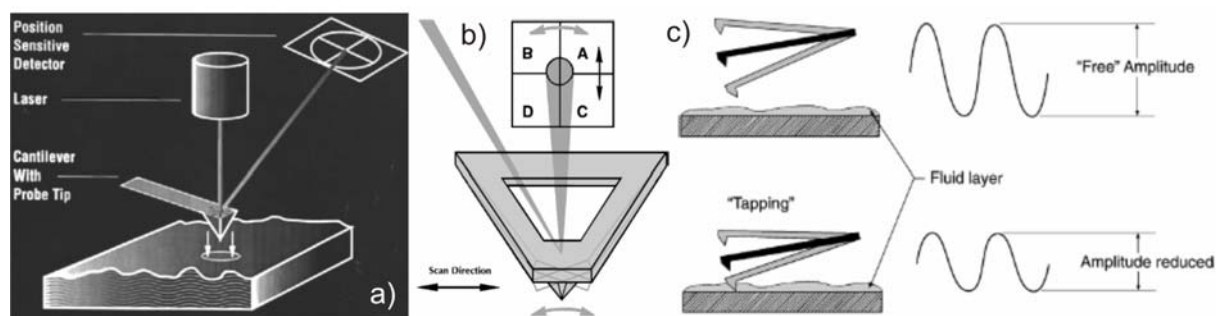
Scheme 3.2.6. *a) Schematic representation of an operating AFM, b) Scanning and detection of the normal and lateral force variations in the contact mode using differential signals (A + B) − (C + D) and (A + C) and (B + D), respectively. To increase the lateral force sensitivity, scanning is performed sidewise as shown. (c) Tapping mode cantilever oscillation amplitude in free air and during scanning[60].*

In analysis of polymer surfaces, to reduce any possible damage to the sample, non-contact mode is usually used. In tapping mode, short, intermittent contacts between the tip and surface minimize the inelastic deformation of the sample. The phase images that are recorded simultaneously with the height images show variations of the phase of an oscillating probe determined at the fundamental resonant frequency of the freely oscillating probe. Phase images provide the contrast of morphological and nonstructural features due to their high sensitivity to surface imperfections such as steps, cracks, etc. The phase changes are more informative on surfaces with local variations of the mechanical properties. SFM analysis gives information on both surface topography and materials property.

SFM images were recorded using a Veeco Dimension 3100 System (Veeco, Santa Barabara, USA) in tapping mode equipped with Si cantilevers (Olympus OMCL-AC240TS, Japan) having spring constant ranging between 33.2 and 65.7 N/m and resonance frequency 370.4-319.7 kHz. The images were analyzed using the software Nanoscope 5.30r3sr3[61].

3.2.11 Scanning Kelvin Probe Microscopy (SKPM)

Scanning Kelvin Probe Microscopy (SKPM) is a derivative of scanning force microscopy (SFM). SKPM measures the contact potential difference (CPD) between the tip and the sample surface. An alternating current (ac) voltage with adjustable direct current (dc) offset is applied between a conducting SFM tip and the sample electrode and the resulting electrostatic

force is detected by a lock-in amplifier. A feedback circuit controls the dc tip potential until the CPD is compensated[62]. A schematic representation of a working SKPM is shown in Scheme 3.2.7.1, taken from Ref.62.
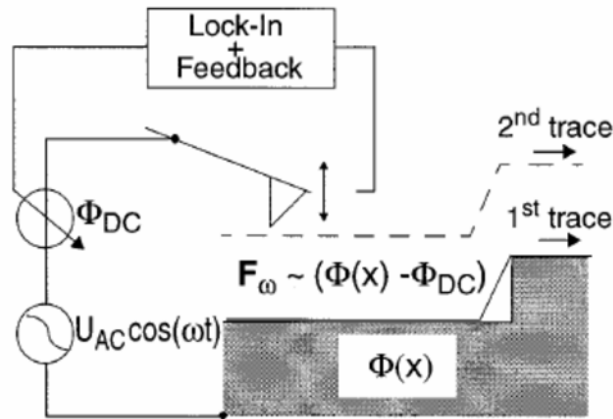

Scheme 3.2.7.1. SKPM measures the surface potential distribution as depicted above. In the first trace (solid line), the topography of a single line is acquired using tapping mode, i.e. mechanical excitation of the cantilever. In the second trace (dashed line), this topography is retraced at a set lift height from the sample surface to detect the electric surface potential Φ(x). In the second trace, the cantilever is excited electrically by applying the periodic voltage $U_{ac} \cos (\omega t)$ to the tip. The feedback then changes the dc tip potential Φ_{dc} until the ω component of the tip force vanishes [$\Phi_{dc} = \Phi(x)$][62].

SKPM studies were carried out with the Veeco Dimension 3100 System. Uncoated Si Cantilevers (Olympus OMCL-AC240TS, Japan) at a nominal resonance frequency of 70 kHz were used. In order to reduce the contact resistance to the cantilever holder of the SFM a small amount of conductive silver was put on the chip. Prior to the measurement the cantilevers were cleaned with argon plasma (Harrick Plasma Cleaner/Sterilizer; Ossining, New York; Model PDC-002, 40sec at High Power). The surface work function is measured in an interleaved step between two scan cycles, where the tip follows the topography at a defined lift height. By keeping this height as low as possible (typically -10 to -20 nm) the best lateral resolution can be achieved (a small influence on the scan height on the measured signals is observed). During the interleaved step, the contact potential difference (i.e. the difference in work function ΔΦ) of SFM-tip and sample surface was measured[62]. In order to determine the absolute value of the work function of the investigated sample surfaces, Φ_{Sample}, reference measurements on freshly cleaved HOPG substrates having a known work function of

Φ_{HOPG}=4,65eV were performed for each sample. With the sample signal $\Delta\Phi_{Sample}$ and the reference $\Delta\Phi_{HOPG}$ the absolute value is given by

$$\Phi_{Sample} = \Phi_{HOPG} + \Delta\Phi_{HOPG} - \Delta\Phi_{Sample} \qquad \text{Eqn.3.2.7.1}$$

Schematic representation of the relevant energy levels is shown in Scheme 3.2.7.2.
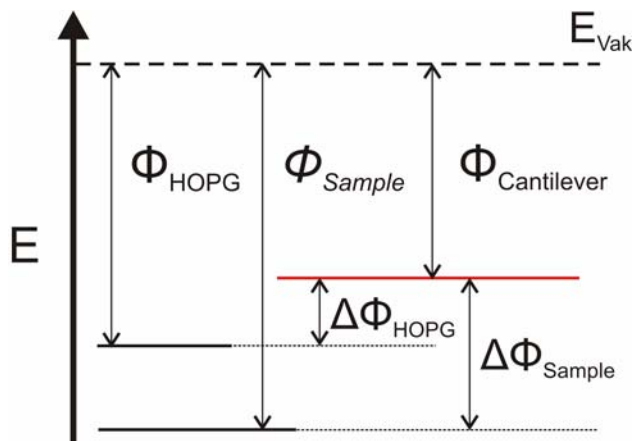

Scheme 3.2.7.2. *Schematic representation of the relevant energy levels for SKPM. During the measurement, the contact potential difference, $\Delta\Phi_{Sample}$, of SFM-tip and sample surface is measured. By comparing this value with a reference sample (Φ_{HOPG}) the unknown Φ_{Sample} can be determined.*

3.2.12 Conductive prove scanning force microscopy (CPM)

Conductive probe scanning force microscopy (CPM) is used for studying the electrical transport in integrated blocking layer. CPM measurement was performed with Veeco Multimode SFM System (Veeco, Santa Barabara, USA) equipped with Nanoscope IIIa controller with quadrix extension and TUNA module (Tunneling AFM). Pt/Ir coated on tip and detector side Si cantilevers (Nanosensors PPP-EFM-50) at a nominal resonance frequency of 45-115 kHz were used. The tip was n-type semiconducting single crystal silicon (4-6 ohm.cm).The samples form CPM were prepared on Pt (50 nm) coated Si wafer with according to recipe above with 2% titania precursor concentration.

3.2.13 Focused Ion Beam (FIB)

Focused ion beam (FIB)-SEM instruments enables serial sectioning tomography experiments to study micron scale to smaller features in the materials structure[63]. These microscopes use a focused highly energetic beam of gallium ions (Ga^+), typically 30 kV, that can be operated at low beam currents for imaging or high beam currents site specific sputtering or milling. Moreover, the primary beam can be focused on very small spot sizes, on the order of 5-20 nm. When the Ga^+ primary ion beam hits the sample surface, it sputters a small amount of material, which leaves the surface as secondary ions or neutral atoms. The primary beam also produces secondary electrons. As it rasters on the sample surface, the signal from the sputtered ions or secondary electrons are collected to form an image[64]. At low primary beam currents, very little amount of the material is sputtered. At high primary currents, in conjunction with the small spot size a controlled removal of the material of the nanosclae by ion sputtering is possible. A schematic drawing of the FIB set-up and typical sample geometry are shown in Scheme 3.2.8.1, taken from Ref.63. A typical FIB tomography experiment using cross-sectioning milling starts with location of an area of interest on the sample surface and creation of a trench around this area with high beam currents, 5-20 nA. Protective platinum is usually deposited by FIB-induced decomposition of precursor gases on top of the surface interest before trenching to prevent unwanted milling or Ga^+ implantation in this surface. Then the serial sectioning with ion beam currents between 30 and 100 pA is done. After the sectioning is complete, SEM images of the cut are taken.
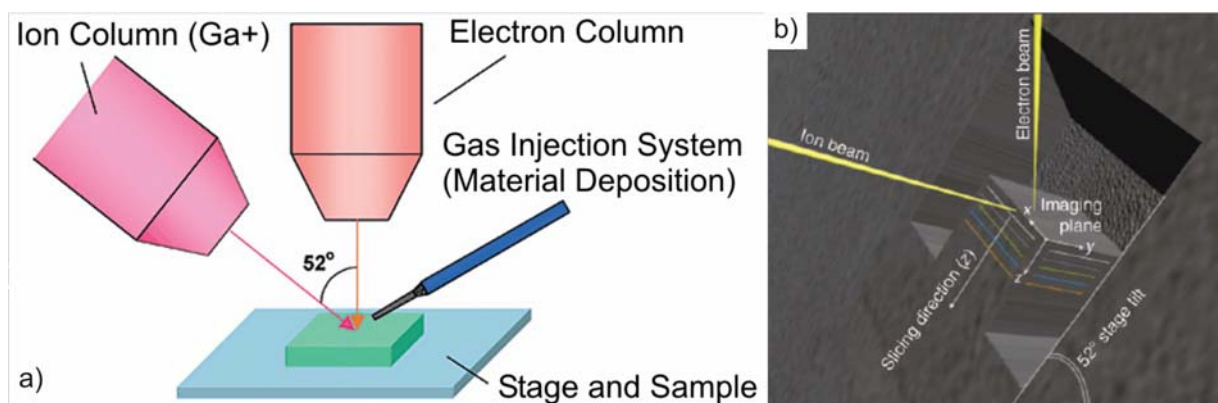
Scheme 3.2.8.1. *a) Schematic drawing of a FIB-SEM set-up, b) Typical sample geometry and beam orientation for a FIB–SEM tomography experiment using cross-section milling[63].*

The milling process was done by FEI Nova 600 Nanolab dual beam instrument which combines an SEM for sample observation with a Ga^+ ion beam that can be focused down to approx. 5 nm beam diameter. Gas injection system allowed the targeted deposition of Pt by decomposition of precursor gas with the ion beam.

3.2.14 X-ray Reflectivity

X-ray reflectivity is a nondestructive method which probes the variations in the electron density[65]. It is widely used in characterization of thin films. When x-rays interact with matter both on surface and inside the film, inelastic scattering as Compton scattering or photoionization, or elastic scattering by electrons, called Thomson scattering, may occur. The wavelength of x-rays is conserved for Thomson scattering, and this is used for structural investigations of the matter[66]. Therefore, x-ray reflectivity reveals information about the matter inside the film that can not be obtained via microscopy techniques. In an x-ray reflectivity experiment, a highly collimated x-ray beam illuminates the sample with a very small incidence angle, resulting in reflected x-rays. The incidence angle is varied and the intensity of the reflected x-rays is monitored as a function of the incidence angle. The plot of reflectivity versus scattering angle shows a sharp edge at the critical angle of total external reflection, a characteristic overall power law decay and a modulation pattern due to presence of surface layers. The shape and decay of these modulations give information on the thickness, number and interfacial properties of the surface layers[65].

When an x-ray beam hits a surface, as depicted in Scheme 3.2.9.1, taken from Ref.65, it undergoes reflection where
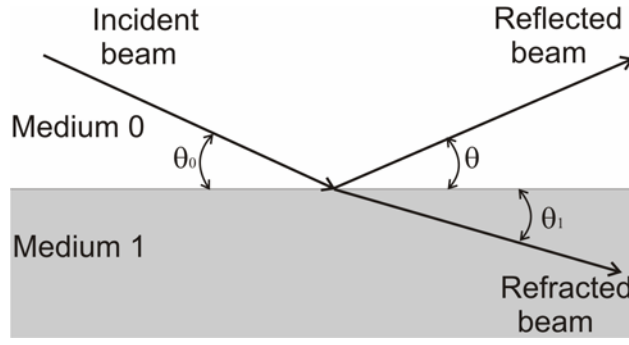
$$\cos\theta_0 = \cos\theta \qquad\qquad \text{Eqn.3.2.9.1}$$

and refraction. The ratio of the refractive indices of the two media determines the refraction angle, θ_1, in comparison to the grazing angle of incidence, θ_0, according to the Snell's law:

$$n_0\cos\theta_0 = n_1\cos\theta_1 \qquad\qquad \text{Eqn.3.2.9.2}$$

where n_0, n_1 are the refractive indices of the medium 0 and medium 1, respectively. When medium 0 is air, then $n_0=1$, and

$$\cos\theta_1 = \left(\frac{1}{n_1}\right)\cos\theta_0 \qquad\qquad \text{Eqn.3.2.9.3.}$$

Scheme 3.2.9.1. *Schematic representation of the relationship between a beam incident on a surface at angle θ_0, the reflected portion at θ_0 and the refracted beam in medium 1 at θ_1 with respect to surface*[65].

If $n_1 > 1$, then $\theta_1 > \theta_0$ and there is a real angle of reflection, θ_1, for all incidence angles, θ_0. If $n_1 < 1$, then $\theta_1 < \theta_0$ and there is a real angle of reflection for all incidence angles greater than the critical angle θ_c. θ_1 is zero at

$$\cos\theta_c = \cos\theta_0 = n_1 \qquad\qquad \text{Eqn.3.2.9.4.}$$

and total external reflection occurs for $\theta_0 < \theta_c$.

Combining Snell's law and critical angle expression,

$$n_1^2 \sin^2(\theta_1) = n_0^2 \sin^2(\theta_0) - n_0^2 \sin^2(\theta_c) \text{ or } k_{z1} = \sqrt{\left(k_{z0}^2 - k_{zc}^2\right)} \qquad \text{Eqn.3.2.9.5}$$

where k_{zi} is the *z*-component of the wave vector of wave *i*.

The amplitude of the reflected x-ray beam, *r*, and its intensity, *R*, are given by

$$r = \frac{k_{z0} - k_{z1}}{k_{z0} + k_{z1}} \text{ and } R = \left|\frac{k_{z0} - k_{z1}}{k_{z0} + k_{z1}}\right|^2 \qquad\qquad \text{Eqn.3.2.9.6,}$$

respectively. *R* and *r* are both normalized quantities with respect to the amplitude and intensity of the incident wave, and the expression of *R* is called *Fresnel's law*.

In case of reflectivity from a single layer on a substrate, many reflections and refractions occur inside the layer. The Fresnel reflection coefficient, r_{01} represents the fraction of the amplitude reflected upon traversal from media *0* to media *1*. The Fresnel transmission coefficient, t_{01}, shows the amplitude transmitted from medium *0* to medium *1*. Their general values are given by

$$r_{01} = \frac{k_{z0} - k_{z1}}{k_{z0} + k_{z1}} \quad \text{and} \quad t_{01} = \frac{2k_{z1}}{k_{z0} + k_{z1}} \qquad \text{Eqn.3.2.9.7.}$$

The transmission of the beam from medium *0* to medium *1* (t_{01}), the reflection at the interface *1-2* (r_{12}) and the transmission from medium *1* to medium *0* (t_{10}) form the path of the beam. As represented in the Scheme 3.2.9.1, taken from Ref.65, besides the amplitude change, there exists a phase shift with respect to the incident wave. This phase shift is *2Φ* where

$$\Phi_i = \frac{2\pi}{\lambda} n_1 \sin(\theta_1) d = k_{z1} d \qquad \text{Eqn.3.2.9.8.}$$

The sum of the total amplitude and intensity yields

$$r = \frac{r_{01} + r_{12} e^{-i2\Phi_i}}{1 + r_{10} r_{12} e^{-i2\Phi_i}} \quad \text{and} \quad R = \left| \frac{r_{01} + r_{12} e^{-i2\Phi_i}}{1 + r_{10} r_{12} e^{-i2\Phi_i}} \right| \qquad \text{Eqn.3.2.9.9}$$
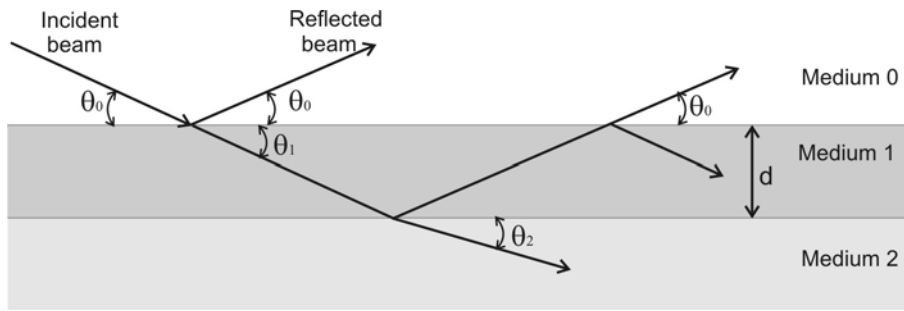
Scheme 3.2.9.2. *Schematic representation of the beam path in a specimen of a sample of thickness, d, on a substrate. When the beam hits the surface, it is reflected at an angle θ_0, and refracted at the vacuum-specimen interface at an angle θ_1, it is then reflected and refracted at the sample-substrate interface*[65].

The reflectivity *R* shows a beating pattern, which is called *Kiessig fringes*. Between the maxima, the shift of the internally reflected waves is *2π* and the waves interfere constructively. The first rough estimate of the film thickness, *d*, from the interval *Δq* between the two maxima can be made by

$$d = \frac{2\pi}{\Delta q} \qquad \text{Eqn.3.2.9.10.}$$

X-ray reflectivity experiment was conducted using a Seifert XRD-TT3003 diffractometer equipped with Göbel mirror.

3.2.15 Small Angle X-ray Scattering (SAXS)

Small angle x-ray scattering (SAXS) probes relatively large-scale structures in contrast to WAXS. SAXS is recorded at angles between 0.1°-5°, where information about the shape and size of macromolecules, characteristic distance of partially ordered materials is contained. The structure of the polymer systems can be revealed from SAXS data[30].

When an x-ray beam hits an object, every electron becomes a source of a scattered wave. Since the energy of an x-ray photon is very large compared with the binding energy of an atom, all electrons will behave as if they were free. Consequently, all secondary waves are of the same intensity, by the well known Thomson formula

$$I_e(\theta) = I_p \times 7.9 \times 10^{-26} \times \frac{1}{a^2} \times \frac{1 + \cos^2 2\theta}{2} \qquad \text{Eqn.3.2.11.1}$$

where I_p is the primary intensity, a is the difference from the sample and the object. The numerical factor is the square of the so called electron radius (e^2/mc^2). The intensity depends only slightly on the scattering angle 2θ by the polarization factor, which is equal to 1 for the small angles.

The scattered waves are coherent, i.e. the amplitudes are added and then the intensity is given by the absolute square of the resulting amplitude. The amplitudes are equal in magnitude and differ only by their phase, φ, which depends on the position of the electron in the space. A single secondary wave can be expressed in the form: $e^{i\varphi}$. The phase is $2\pi/\lambda$ times the difference between the optical path and some arbitrary reference point.

Phase difference is calculated as shown in Scheme 3.2.11.1, taken from Ref.67. Incident and scattered beam directions are s_0 and s, respectively. The path difference of a point P, specified by the vector r, against the origin 0 is, $\left|\overline{PA}\right| - \left|\overline{OB}\right| = -r(s - s_0)$. The phase is therefore

$$\varphi = -\left(\frac{2\pi}{\lambda}\right) r(s - s_0) \qquad \text{Eqn.3.2.11.2}$$
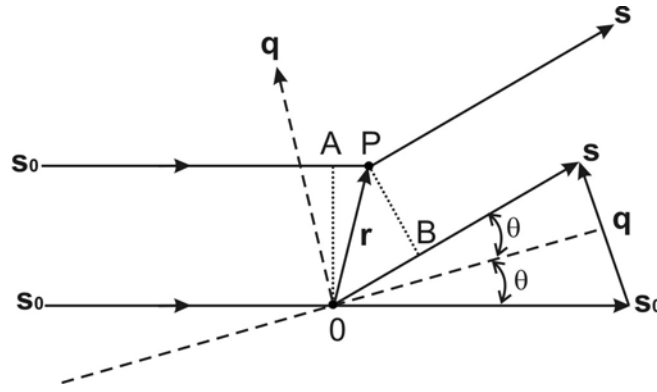
Scheme 3.2.11.1. Scattering by two point centers[67].

This takes the form $\varphi = -qr$. From Scheme 3.2.11.1, $(s\text{-}s_0)$ lies symmetrically with respect to the incident and the scattered beam, and its magnitude is $2\sin\theta$. Consequently, the vector q has the same direction and the magnitude:

$$q = \frac{4\pi}{\lambda}\sin\theta \qquad\qquad \text{Eqn.3.2.11.3}$$

where λ is the wavelength of the incident beam, θ is the half the scattering angle, angle between the incident and scattered beams.

The resulting scattering amplitude can be obtained by summing up all secondary waves represented by a term e^{-iqr} each. Since a single electron cannot be exactly localized, it is convenient to use electron density, $\rho(r)$, which is the number of electrons per unit volume (cm^3). A volume element dV at position r contains $\rho(r)dV$ electrons. By integration over the whole volume irradiated V, the Fourier transform of $\rho(r)$ in q direction within an object is obtained.

$$F(q) = \iiint dV \cdot \rho(r)e^{-iqr} \qquad\qquad \text{Eqn.3.2.11.4}$$

The intensity is derived by using the conjugate complex F^*:

$$I(q) = FF^* = \iiint\iiint dV_1 \cdot dV_2 \cdot \rho(r_1)\rho(r_2)e^{-iq(r_1-r_2)} \qquad\qquad \text{Eqn.3.2.11.5}$$

which is again a Fourier integral, involving the relative distance $(r_1\text{-}r_2)$ for every pair of points. The double integral can be solved in two steps; first to summarize all pairs with equal relative distance, then to integrate over all relative distances, including the phase factor.

28

The first step is the mathematical operation of convolution square or autocorrelation, and is defined by

$$\tilde{\rho}^2(r) \equiv \iiint \rho(r_1)\rho(r_2)dV_1 \text{ with } \textbf{\textit{r}}=(\textbf{\textit{r}}_1\textbf{-}\textbf{\textit{r}}_2)=constant \qquad \text{Eqn.3.2.11.6}$$

Every electron pair with relative distance $\textbf{\textit{r}}$ can be represented by a point in a fictious space. The density of these points is then given by $\tilde{\rho}^2(r)$. As every point is counted twice with $\textbf{\textit{r}}$ and $-\textbf{\textit{r}}$, the distribution in this space must show a center of symmetry, whether this is the case in ordinary space or not.

The second step consists of integration over the fictious space:

$$I(q) = \iiint \tilde{\rho}^2(r) \cdot e^{-iqr} \cdot dV \qquad \text{Eqn.3.2.11.7}$$

This is a Fourier transform again. So the intensity distribution in $\textbf{\textit{q}}$ or in reciprocal space is uniquely determined by the structure of the object, as expressed by $\tilde{\rho}^2(r)$. Conversely, the latter can be obtained from $I(q)$ by the inverse Fourier transform:

$$\tilde{\rho}^2(r) = (2\pi)^{-3} \iiint I(q) \cdot e^{iqr} \cdot dq_x dq_y dq_z \qquad \text{Eqn.3.2.11.8}$$

A general conclusion can be drawn from Eqn.3.2.11.7 and 8: there is reciprocity between ordinary and reciprocal space. As they are connected by the phase $\textbf{\textit{qr}}$ only, the result will be the same, when $\textbf{\textit{r}}$ is enlarged and $\textbf{\textit{q}}$ is diminished by the same factor. Large particles will give a diffraction pattern concentrated at small angles[67].

With a wavelength about 1 Å, particles and inhomogenities in colloidal dimensions can be investigated in a range of one or two degrees which is the typical domain of small angle scattering. In the majority of these cases, the system is statistically isotropic and no long-range order exists, i.e. there is no correlation between particles at great spatial distances. The particles are embedded in a matrix which is considered as a homogeneous medium with an electron density of ρ_0. The electron density in equations 3.2.11.4-8 can be replaced by $\Delta\rho=\rho-\rho_0$, which can take positive or negative values. Also, the phase factor can be replaced by its average over all orientations. This leads to the fundamental formula of Debye[68]

$$\langle e^{-iqr} \rangle = \frac{\sin(qr)}{qr} \qquad \text{Eqn.3.2.11.9}$$

Thus, Eqn.3.2.11.7 reduces to the form

$$I(q) = 4\pi \int_0^\infty \gamma(r) \frac{\sin(qr)}{qr} r^2 dr \qquad \text{Eqn.3.2.11.10}$$

which is the most general formula for scattering pattern of any system obeying the above restrictions. $\gamma(r)$ is the so-called correlation function[69] or characteristic function[70]. It can be obtained with the inverse Fourier transform

$$\gamma(r) = \frac{1}{2\pi^2} \int_0^\infty I(q)q^2 \frac{\sin(qr)}{qr} dq \qquad \text{Eqn.3.2.11.11}$$

For $q=0$ and $r=0$, since the Debye factor has the value 1, Eqn.3.2.11.10-11 take simpler form

$$I(0) = \int_0^\infty 4\pi r^2 \gamma(r) dr \qquad \text{Eqn.3.2.11.12}$$

$$\gamma(0) = \frac{1}{2\pi^2} \int I(q)q^2 dq = V\overline{(\Delta\rho)^2} \qquad \text{Eqn.3.2.11.13}$$

Eqn.3.2.11.12 requires some consideration. For, at $q=0$ exactly, all secondary waves are in phase and $I(0)$ may be expected to be equal to the square of the total number of electrons in the irradiated volume V. However, $I(0)$ can not be measured experimentally. Eqn.3.2.11.12 can be interpreted as each electron of volume V acting in coherence only with an environment defined by $\gamma(r)$, thus $I(0)$ being an extrapolated value.

Eqn.3.2.11.13 shows that the integral of the intensity over the reciprocal space is directly related to the mean square fluctuation of electron density, irrespective of special features of the structure. If parts of the system are shifted or deformed, the diffraction pattern might be altered but the integral in Eqn.3.2.11.13 must remain invariant

$$Q = \int_0^\infty I(q)q^2 dq = 2\pi^2 V\overline{(\Delta\rho)^2} \qquad \text{Eqn.3.2.11.14}$$

At low q region, for $qr \ll 1$ Debye factor is $\frac{\sin(qr)}{qr} \cong 1 - \frac{(qr)^2}{3!} + ...$, Eqn.3.2.11.10 reduces to[67]

$$I(q) = 4\pi \int \gamma(r)\left(1 - \frac{(qr)^2}{6} + ...\right)r^2 dr \cong I(0)\left(1 - \frac{q^2 R_g}{3}\right) \qquad \text{Eqn.3.2.11.15}$$

30

where R_g is the radius of gyration given by

$$R_g^2 = \frac{\frac{1}{2}\int \gamma(r)r^4 dr}{\int \gamma(r)r^2 dr} \qquad \text{Eqn.3.2.11.16}$$

R_g is related to the electron density, $\rho(r)$, of the particle and can be represented as

$$R_g^2 = \frac{\int \rho(k)k^2 dk}{\int \rho(k)dk} \qquad \text{Eqn.3.2.11.17}$$

by defining $\boldsymbol{k}$ as the vector taken from the center of gravity of $\rho(r)$.

The radius of gyration is only related to the geometrical parameters of simple triaxial bodies for homogeneous particles, e.g. $R_g = \sqrt{\frac{3}{5}} \cdot R$ for spheres with radius R; $R_g = \sqrt{\frac{R^2}{2} + \frac{H^2}{12}}$ for cylindrical particles with length H and radius R in cross-section.

Since $e^{-x} \cong 1 - x$ for $\boldsymbol{qr}$<<1, Eqn.3.2.11.15 can also be expressed as

$$I(q) \cong I(0)\exp\left[-\frac{R_g^2 q^2}{3}\right] \qquad \text{Eqn.3.2.11.18}$$

This is the so-called Guinier's law. It allows to obtain R_g^2 and $I(0)$ from scattering data in the smallest angle region without any prior assumption on the shape and internal structure of the investigated particles.

After explaining basic principles regarding SAXS, the interpretation of experimental data is summarized in Scheme 3.2.11.2, taken from Ref.71. In the smallest q regime, the inter-particle interactions are excluded via extrapolation of the concentration in dilute colloidal solutions. Thus, resulted scattering intensity of particles can be used to determine R_g of particles in solvent. In case for polymer chains, information on chain statistics can be obtained by analyzing $R_g{}^2$ as a function of molecular weight by using the relationship which is given by Flory. In intermediate q regime, the spatial resolution is improved and the correlations inside the particles are observed. A decay of q^{-1} corresponds to a cylindrical particle and q^{-2} for a flat particle. In high q regime, in case of a well defined internal surface, structure of the interface can be observed by using the fourth power law of scattering functions for the final slope derived independently by Debye and Porod[67]:

$$I_0 = (\Delta\rho)^2 \cdot \frac{2\pi}{q^4} \cdot S \qquad\qquad \text{Eqn.3.2.11.19}$$

where S is the specific surface of particles and can be determined by the above equation.

Transmission SAXS measurements of the block copolymers were performed with Micromaxx 007 rotating anode using Cu Kα radiation with a Hi-Star Bruker detector where sample to detector distance of 178 cm. SAXS measurements of thin nanocomposite films were performed by GISAXS as explained in the next section.
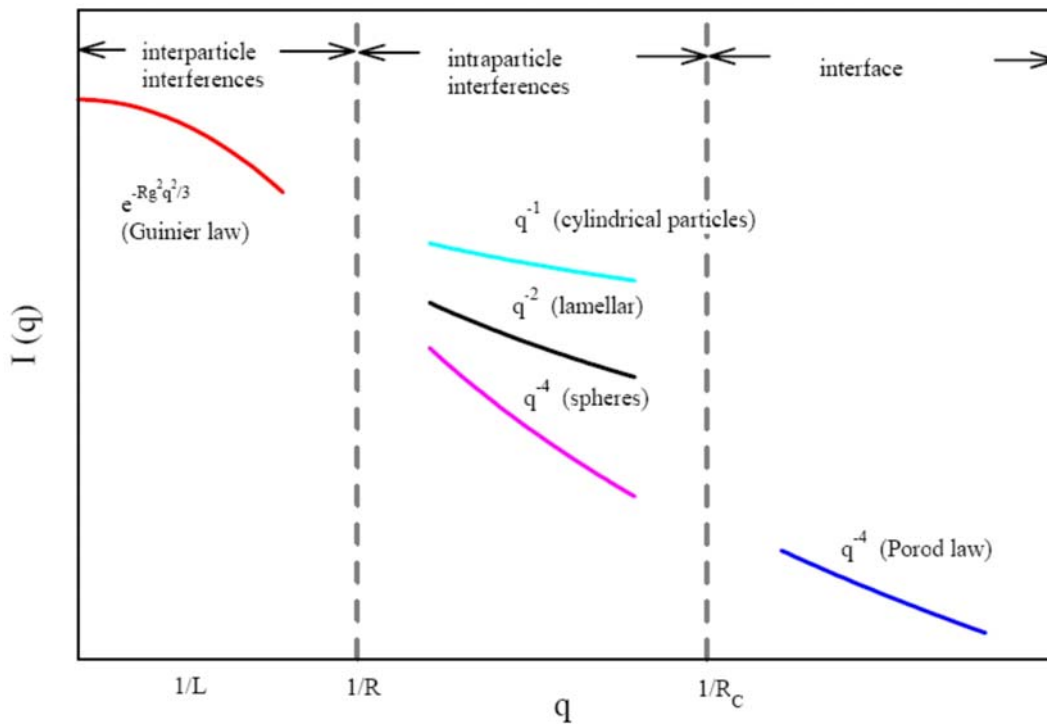

Scheme 3.2.11.2. *Scaling law of scattering intensity at different q regions. L is the length of a rod, R is the radius of a sphere or a platelet and R_c is the diameter of a rod perpendicular to the length direction[71].*

3.2.16 Grazing Incidence Small Angle X-ray Scattering (GISAXS)

Grazing incidence small angle X-ray scattering (GISAXS) is a versatile tool to characterize nanoscale density correlations, shape of nanoscopic objects at a surface, buried interfaces or in thin films. GISAXS combines features from SAXS (mesoscopic length scale, incident beam definition by multiple slits, area detector) and diffuse x-ray reflectivity (scattering geometry and sample goniometer). Transmission geometry is not applicable to tiny scattering

volumes as in thin films. In GISAXS, the transmission geometry is replaced by a reflection one. Thus, GISAXS provides information about both lateral and normal ordering at a surface or inside a thin film. GISAXS has many advantages over transmission scattering techniques. Long x-ray beam path length through the film plane results in intense scattering patterns for nanometer thicknesses. The bulk scattering is reduced due to limited penetration depth of the incoming beam at glancing angles near the critical angle of the substrate. Larger length scales can be analyzed by increasing the sample to detector distance[72]. Since polymeric samples are not good scaterers as metals or semiconductors, GISAXS experiments on nanostructured polymer films are performed with synchrotron radiation which is highly collimated. In order to make x-ray scattering surface sensitive, a grazing incidence angle α is chosen between about half the critical angle α_c and several critical angles of the film material. The actual choice depends on the investigated system. The geometry of a GISAXS experiment is shown in Scheme 3.2.12.1, taken from Ref.73,74. X-rays are scattered along k_f in the direction ($2\theta_f$, α_f) by electron density fluctuations in illuminated volume. The area detector records scattered rays of exit angles β (α_f) and scattering angle ψ ($2\theta_f$) in the surface plane. A beam stop needs to be set up to block spill-over direct beam as well as the reflected beam and the intense diffuse scattering in scattering plane.
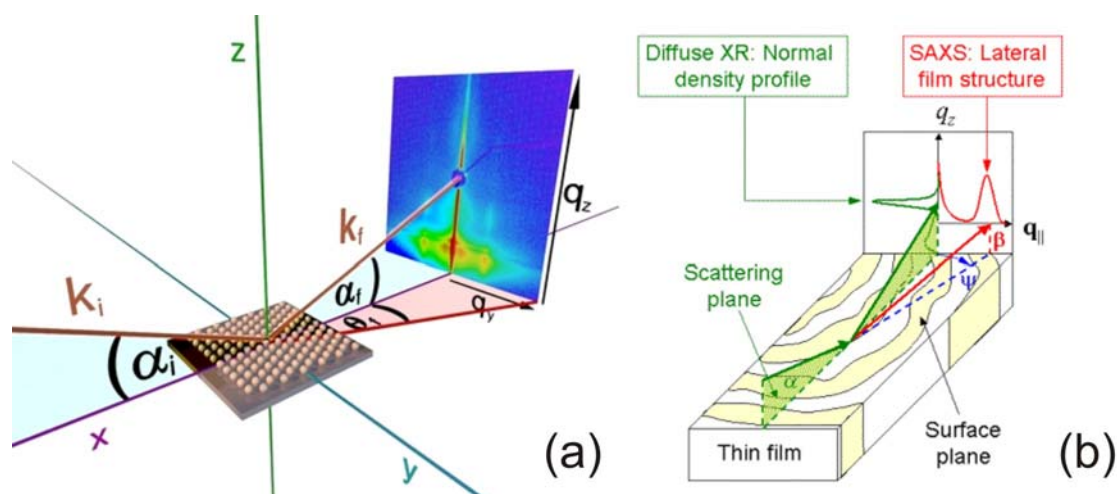
Scheme 3.2.12.1. *The geometry of a GISAXS experiment. a) A monochromatic x-ray beam with wave vector k_i is directed on a surface with incidence angle α_i with respect to the surface[73]. b) In the scattering plane GISAXS intensity distribution corresponds to a detector scan in diffuse reflectivity. Intensity distribution parallel to the surface plane corresponds to a line cut through the corresponding transmission SAXS pattern[74].*

The scattering vector in x, y, z directions is

$$q_{x,y,z} = \frac{2\pi}{\lambda}\begin{bmatrix} \cos(\alpha_f)\cos(2\theta_f) - \cos(\alpha_i) \\ \cos(\alpha_f)\sin(2\theta_f) \\ \sin(\alpha_f) + \sin(\alpha_i) \end{bmatrix}$$

Eqn.3.2.12.1

The scattering intensity for lateral electron fluctuations on the surface is given by

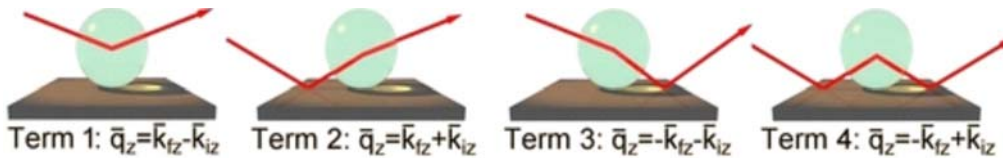$$I(q) = \left\langle |F|^2 \right\rangle S(q_{//})$$

Eqn.3.2.12.2

where F is the form factor and $S(q)$ is the total interference function, which describes the spatial arrangement with lateral correlation of the objects on the surface. $S(q)$ is the Fourier transform of the object position autocorrelation function. In Born approximation, F is the Fourier transform of the object shape and defined as

$$F(q) = \int_V \exp(iq \cdot r) d^3 r$$

Eqn.3.2.12.3

The reflection and refraction effects at the surface have to be considered, too. Thus, F should be calculated within the distorted wave Born approximation (*DWBA*). Scheme 3.2.12.2, taken from Ref.73, shows the physical picture of the calculation for scattering cross section in *DWBA*, given by

$$\frac{d\sigma}{d\Omega} \propto \left| F(q_{//}, k_{fz} - k_{iz}) + R(\alpha_i)F(q_{//}, k_{fz} + k_{iz}) + R(\alpha_f)F(q_{//}, -k_{fz} - k_{iz}) + R(\alpha_i)R(\alpha_f)F(q_{//}, -k_{fz} + k_{iz}) \right|^2$$

Eqn.3.2.12.4

$$I(q) = \left\langle |F_{DWBA}|^2 \right\rangle S(q_{//})$$

Eqn.3.2.12.5

Term 1: $\bar{q}_z = \bar{k}_{fz} - \bar{k}_{iz}$ Term 2: $\bar{q}_z = \bar{k}_{fz} + \bar{k}_{iz}$ Term 3: $\bar{q}_z = -\bar{k}_{fz} - \bar{k}_{iz}$ Term 4: $\bar{q}_z = -\bar{k}_{fz} + \bar{k}_{iz}$

Scheme 3.2.12.2. Four scattering events in DWBA[73].

These waves interfere coherently giving an effective *DWBA* form factor, F_{DWBA}. The classical form factor is transferred corresponding to the specific wave vector and Fresnel reflection coefficient *R*.

Microbeam grazing incidence small angle x-ray scattering (μGISAXS) experiments were performed at the beamline BW4, at DESY HASYLAB in Hamburg, where parabolic beryllium compound refractive lenses are used to obtain a micro-focused beam[75]. A micro-focused beamsize of 32×23 μm² (height × width), synchrotron radiation with a wavelength of 1.38 Å and incident on the sample surface at 0.74° were used for the measurements. The sample-detector distance for μGISAXS was adjusted to 2,2 m. The setup included a movable specular beamstop and a diode beamstop for detection of direct beam intensity. A 2d-MarCCD detector (2048×2048 pixels) was used to record the scattered x-rays from the surface.

3.2.17 Wide Angle X-ray Scattering (WAXS)

Wide angle x-ray scattering (WAXS) deals with the atomic structure of crystals. In WAXS the sample to detector distance is shorter compared to small angle x-ray scattering, thus the diffraction from larger angles is observed. Bragg peaks scattered to wide angles are analyzed to determine the crystalline structure of the matter. The Bragg equation

$$n\lambda = 2d \sin(\theta) \qquad \text{Eqn.3.2.10.1.}$$

where λ is the wavelength of the incident x-ray beam, *d* is the distance between atomic layers in a crystal and θ is the incidence angle, is used to reveal the crystallographic nature of the matter. The diffraction pattern gives information about the chemical or phase composition of the matter and preferred alignment of the crystallites. The scattering intensity is plotted as a function of the *2θ* angle[66].

The *θ-θ* measurements were conducted on a D8-Bruker-Advance2 diffractometer equipped with a Cu anode generated at a current of 30 mA and a voltage of 30 kV. Scans were taken in a *2Θ* range from 20° to 80° with a step size of 0.05° and integration time of 30 s.

# 4 Synthesis of "PDMS"-b-"PEO" amphiphilic block copolymers

Synthesis of PDMS-PEO diblock copolymers with less than 10000 g/mol molecular weight was accomplished by end coupling of PDMS and PEO blocks via hydrosilylation[76-79] resulting in very low yield after purification steps. With the same strategy PEO-PDMS-PEO triblock copolymers of <3000g/mol were synthesized[80]. Because of low yield and low molecular weight of the obtained blocks end coupling by hydrosilylation was avoided as the method to synthesize our desired block copolymer.

As the first route to start synthesizing a block copolymer, synthesis of "PDMS"-"PEO" block copolymer was tried by anionic polymerization. Anionic polymerization of ethylene oxide was initiated by potassium isopropanoxide in THF at room temperature. Then PEO was reacted with potassium which was covering the walls of the reaction flask as potassium mirror. 18-crown-6 ether was added before addition of hexamethyltricyclosiloxane (D_3) to solvate the cations and increase the concentration of the free silonalate ions, thus increase the reaction rate[81]. Although low molecular weight PEO could be converted to potassium alcoholate[81], we prepared higher molecular weight PEO. Thus, the conversion to potassium alcoholate was very low. Consequently PEO-b-PDMS could not be obtained by anionic sequential monomer addition. The other way around was also tried by trying to convert lithium alcoholate at the end of PDMS chain into potassium alcoholate by reacting with CH_3OK[82]. This macroinitiator was used for anionic polymerization of ethylene oxide (EO). Since oxyanions are not strong nucleophiles to start and precede polymerization of the other monomer in our EO-D_3 system, other synthetic routes than anionic polymerization were investigated.

End-coupling by using isocyanate and hydroxyl groups was next examined. Since cyanates and alcohols are very sensitive to moisture every step was done under nitrogen or argon atmosphere. Anionic polymerization of PDMS was stopped by 3-isocyanatopropylsimethylchlorosilane. PDMS was kept in its reaction bulb. Anionically synthesized PEO was terminated with HCl (g) and kept in its reaction bulb. Desired amounts of two polymers were taken from each bulb and transferred into a reaction flask in the glove box. The reflux set-up was closed at the top by a stopper and connected to argon flow, and anhydrous THF was used. Although different molecular weights of each polymer were synthesized anionically and tried to react, no end-coupling observed. Dibutyltinlaurate catalyst was also used to enhance the reaction of cyanate and alcohol groups[83]. From chain

statistics probability of finding the end group is highest in the middle of the polymer chain[84]. Although very dilute solutions of polymers were tried to react, these reactive groups could not react because of the PDMS or PEO around them. So, end-coupling trials were also unsuccessful.

Since anionic polymerization by sequential monomer addition and end coupling of isocyanate groups with hydroxyl groups were unsuccessful to obtain "PDMS"-"PEO" block copolymers, combination of different polymerization techniques via macroinitiator preparation was another strategy. An ATRP macroinitiator was prepared by anionic polymerization, and then polymerization of the second block was achieved by ATRP. Sec-butyllithium initiated anionic polymerization of PDMS in THF/cyclohexane was stopped by 3-(chlorodimethylsilyl) propyl 2-bromoisobutyrate which was synthesized according to literature[85]. As a first trial polymerization of a hydrophilic monomer, benzylmethacrylate (BMA), was tried. The reaction conditions were 30°C, in THF, by using pentamethyldiethylenetriamine (PMDETA) and Cu(I)Br (Scheme 4.1). PDMS-PBMA block copolymer was obtained with PDMS homopolymer presence which was revealed by HPLC (Figure 4.1.). PDMS macroinitiator was also run through the column with a synthesized molecular weight range poly (benzylmethacrylate) (PBMA) polymer. The peaks of both homopolymers exist inside the block copolymer peak. This indicated incomplete reaction of oxyanion at the end of PDMS chain with the ATRP initiator, and unsuccessful removal of excess ATRP initiator after reacting with PDMS, because after polymerization of BMA, PBMA homopolymer was also present. Since the first trial was to obtain an amphiphilic block copolyme in 1:1 ratio in molecular weight, it was not easy to separate the block copolymer and homopolymers due to small difference in their molecular weights.
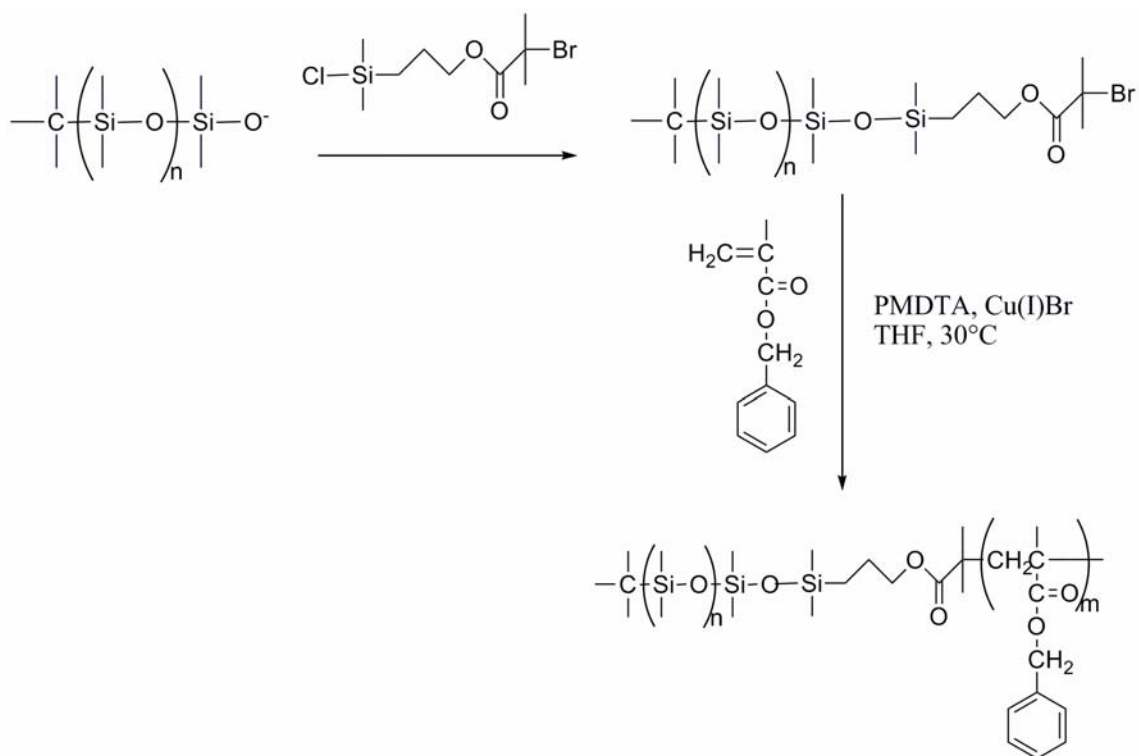
Scheme 4.1. *Synthesis scheme of PDMS-b-PBMA by combination of anionic polymerization with ATRP.*
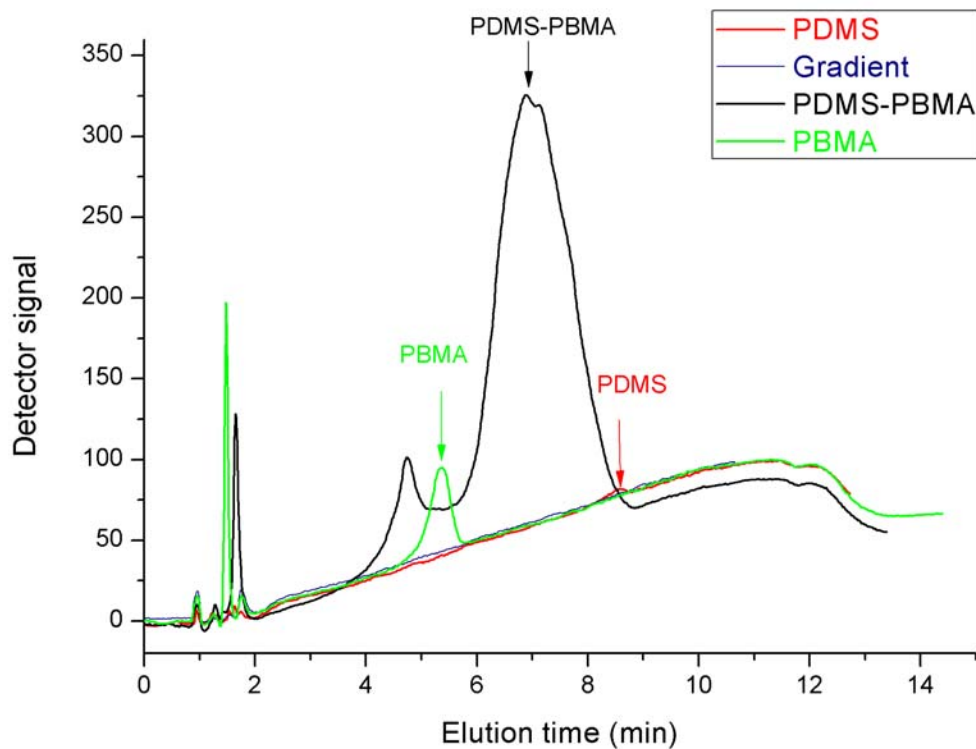

Figure 4.1. *HPLC of PDMS-b-PBMA with PDMS macroinitiator and a PBMA standard polymer in the synthesized molecular weight range.*

Combination of two different synthetic ways was found to yield polymeric reaction products. The problem was now to achieve better attachment of ATRP initiator to PDMS chain. For this reason, anionic polymerization of PDMS was stopped by 3-aminopropylmethylbis (trimethylsiloxy) silane. Then this amino end functionalized PDMS was reacted with N-hydroxysuccinimidyl 2-bromo-2-methylpropionate (NBS) to obtain an ATRP initiator (Scheme 4.2). Two different molecular weight PDMS polymers were used for these reactions. ATRP was conducted at 30°C, in THF, by using PMDETA and Cu(I)Br. No block copolymer could be obtained. This can be due to descending yield in successive reactions in multi steps instead of one step reaction, and inefficient initiator and ligand usage; however the system was not tried again.
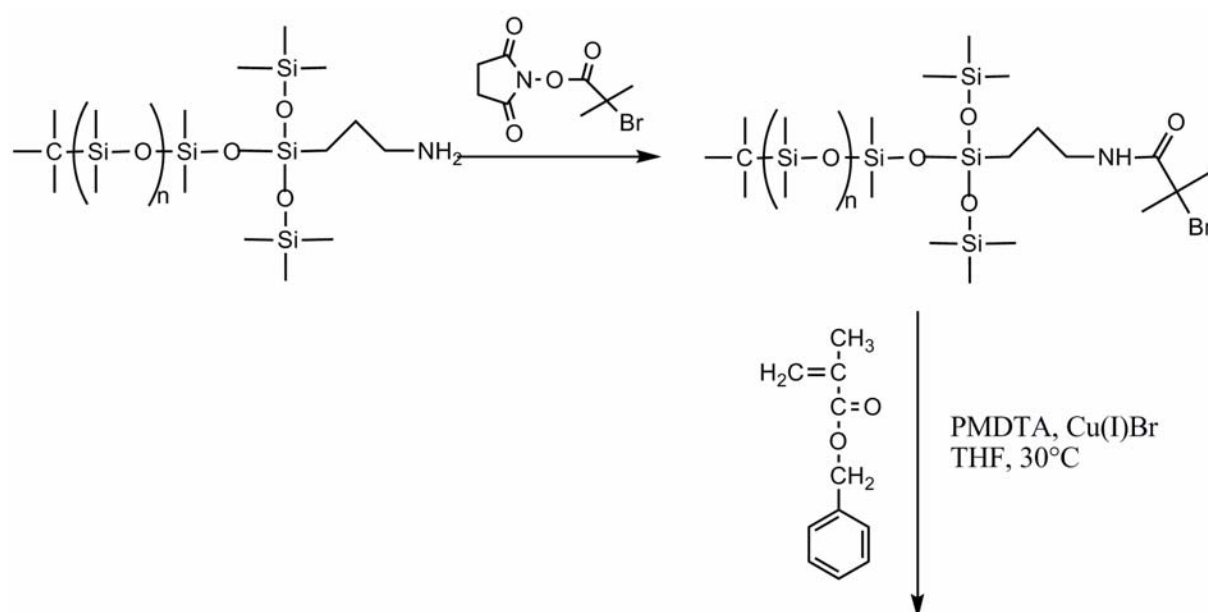
Scheme 4.2. *Schematic representation of ATRP initiator attachment by reacting amino groups at the end of PDMS with NBS.*

After observing an amphiphilic block copolymer synthesis by using a PDMS macroinitiator via ATRP, efficient attachment of ATRP initiator to PDMS was the primary goal. It was achieved by reacting hydroxyl end groups of a telechelic PDMS with 2-bromo-2-methylpropionyl bromide[86]. This PDMS macroinitiator was reacted with poly (ethyleneglycol) acrylate [$CH_2=CHCO(OCH_2CH_2)_n$-OH], and resulted in a cross linked polymer. To protect the oxygen in the monomer, poly (ethyleneglycol) methyl ether

methacrylate [(PEO)MA] that has a methyl group instead of the hydrogen compared to the previous monomer was polymerized and crosslinking was prevented. Poly(ethyleneglycol)methylethermethacrylate-block-poly(dimethylsiloxane)-block-poly(ethyleneglycol)methylethermethacrylate [(PEO)MA-PDMS-MA(PEO)] triblock copolymer was obtained. The synthesis and characterization of the triblock copolymer is explained in the following section. Diblock copolymers of the same type, by using mono hydroxyl end functionalized PDMS were also synthesized; PDMS-(PEO)MA (Section 4.2). Starting from PEO and converting into an ATRP initiator and polymerization of (PDMS)MA resulted in PEO-MA(PDMS) diblock copolymer and explained in Section 4.3.

4.1   (PEO)MA-PDMS-MA(PEO)

(PEO)MA-PDMS-MA(PEO) triblock copolymer was synthesized by ATRP of poly (ethyleneglycol) methyl ether [(PEO)MA] monomer after preparation of a difunctional PDMS macroinitiator. Synthesis steps are illustrated in Scheme 4.1.1.
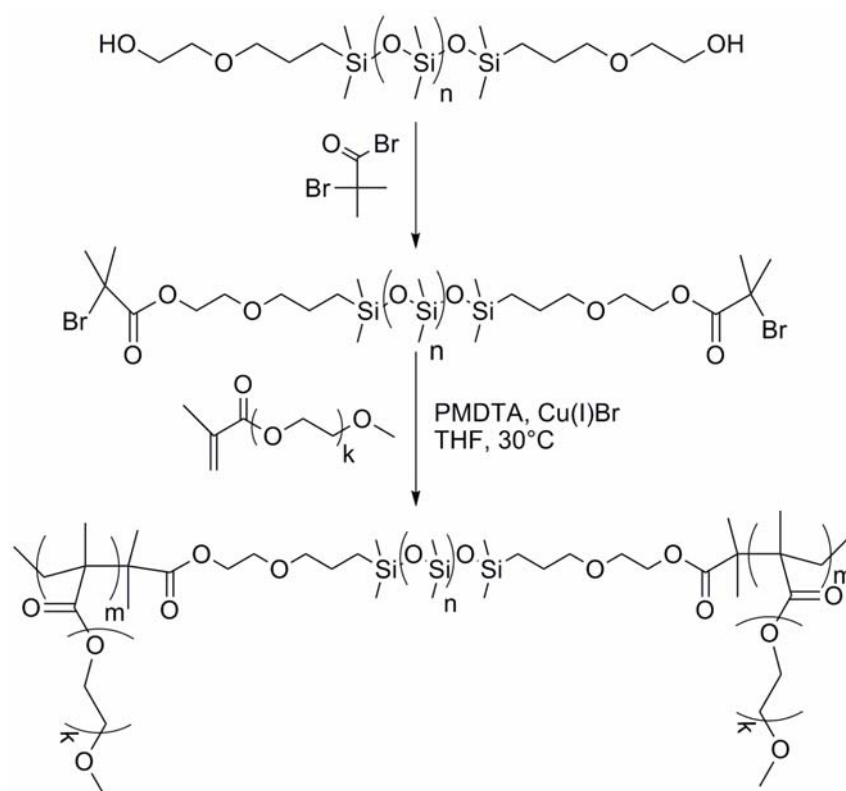
Scheme 4.1.1. *(PEO)MA-PDMS-MA(PEO) synthesis steps.*

41

4.1.1 Macroinitiator preparation

Dihydroxyl end functionalized PDMS was converted to an ATRP initiator as described by Huan et al[86]. 10 g (2.4 mmol) HO-PDMS-OH was dissolved in 400 ml anhydrous THF. 1.56 ml (11.1 mmol) anhydrous triethylamine (TEA) was added to stirred solution, followed by addition of 0.97 ml (5.55 mmol) 2-bromo-2-methylpropionyl bromide. The mixture was left for stirring overnight at ambient temperature. It was filtered by suction filter to remove the bromide salt, and the solvent was evaporated under vacuum. The resulting colorless oil was diluted with 400 ml dichloromethane (CH_2Cl_2) and put into an extraction funnel and washed with saturated sodium bicarbonate ($NaHCO_3$) solution. The organic layer was isolated and dried over anhydrous magnesium sulfate ($MgSO_4$). The difunctional macroinitiator was 9.5 g, with 76% yield.

The ^1H NMR spectra of dihydroxyl end functionalized PDMS and dibromo end functionalized PDMS are shown in Figure 4.1.1. The broad peak at 1.89 ppm corresponding to the hydroxyl groups on dihydroxyl end functionalized PDMS (spectra on top) disappeared after esterification reaction with 2-bromo-2-methylpropionyl. The appearance of two singlet peaks at 1.94 ppm, 2.00 ppm (($CH_3)_2CBr$) (spectra at the bottom) indicated the completeness of the reaction. The methylene peaks indicated by "e, f, g" shifted downfield when oxygen was replaced by Br.
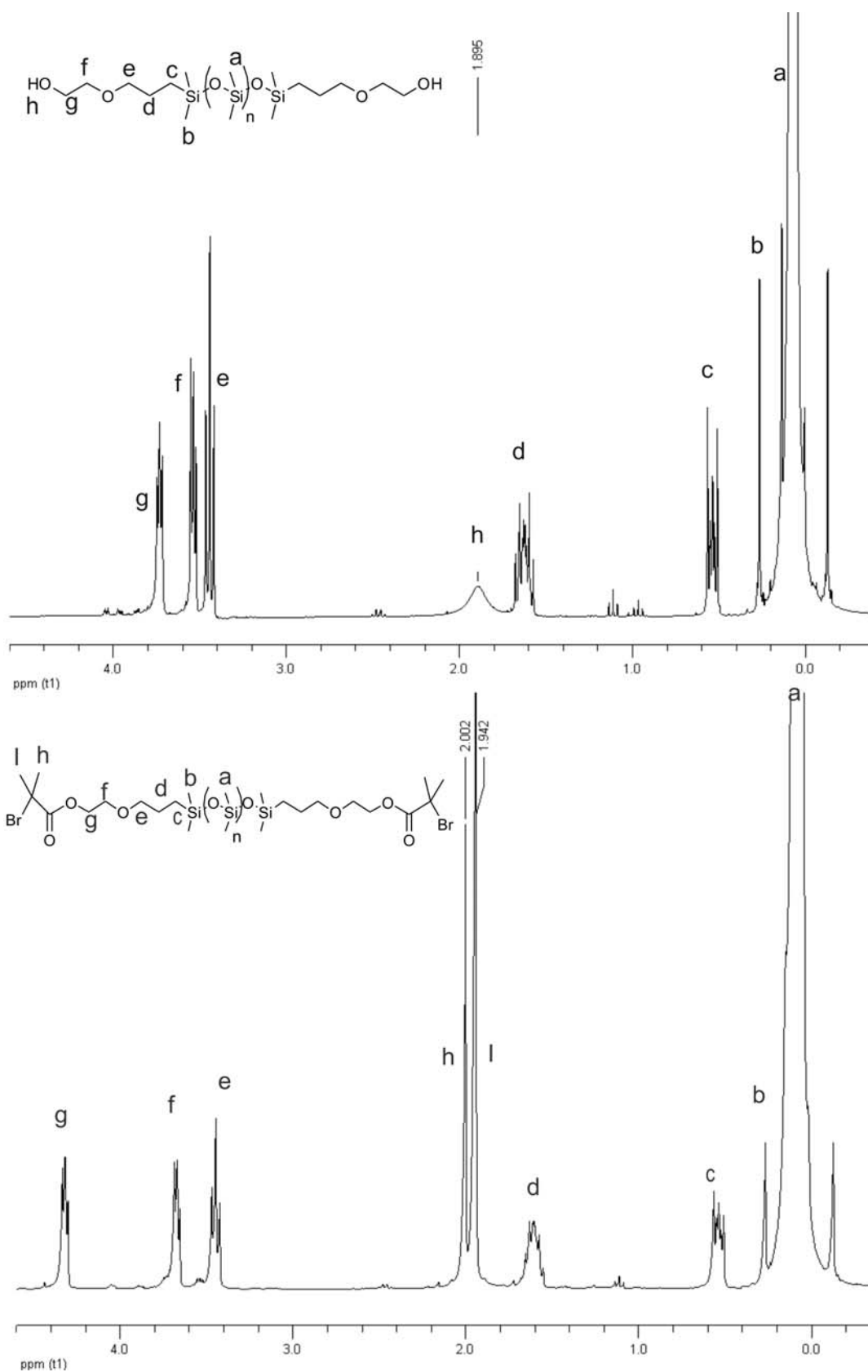
Figure 4.1.1.1. ^1H NMR spectra of dihydroxyl (top) and dibromo (bottom) end functionalized PDMS. OH peak at 1.89 ppm disappeared, singlets at 2.00 and 1.94 ppm appeared for methyl groups next to bromine.

4.1.2 Polymerization of (PEO)MA with macroinitiator

4.04 g (0.95 mmol) of Br-PDMS-Br was put into a reaction flask with a magnetic stirrer. Vacuum was applied to remove residual solvent. Then it was flushed with Argon. Addition of 12 ml dry THF was followed by 6.74 g (14.16 mmol) of poly (ethyleneglycol) methyl ether methacrylate [(PEO)MA], 0.205 g (1.44 mmol) of Cu(I)Br and 330 μl (1.58 mmol) of pentamethyldiethylenetriamine (PMDETA). All reactants were flushed with Argon prior to addition. Three cycles of freeze-thaw were applied to remove any oxygen from the reaction medium. The polymerization was concluded at 32°C under Argon for 15 h. The reaction was stopped by exposure to air, and DOWEX ion exchanger was added. The mixture was filtrated by passing through aluminum oxide (Al_2O_3), and centrifuged at 4000 rpm for 15 min. Clear solution above Al_2O_3 was taken and solvent was evaporated. The triblock copolymer was obtained as a clear viscous liquid, 10.68 g, with 95% yield.

The ^{1}H NMR spectra of the reactants; macroinitiator (top), (PEO)MA monomer (center) where double bond peaks of magnified in the inlet and the product; triblock copolymer (bottom), are given in Figure 4.1.2.1. The polymerization is realized by disappearance of double bond peaks and appearance of PEO and PDMS peaks at the same spectrum (bottom): PEO methylene (CH_2) triplet peak at 3.64 ppm with the singlet peak at 3.37 ppm for the methyl ether at the end of the PEO chain and peak for PDMS methyl groups (CH_3) at 0.05 ppm.

The number-average molecular weight of the triblock copolymer is about M_n = 9300 g/mol with a polydispersity D = 1.68. The molecular weight distribution of the triblock copolymer from GPC measurement is given in Figure 4.1.2.2. GPC was calibrated with PDMS standards. Since the triblock copolymer is composed of (PEO)MA parts in addition to PDMS, the exact value is inaccurate but presence of only triblock copolymer is seen. The molecular weight of the dihydroxyl end functionalized PDMS was around 4200 g/mol from GPC measurement. By comparing the integrals of the NMR peaks, the molecular weight of the (PEO)MA-blocks is estimated as M_n[(PEO)MA] ≈ 2000 g/mol. From these, degree of polymerization of (PEO)MA monomer was calculated to be 5. (PEO)MA monomer has a molecular weight of 476 g/mol, corresponding to 8 repeating units in PEO chain. PDMS macroinitiator has 52 repeating units. Thus (PEO)MA-PDMS-MA(PEO) triblock copolymer contains short methacrylate chains with short PEO side groups.
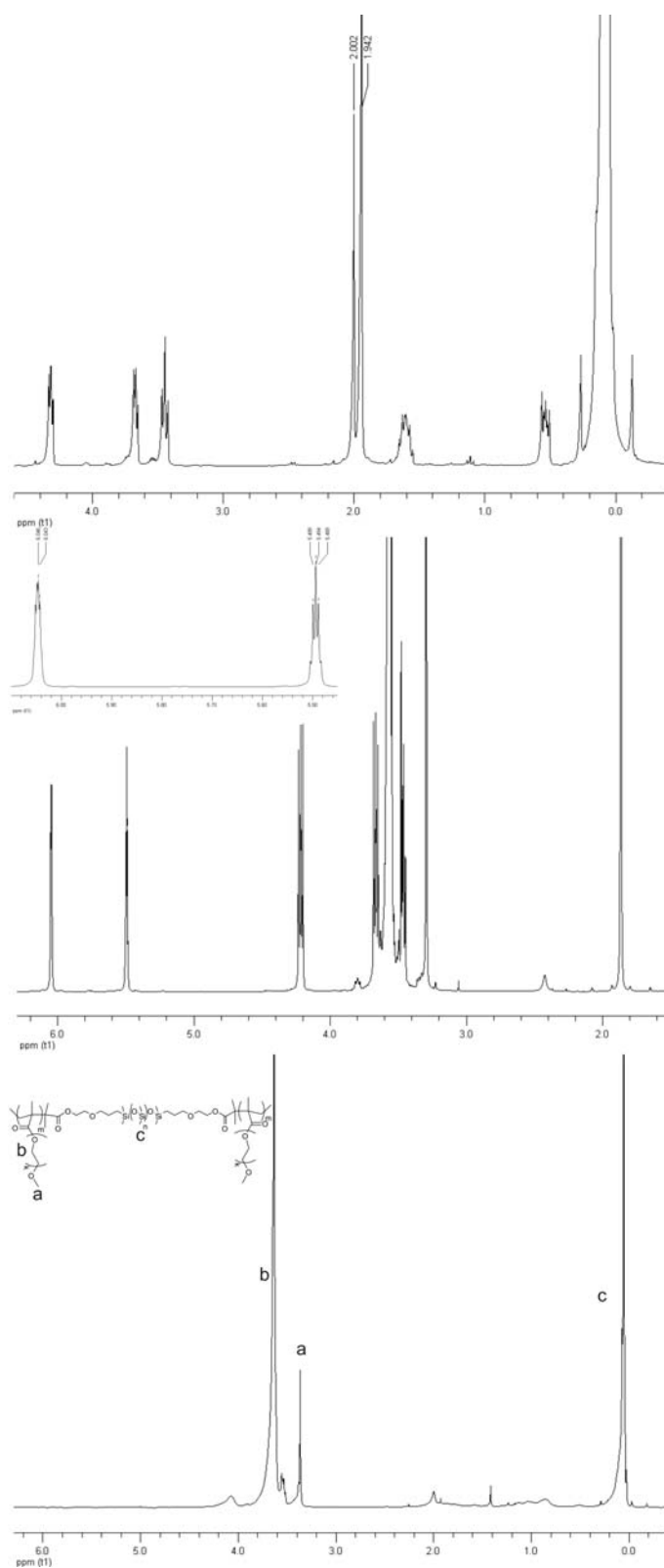
Figure 4.1.2.1. *^{1}H NMR spectra of the macroinitiator (top), (PEO)MA monomer with monomer peaks inlet (center) and (PEO(MA-PDMS-MA(PEO) (bottom). Double bond peaks of monomer disappeared, and PEO and PDMS peaks are present in the triblock copolymer with corresponding peaks coming from the macroinitiator and the monomer.*
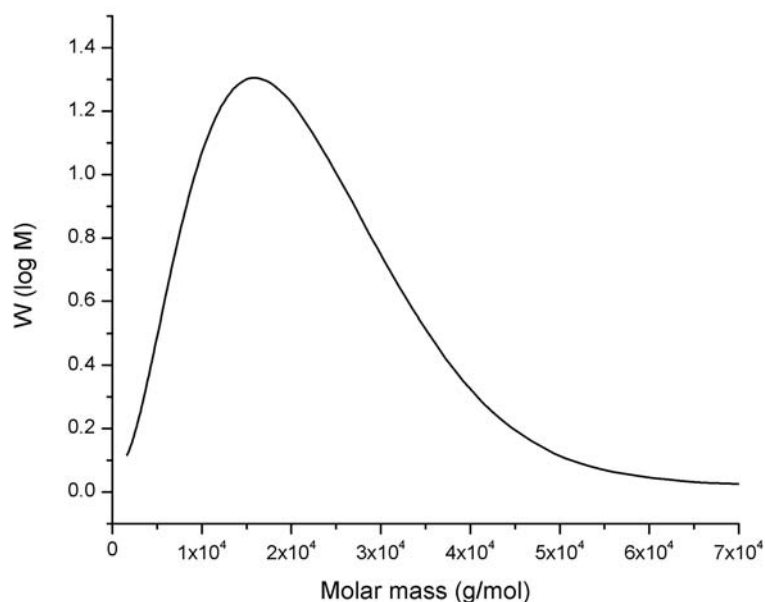
Figure 4.1.2.2. *Molecular weight distribution of (PEO)MA-PDMS-MA(PEO) from GPC.*

In the DSC thermogram of (PEO)MA-PDMS-MA(PEO) (Figure 4.1.2.3), second heating curve is shown. A glass transition temperature of -136°C for PDMS, -66.9°C corresponding to that of PEO, a crystallization temperature of -28.6°C corresponding to the cold crystallization of PDMS and a melting temperature of –5.8°C for PDMS are seen. The T_g of PDMS is in range between -144 to -123°C and that of PEO is in range between-72 to-65°C[87]. The glass transition temperatures obtained from the triblock copolymer correspond to those of the corresponding homopolymers indicating phase separated block copolymers. Very low T_g of PDMS arises from its highly flexible chain. The reasons for this extraordinary flexibility can be seen in Scheme 4.1.2.1.
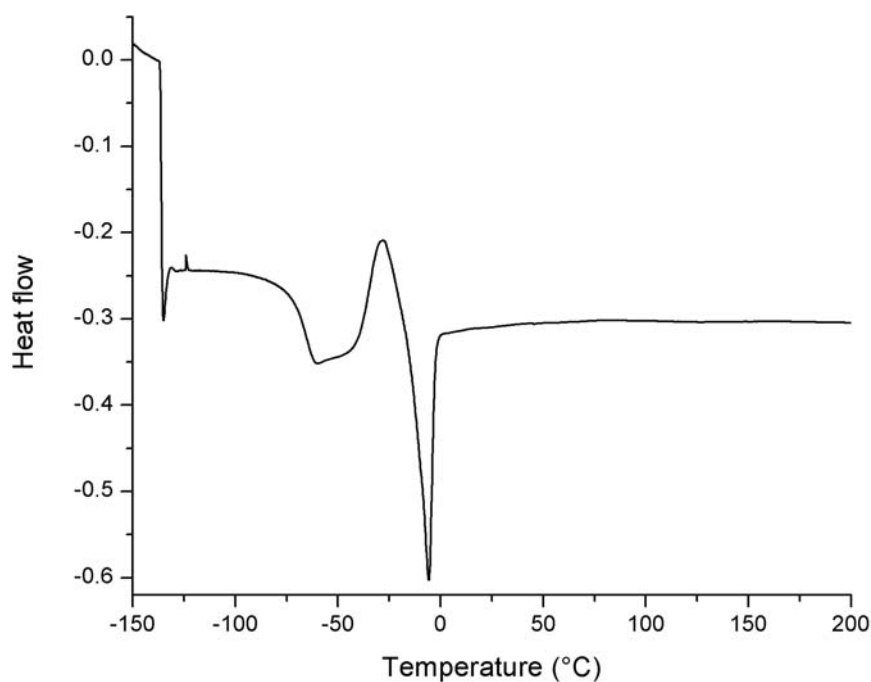
Figure 4.1.2.3. *DSC thermogram of (PEO)MA-PDMS-MA(PEO); second heating curve. T_g of PDMS=-136°C, T_g of PEO=-66.9°C, cold crystallization temperature of PDMS=-28.6°C and corresponding T_m=-5.8°C are observed.*
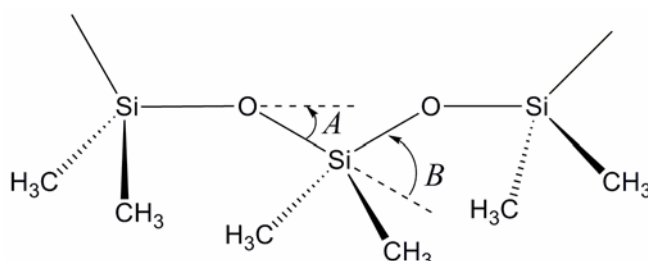
Scheme 4.1.2.1. *PDMS chain showing some structural information relevant to its high flexibility[88].*

The Si-O skeletal bond has a length of 1.64 Å which is longer than that of a C-C bond, 1.53 Å. Because of this, intramolecular crowding or steric interferences are diminished[28]. The oxygen atoms in the backbone of a polymer skeletal are as small as an atom can be and still have the multivalency needed to continue a chain structure. The Si-O-Si bond angle, 180°-*A* in Scheme 4.1.2.1, of ~143° is wider than the usual tetrahedral bond angle of ~110°. These three structural features have the effect of increasing the dynamic flexibility of the chain[89] and the equilibrium flexibility, which is the ability of a chain to be compact when in the form of a random coil.

47

In addition to the low glass transition resulting from the behavior explained above, cold crystallization of PDMS is observed in the triblock copolymer, with the following melting. Crystallization of PDMS in (PEO)-PDMS-(PEO) triblock copolymer was studied by Dollase et.al.[90]. They observed enhancement of PDMS crystallization by PEO part in the triblock copolymer compared to corresponding PDMS and PEO polymer blends.

PDMS is the larger block in (PEO)MA-PDMS-MA(PEO), with 52 repeating units, whereas PEO in the side chain is only 8 repeating units. Thus, melting of PEO could not be observed. Instead characteristic of the larger block is seen. This is the unique feature of our triblock copolymer. It has polymer brushes at each end. DSC shows all characteristics of the higher molecular weight part, linear PDMS. Short PEO chains are not enough to form crystallites.

Presence of two T_gs shows that the triblock copolymer is phase separated. The morphology of the (PEO)MA-PDMS-MA(PEO) in bulk was investigated by small angle x-ray scattering. The triblock copolymer shows hexagonally packed cylindrical (HCPC)[30] microdomain morphology at room temperature, as evidenced by higher order reflections at q values 1:√3:√4 relative to the first-order peak. SAXS curve with Gaussian fits to the mentioned peaks are given in Figure 4.1.2.4. All the fits have the same width as the primary peak. The primary peak is at 0.03205 Å^{-1}. Using Eqn.3.2.9.10 a center to center distance of 19.6 nm is obtained. This distance can be correlated to the center to center distance between cylinders according to the structure of hexagonally packed cylinder morphology.
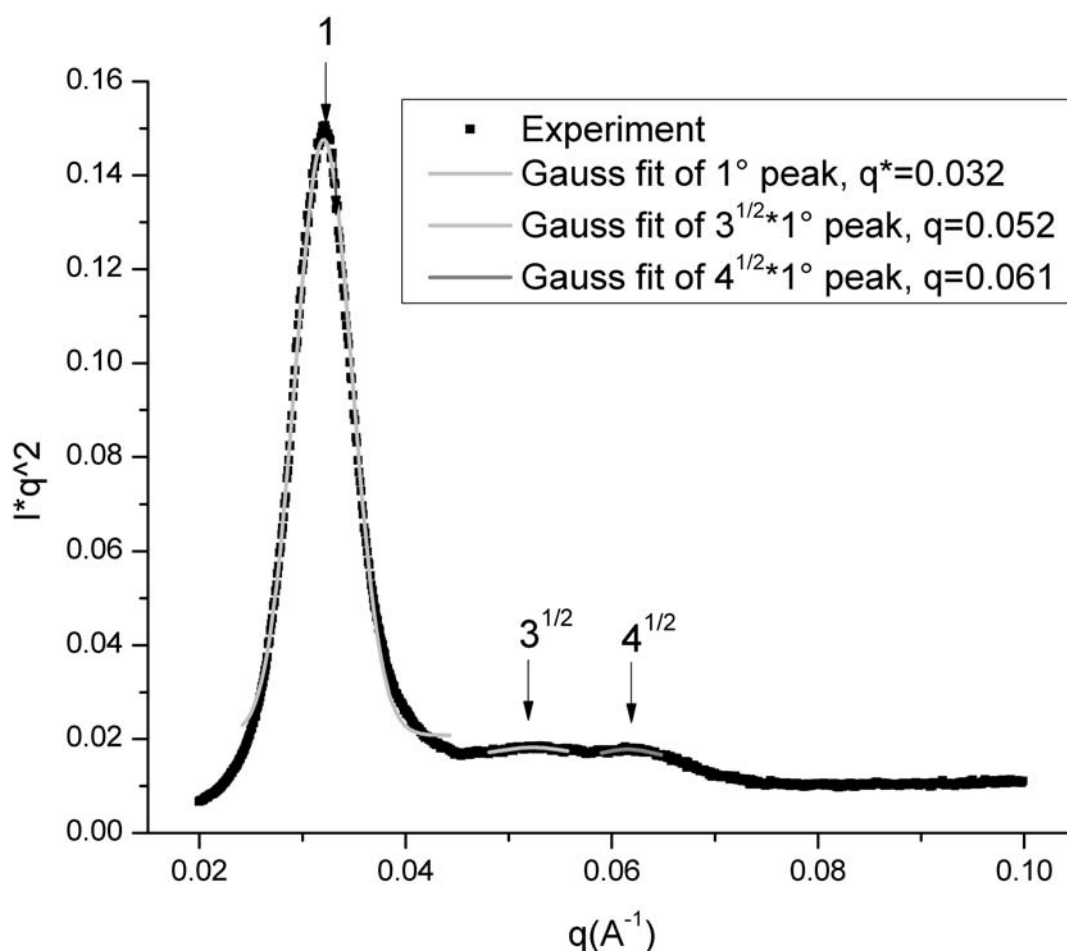
Figure 4.1.2.4. *SAXS curve of (PEO)MA-PDMS-MA(PEO) at 30°C with Gauss fits for primary peak and higher order reflections at q values 1:√3:√4 relative to the first-order peak having the same width as the first order peak.*

To further investigate the (PEO)MA-PDMS-MA(PEO) morphology, (PEO)MA-PDMS-MA(PEO) thin film was investigated by scanning force microscopy (SFM). Figure 4.1.2.5 shows the height image of a thin triblock copolymer film which was prepared by spin-coating 1% by weight (PEO)MA-PDMS-MA(PEO)/THF solution on Si wafer, and kept in oven at 70°C overnight. The measurement was repeated with different cantilevers having different spring constants. Since the block copolymer is a gel at room temperature, a cantilever with a lower spring constant was preferred to increase the observed contrast in SFM. Due to the applied amplitude set-point, a contrast was observed in the height image. When this image's power spectral density is calculated, the center to center distance of the spheres is found to be around 22nm. This is in correlation with the value obtained from the primary peak in SAXS measurement which gives a distance value of around 20 nm.
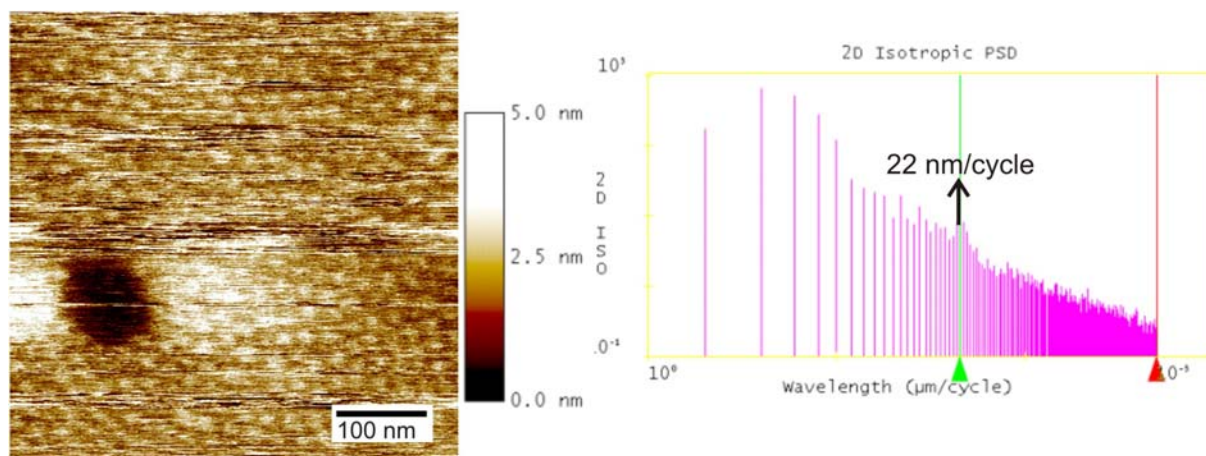
Figure 4.1.2.5. SFM height image of thin (PEO)MA-PDMS-MA(PEO) film (left) with corresponding power spectral density (right). The center to center distance in the height image is 22 nm as indicated by power spectral density calculation.

To obtain information on the stability of the ordered morphology of the triblock copolymer, temperature dependent SAXS measurements were conducted from 30° to 200°C, by 10°C intervals. To observe the T_{ODT}, 2°C interval measurements from 160°C to 198°C were performed. The primary peak of each measurement was fitted with Gaussian curve and half widths of the peaks were recorded. Figure 4.1.2.6 shows the plot of (peak width)^2 vs 1/T. The order to disorder transition of the block copolymers was investigated by using the plots of the square of the half width of the first-order scattering maximum versus 1/T. These plots have a theoretical basis of mean field theory[91]. The square of the half widths of the first order scattering maximum shows a temperature dependency, and a discontinuity is observed near a critical temperature, here the order to disorder transition temperature. The dashed lines in Figure 4.1.2.6 limit the T_{ODT} range. The order to disorder temperature (ODT) of the triblock copolymer is ~170°C.

There is different viscoelastic contrast between the ordered and disordered states of a block copolymer. Thus, low frequency rheology is very sensitive for detecting the dissolution of ordered microstructures[91-94]. The rheology measurement for the triblock copolymer was done in the temperature range between 173°K and 433°K (Fig. 4.1.2.7). Storage modulus decreases at the glass transition temperature of PEO (~213°K) and makes a long range rubbery plateau until it starts decreasing close to the order to disorder temperature. This behavior shows that the triblock copolymer is ordered and phase separated in temperature range 250-375 °K (-20 to 100°C). At 410°K storage modulus coincides with the loss modulus, and after this

temperature polymer flows, G''>G' (inlet in Fig. 4.1.2.7). At room temperature (PEO)MA-PDMS-MA(PEO) has hexagonally packed cylindrical morphology. Rheology measurement at 30°C with 3%strain (Fig. 4.1.2.8-a), shows a behavior similar to that of the hexagonally packed cylinder phase of poly (ethyleneoxide)-poly (isoprene) diblock copolymer[56, 95]. The moduli at 30°C are one order of magnitude higher than those at the temperature where the moduli coincide, 140°C (Fig. 4.1.2.8-b). Polymer flows after this temperature and does not show the same mechanical strength as at 30°C.
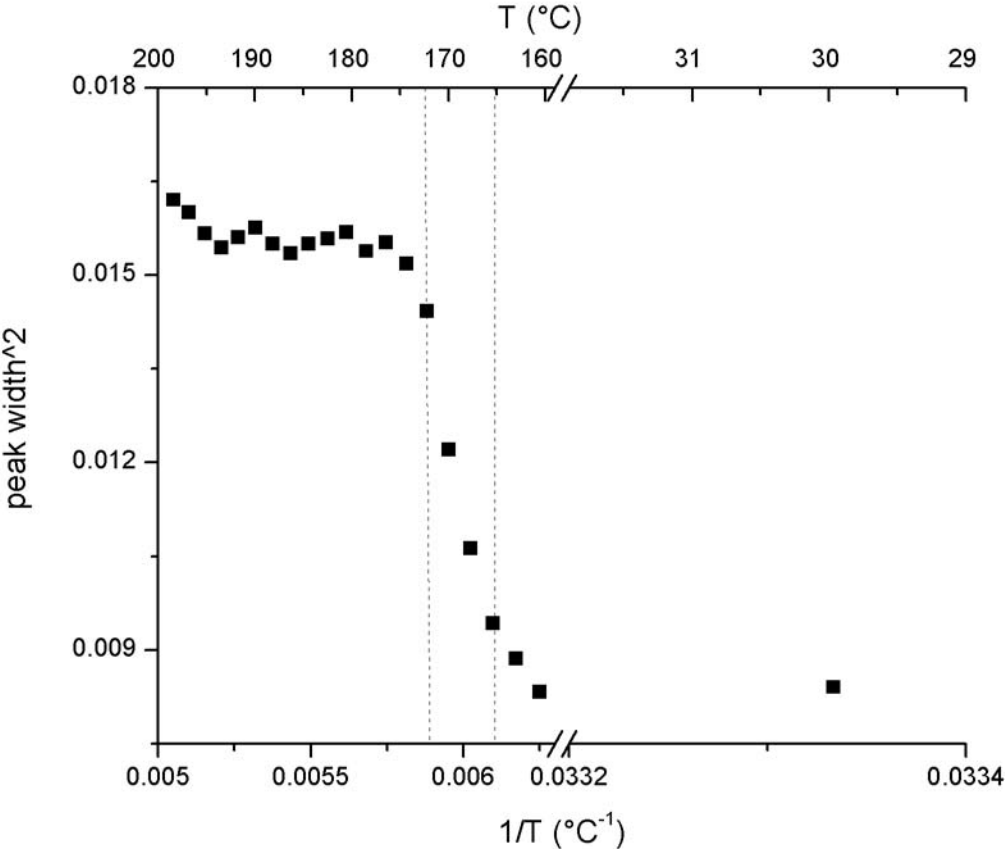
Figure 4.1.2.6. *Plot of (peak width)^2 versus 1/T for (PEO)MA-PDMS-MA(PEO) from 160°C to 198°C in 2°C intervals with the one at 30°C. The order to disorder transition occurs in the range between the dashed lines, close to 170°C.*
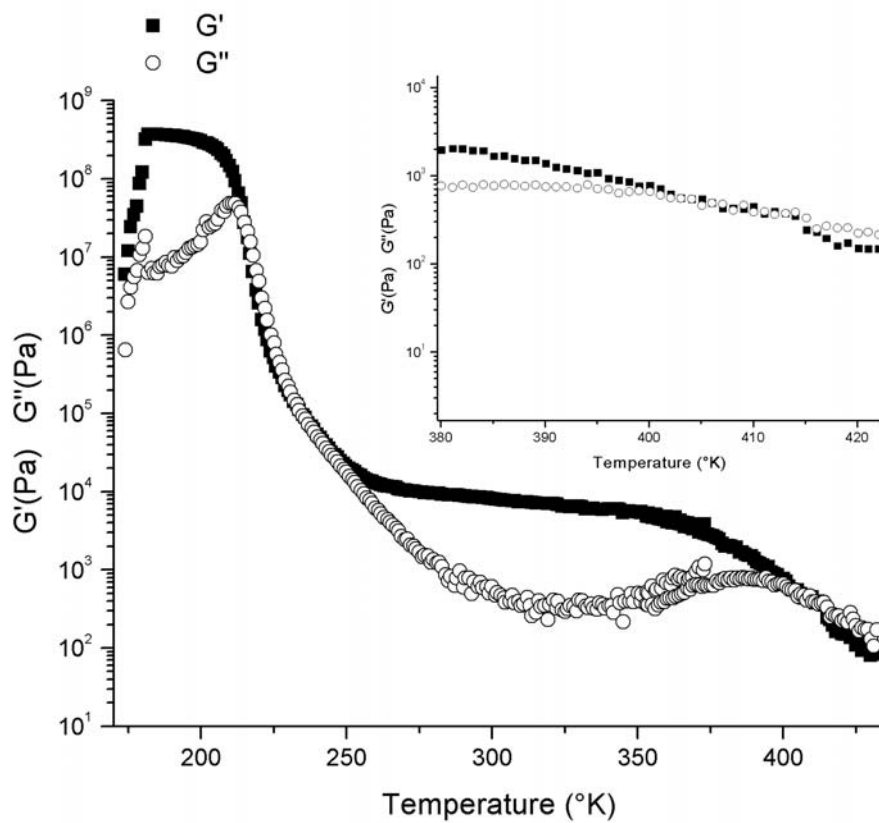
Figure 4.1.2.7. *Temperature dependence of storage (G') and loss moduli (G") of (PEO)MA-PDMS-MA(PEO). In the inset, the same plot is zoomed in where G' and G" coincide.*
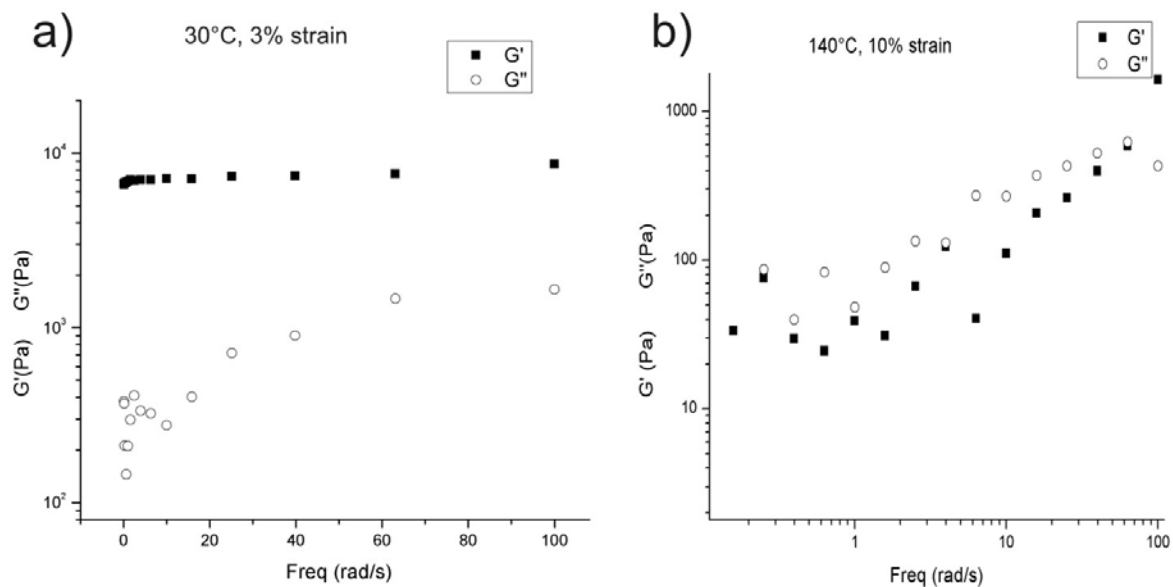

Figure 4.1.2.8. *Frequency measurements of (PEO)MA-PDMS-MA(PEO) at 30°C, 3% strain (a)and 140°C, 10% strain (b).*

4.2   PDMS-MA(PEO)

Mono hydroxyl end functionalized different molecular weight, ~5000 g/mol and 10000 g/mol, PDMSs were converted to monofunctional ATRP initiators by using the same route in difunctional initiator preparation. The block copolymer synthesis was continued with the polymerization of the poly (ethyleneglycol) methyl ether methacrylate [(PEO)MA].

4.2.1   Macroinitiator preparation

10 g (2 mmol) of ~5000 g/mol PDMS-OH was dissolved in 300 ml anhydrous THF. 1.4 ml (10 mmol) TEA was added to stirred solution. After addition of 0.62 ml (5 mmol) 2-bromo-2-methylpropionyl bromide, the mixture left for stirring overnight at room temperature. The bromide salt was removed by filtering, and the solvent was evaporated under vacuum. The resulting colorless oil was diluted with 400 ml CH_2Cl_2 and put into an extraction funnel and washed with saturated $NaHCO_3$ solution. The organic layer was isolated and dried over anhydrous $MgSO_4$, and the macroinitiator was 8.8 g.

In the same way, 10 g (1mmol) of ~10000 g/mol PDMS-OH was dissolved in 300 ml anhydrous THF. 0.7 ml (5 mmol) TEA was added to stirred solution. After addition of 0.31 ml (2.5 mmol) 2-bromo-2-methylpropionyl bromide, the mixture left for stirring overnight at room temperature. The bromide salt was removed by filtering, and the solvent was evaporated under vacuum. The resulting colorless oil was diluted with 400 ml CH_2Cl_2 and put into an extraction funnel and washed with saturated $NaHCO_3$ solution. The organic layer was isolated and dried over anhydrous $MgSO_4$. The macroinitiator was 9.03 g.

4.2.2   Polymerization of (PEO)MA with macroinitiator

3 g (0.6 mmol) of ~5000g/mol PDMS-Br was dissolved in 20 ml THF while purging argon through the flask. The inhibitor of THF was removed previously by passing through Al_2O_3 column.3 g (6.3 mmol) of (PEO)MA and 125 µl (0.6 mmol) PMDETA were flushed with argon prior to their addition into the reaction flask. After addition of 86 mg (0.6 mmol) Cu(I)Br, three cycles of freeze-thaw were applied to remove any oxygen from the reaction medium. The polymerization was concluded at 32°C under Argon for 6 days. The reaction was stopped by exposure to air, and DOWEX ion exchanger was added. The mixture was filtrated by passing through Al_2O_3, and centrifuged at 4000 rpm for 15 min. Clear solution

above Al$_2$O$_3$ was taken and solvent was evaporated. The diblock copolymer was obtained as a clear viscous liquid.

3 g (0.3 mmol) of ~10000g/mol PDMS-Br was dissolved in 20 ml THF while purging argon through the flask. 3 g (6.3 mmol) of (PEO)MA and 63 μl (0.3 mmol) PMDETA were flushed with argon prior to their addition into the reaction flask. After addition of 43 mg (0.3 mmol) Cu(I)Br, three cycles of freeze-thaw were applied to remove any oxygen from the reaction medium. The polymerization was concluded at 32°C under Argon for 6 days. The reaction was stopped by exposure to air, and DOWEX ion exchanger was added. The mixture was filtrated by passing through Al$_2$O$_3$, and centrifuged at 4000 rpm for 15 min. Clear solution above Al$_2$O$_3$ was taken and solvent was evaporated. The diblock copolymer was obtained as a clear viscous liquid.

In the NMR spectra of both diblock copolymers (Figure 4.2.2.1) typical peaks for PDMS and PEO repeating units with methacrylate backbone (in range 0.5-2.2 ppm) are observed. Both spectra are the same, since the only difference in the block copolymers is their molecular weight. 5000 g/mol PDMS containing block copolymer [PDMS(5000)-MA(PEO)] has a molecular weight around 8000 g/mol, whereas that of 10000 g/mol PDMS containing diblock copolymer [PDMS(10000)-MA(PEO)] is ~16000g/mol. The aim was to synthesize 1:1 ratio in the molecular weights of the single blocks. Molecular weight distributions obtained from GPC are shown in Figure 4.2.2.2.

In DSC thermograms, T$_g$ of PDMS at -137°C and that of PEO at -66°C, with cold crystallization of PDMS at -30°C and corresponding melting at -6°C are observed (Fig. 4.2.2.3). In PDMS(5000)-MA(PEO) thermogrram after melting of PDMS the slope of the curve increased. This should be an error related to the instrument.
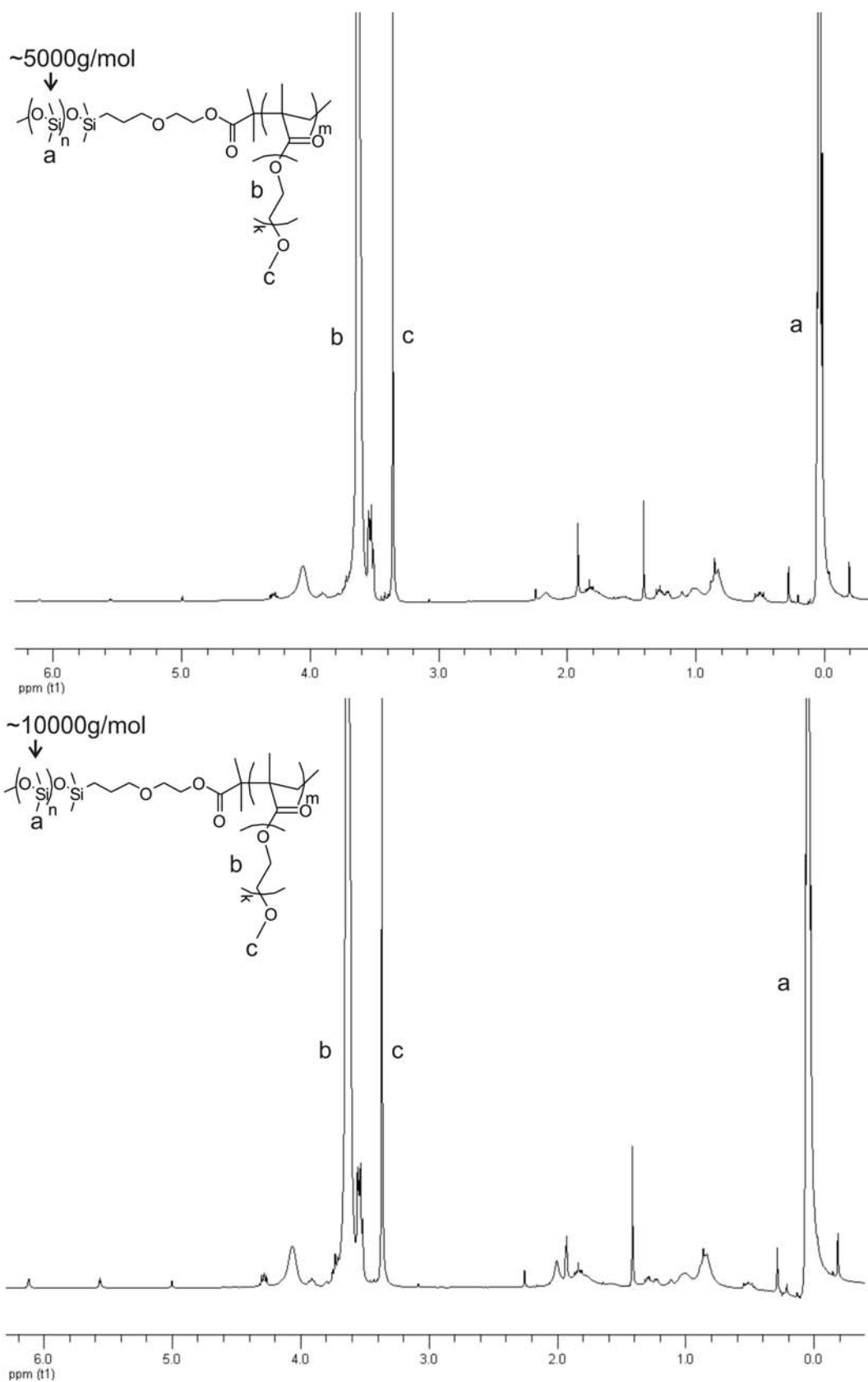
Figure 4.2.2.1. *¹H NMR spectra of PDMS-MA(PEO) diblock copolymers, PDMS(5000)-MA(PEO) on top, PDMS(10000)-MA(PEO) at the bottom.*
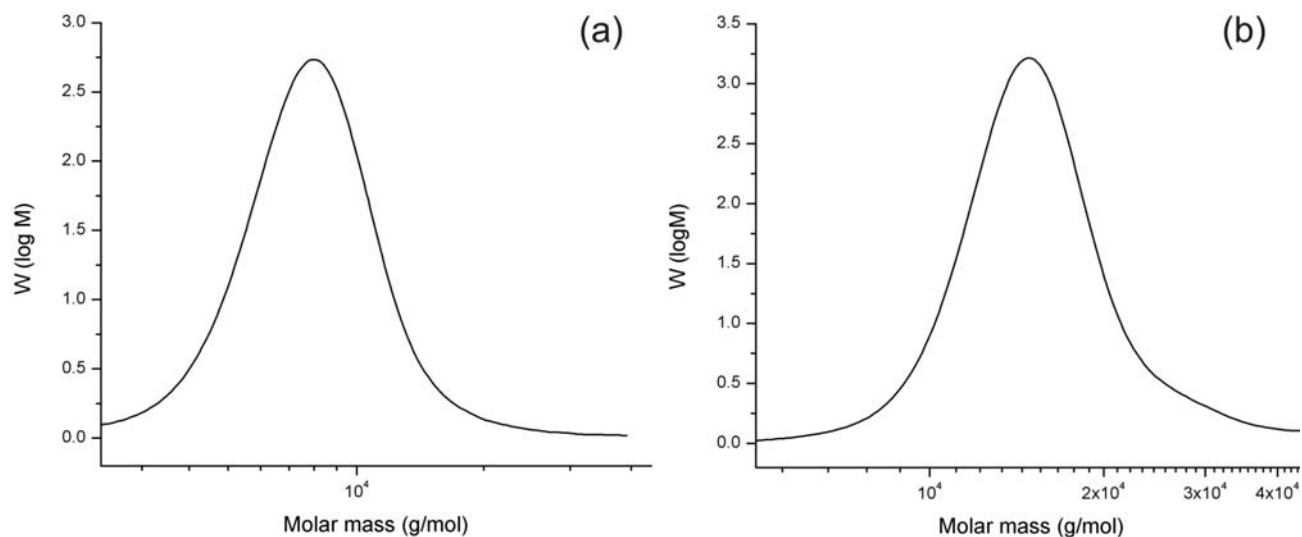
Figure 4.2.2.2. *Molecular weight distributions of a) PDMS(5000)-MA(PEO) and b) PDMS(10000)-MA(PEO) diblock copolymers.*
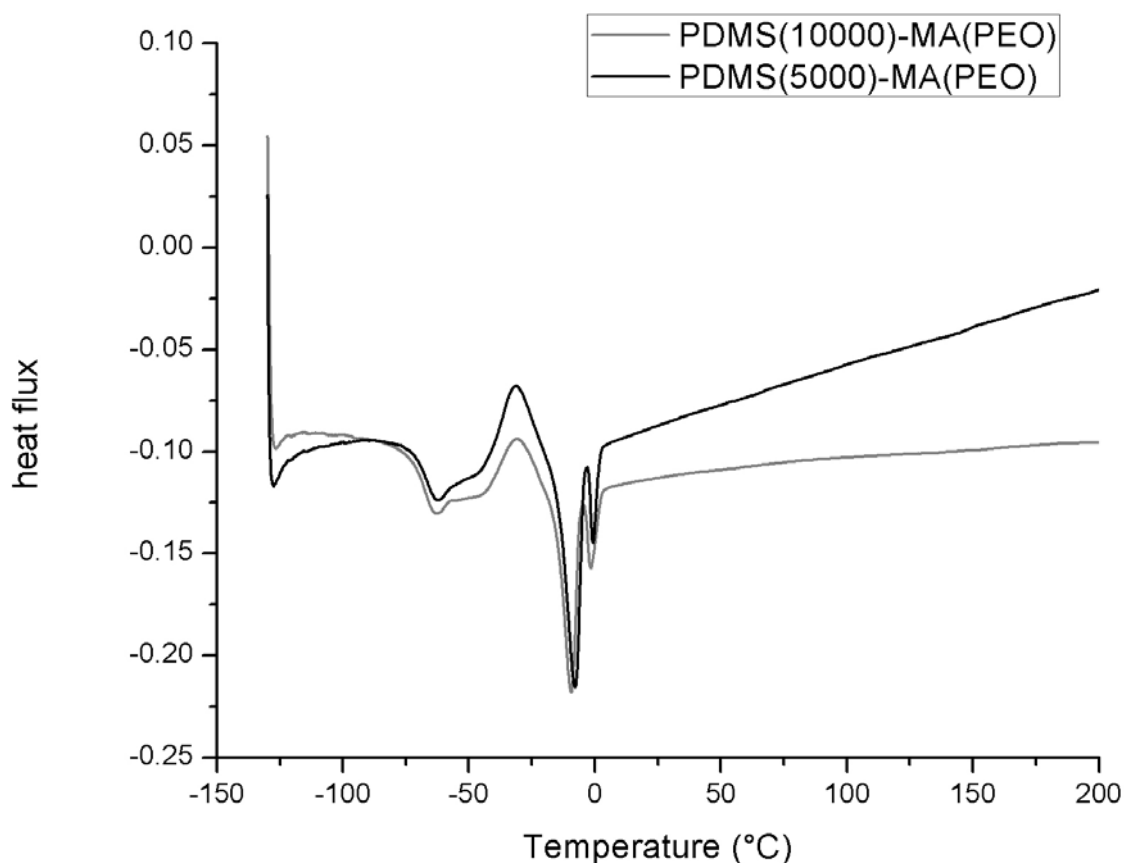

Figure 4.2.2.3. *DSC thermograms of PDMS(10000)-MA(PEO) (grey curve) and PDMS(5000)-MA(PEO)(black curve). T_g of PDMS (-137°C), PEO (-66°C), cold crystallization of PDMS (-30°C) and corresponding melting (-6°C) were observed. The slope observed for the PDMS(5000)-MA(PEO) after melting peak should be related to the instrument.*
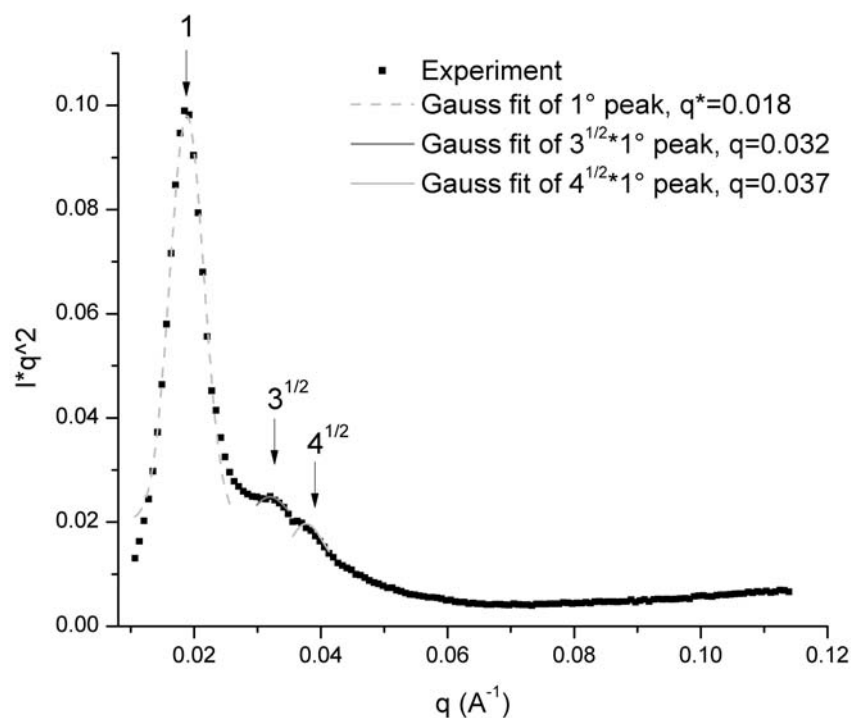
Figure 4.2.2.4. *SAXS of PDMS(5000)-MA(PEO) diblock copolymer with Gauss fits for primary peak and higher order reflections at q values 1:√3:√4 relative to the first-order peak, having the same width as the first order peak.*
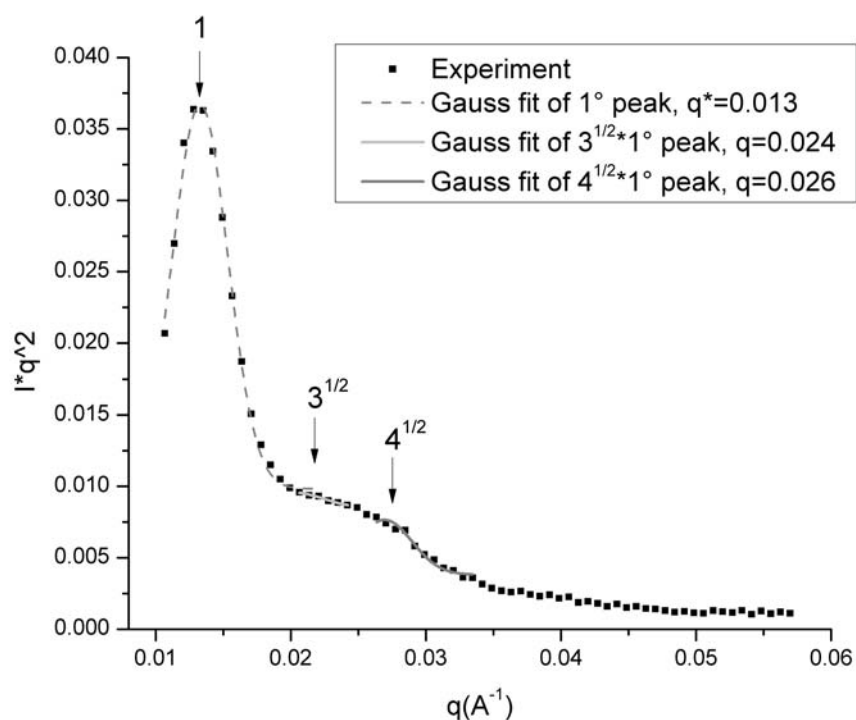

Figure 4.2.2.5. *SAXS of PDMS(10000)-MA(PEO) diblock copolymer with Gauss fits for primary peak and higher order reflections at q values 1:√3:√4 relative to the first-order peak, having the same width as the first order peak.*

The primary peak of PDMS(5000)-MA(PEO) corresponds to ~33 nm center to center distance, and presence of higher order reflections at q values $1:\sqrt{3}:\sqrt{4}$ relative to the first-order peak gives the morphology of the diblock copolymer as hexagonally packed cylinders. And the primary peak of PDMS(10000)-MA(PEO) corresponds to ~47 nm center to center distance, again the presence of higher order reflections at q values $1:\sqrt{3}:\sqrt{4}$ relative to the first-order peak gives the same morphology as hexagonally packed cylinders.

4.3 PEO-MA(PDMS)

PDMS containing block copolymers were synthesized by starting with PDMS macroinitiators in previous sections. Another approach was to convert PEO into an ATRP initiator, and continue with polymerization of poly (dimethylsiloxane) methyl methacrylate [(PDMS)MA] monomer. Synthesis of PEO-MA(PDMS) was accomplished in collaboration with Maria C. Lechmann[96]. Synthesis scheme is illustrated in Scheme 4.3.1.
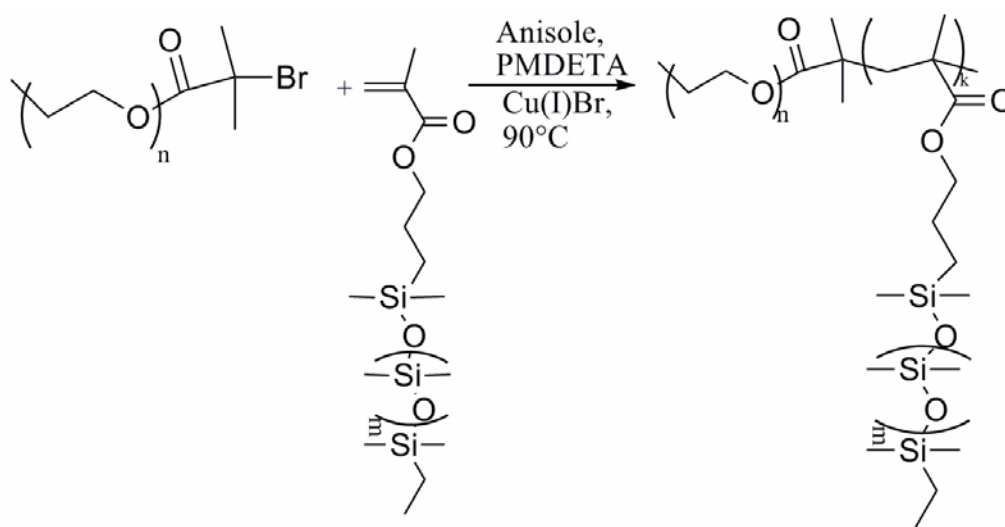
Scheme 4.3.1. *Predicted illustration of PEO-MA(PDMS) synthesis.*

4.3.1 Macroinitiator preparation

PEO-Br macroinitiator was prepared by stopping the anionic polymerization of ethylene oxide by 2-bromo-2-methylpropionyl bromide (ATRP initiator). Ethylene oxide polymerization was initiated by potassium isopropoxide $((CH_3)_2CHOK)$ in THF at room temperature, and left for

shaking overnight. The reaction was stopped by adding the ATRP initiator and then shaked for 1 h. The solvent was evaporated under vacuum. White solid polymer was obtained. The molecular weight of the PEO-Br was 4650 g/mol with a polydispersity of D=1.10.

4.3.2   Polymerization of (PDMS)MA with macroinitiator

In a round bottom flask, 2 g (0.43 mmol)of PEO-Br was dissolved in 15 ml anisole and purged argon through the flask. 1.4 ml (1.34 mmol) (PDMS)MA, 27.5 mg (0.19 mmol) Cu(I)Br and 39.2 µl (0.19 mmol) PMDETA were added into the reaction flask. All reactants were purged with argon prior to addition. Three freeze & thaw cycles applied before heating the flask to 93°C. The reaction was stopped after 3 days. The reaction was stopped by exposure to air, and DOWEX ion exchanger was added. The mixture was filtrated by passing through Al_2O_3, and centrifuged at 4000 rpm for 15 min. Clear solution above Al_2O_3 was taken and solvent was evaporated. The block copolymer was cleaned from the unreacted monomer by ultra filtration using 10k membrane, three times washing with 200 ml THF. In the end obtained diblock copolymer was a few hundred milligrams. ^{1}H-NMR spectrum and molecular weight distribution from GPC of PEO-MA(PDMS) are given in Figure 4.3.2.1 and Figure 4.3.2.1, respectively. PEO-MA(PDMS) has a molecular weight of ~9000 g/mol with a polydispersity of D=2.3. The block copolymer has ~5k-5k molecular weight of each block.
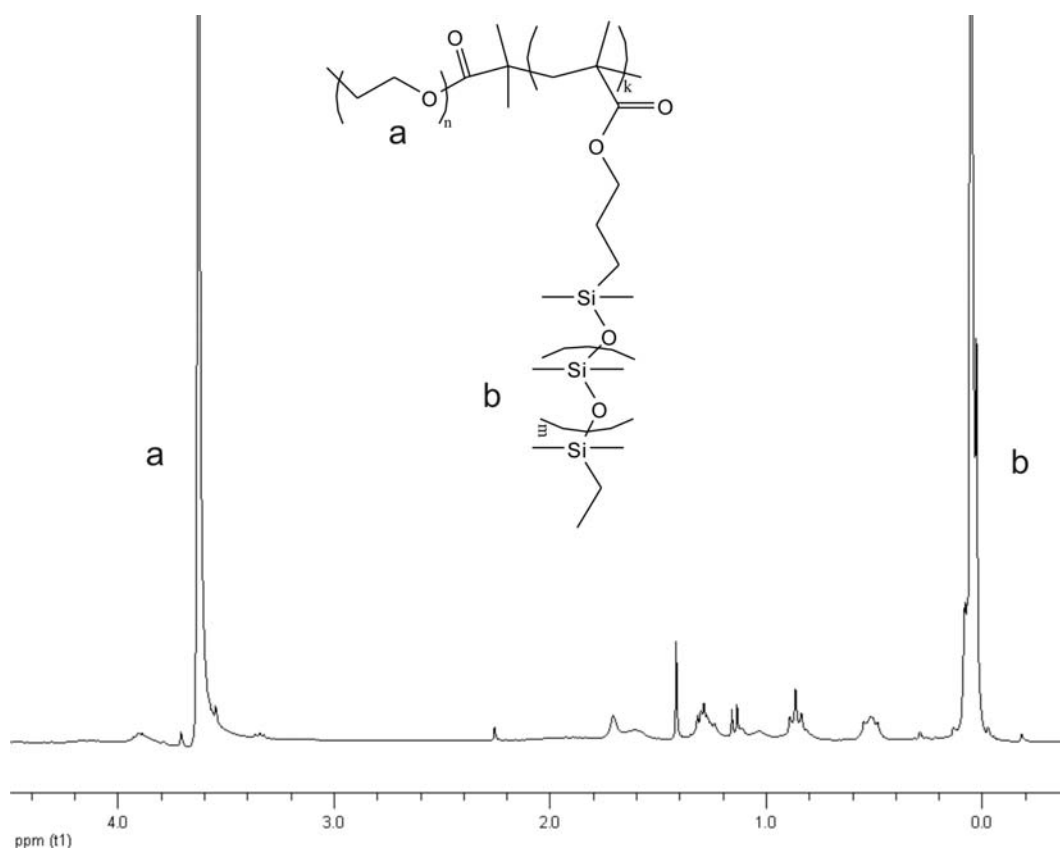
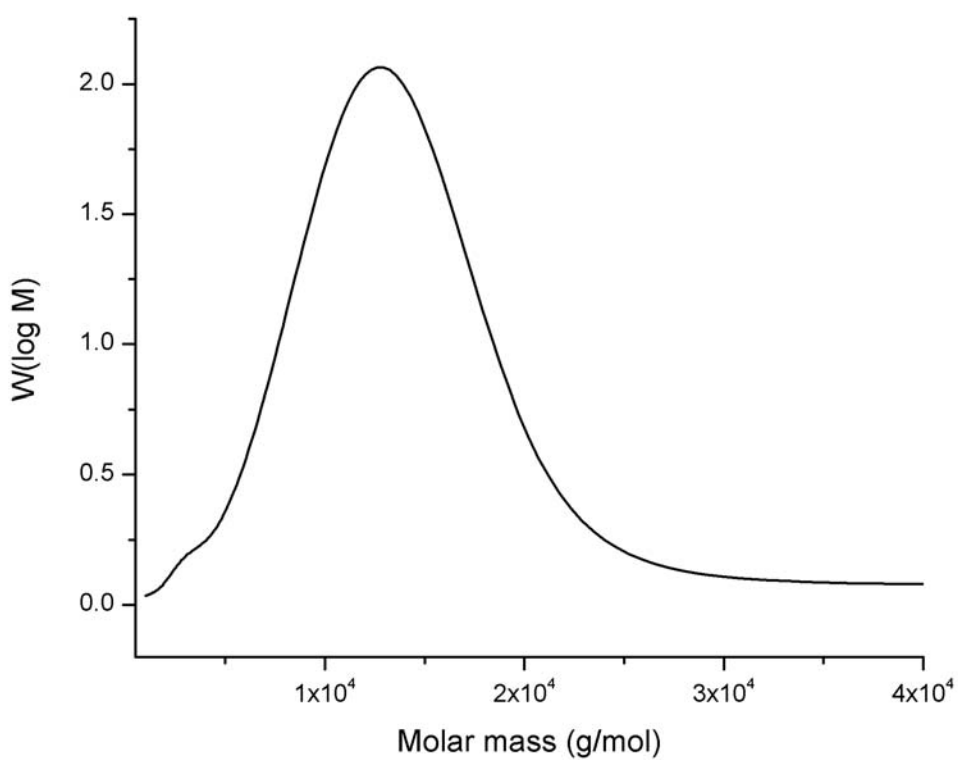***Figure 4.3.2.1.*** *^{1}H-NMR spectrum of PEO-MA(PDMS).*

Figure 4.3.2.2. *Molecular weight distribution of PEO-MA(PDMS) from GPC.*

Morphology of the block copolymer at room temperature could not be determined from SAXS measurement (Figure 4.3.2.3). Primary peak at 0.036 Å^{-1} corresponds to a center to center distance of 17.4 nm, and no higher order peaks exist.
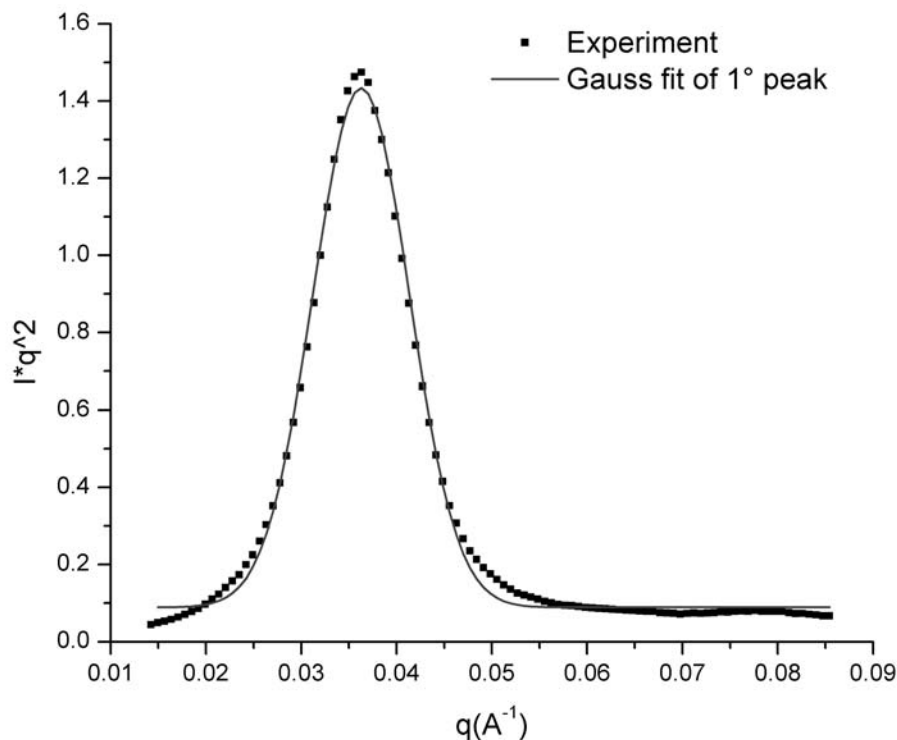

Figure 4.3.2.3. SAXS of PEO-MA(PDMS) diblock copolymer with Gauss fit for primary peak.

T_g of PDMS (-136°) with a slight transition at -61°C for PEO and melting of PEO (50°C) are observed in DSC measurement (Fig.4.3.2.4). The difference of this diblock copolymer from others is the macroinitiator and repeating units. This time macroinitiator is linear PEO and PDMS in the side chain with 10 repeating units. In (PEO)MA-PDMS-MA(PEO) or PDMS-MA(PEO), PDMS is the linear high molecular weight part, thus cold crystallization and corresponding melting could be observed. In the same analogy, in PEO-MA(PDMS), PEO is the linear high molecular weight part and its melting point is observed here, while it was not observed in other blocks since the chains were too short to form crystallites. PDMS here is the short side chain, and its crystallization also is not observed.
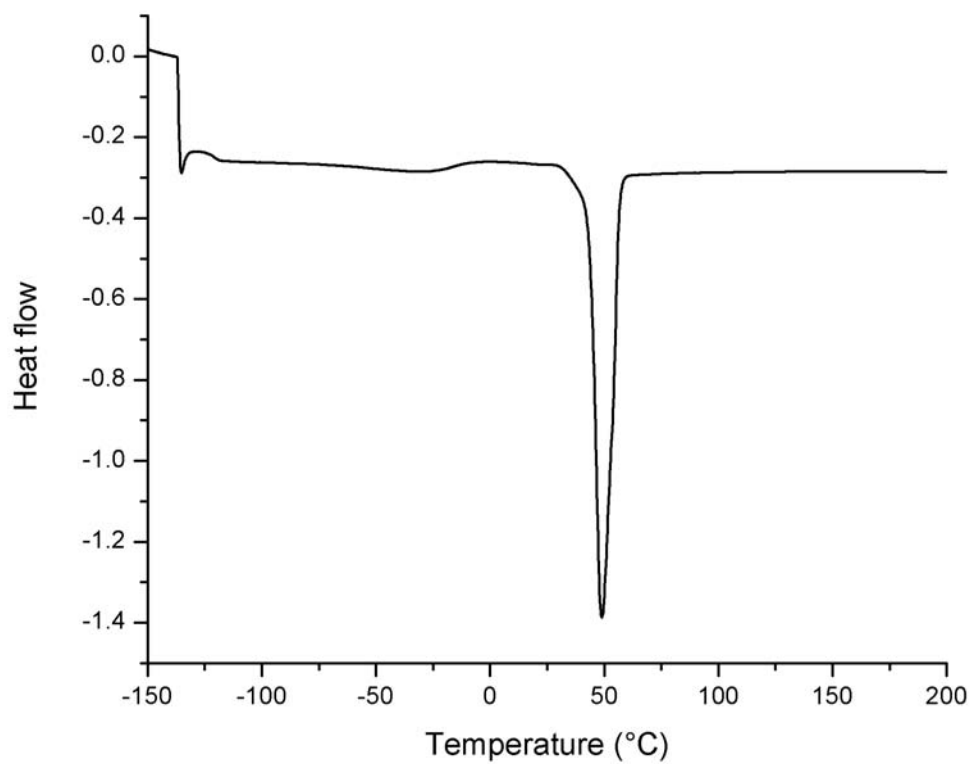
61

Figure 4.3.2.4. *DSC thermogram of PEO-MA(PDMS).*

5 Tinania/PDMS Containing Block Copolymer Nanocomposite Films

An integrated blocking layer composed of conducting titania particles that form charge percolation pathways from their surface to the electrode that they stand on with an insulating matrix among these particles is the aim of the thesis. For this purpose PDMS containing amphiphilic block copolymers were synthesized as explained in Chapter 4. Besides the need for a PDMS containing amphiphilic block copolymer as templating agent via sol-gel chemistry in the nanocomposite film preparation step, cleaning of titania surface from any polymer is required to achieve conduction through the titania nanoparticles. After stirring, the block copolymer and sol-gel solution is spin coated on the substrates. As illustrated in Scheme 5.1 (upper row), if the nanocomposite film is directly heated after preparation, PDMS part of the block copolymer will ceramize even on the titania surface. To clean the titania surface from polymer, plasma etching needs to be applied (Scheme 5.1-lower row).
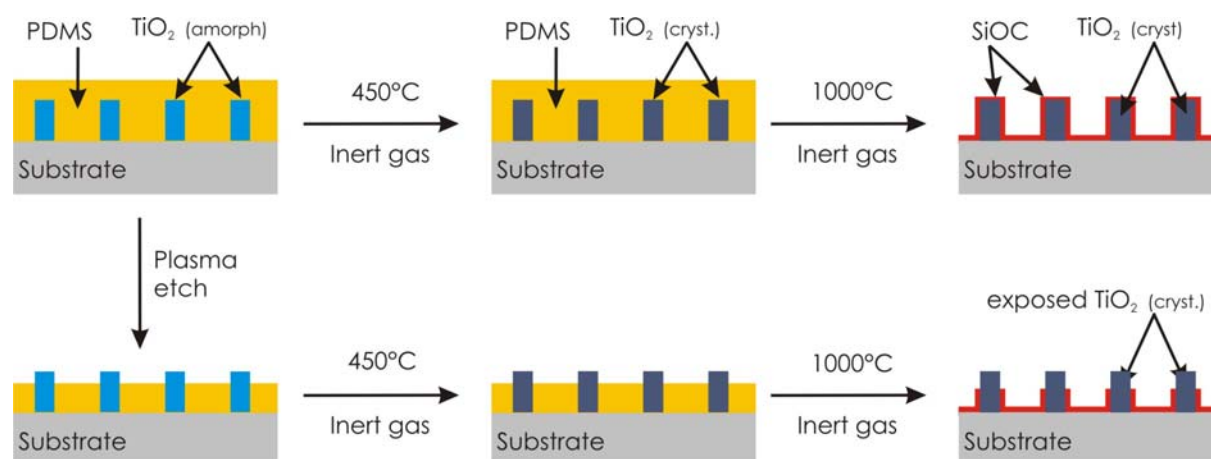
Scheme 5.1. *Illustration of integrated blocking layer preparation steps (drawn not to scale)[97].*

We investigated if PDMS could be etched from the titania surface and its effects on the titania. To do so, titania particles were prepared according to the recipe in our lab by using a poly (styrene)-b-poly (ethylene oxide) (PS-b-PEO) amphiphilic block copolymer as the templating agent[23]. Titania/PS-b-PEO sol-gel was spin-coated on Si wafers (Figure 5.1-1) and then calcined at 450°C under oxygen, burning the templating polymer and turning amorphous titania into anatase polymorph (Figure 5.1-2).

After having titania particles on Si substrates, PDMS homopolymer that was dissolved in THF was spin-coated over them (Figure 5.1-3) and PDMS was etched by oxygen plasma cleaning (Figure 5.1-4). Plasma treatment resulted in crosslinking of PDMS and due to anisotropic shrinkage during crosslinking some cracks occurred throughout the film (Figure 5.2).
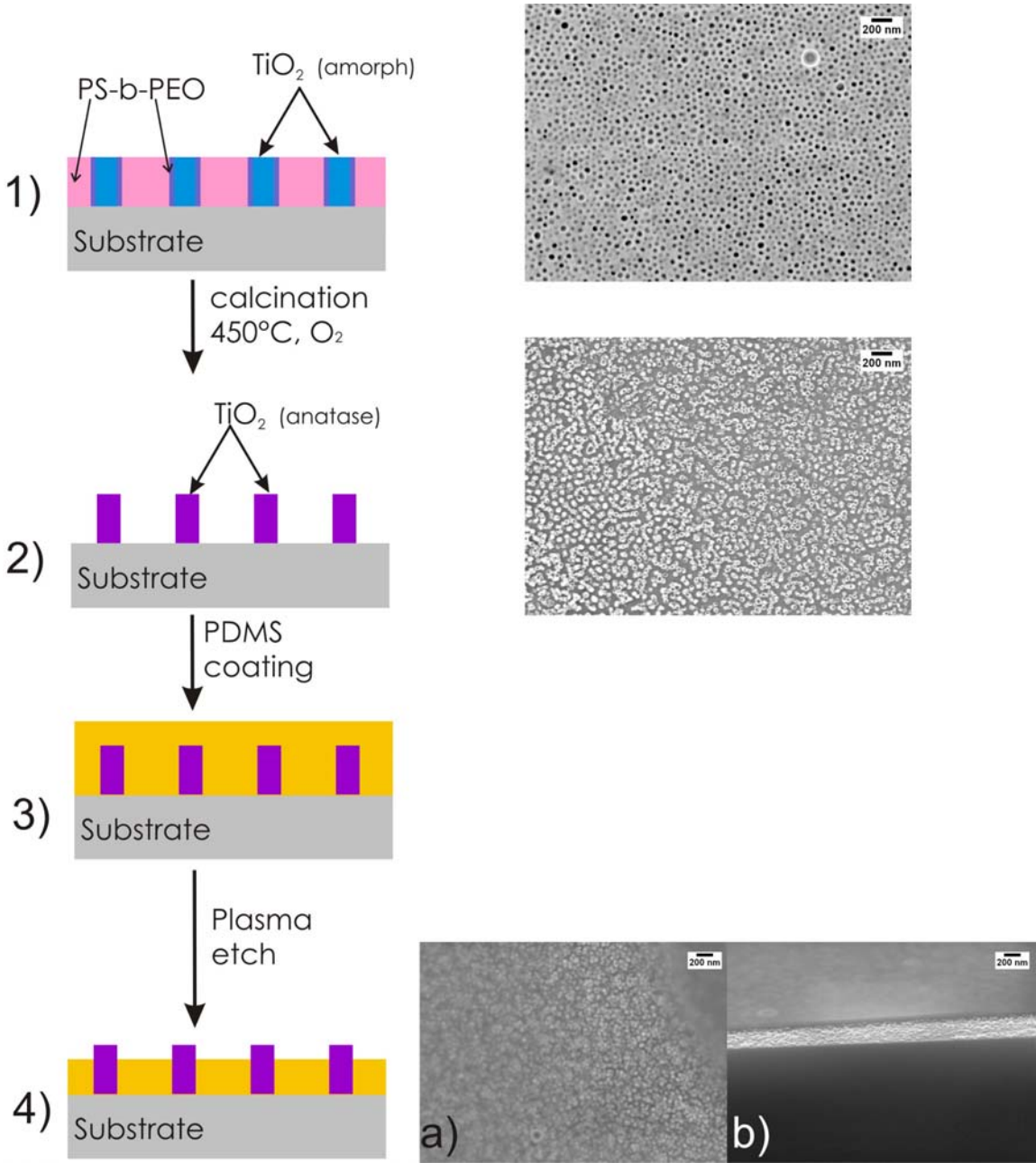

Figure 5.1. *Schematic representation of PDMS coated titania nanoparticles preparation (left) with corresponding SEM images on their right. After titania/PS-b-PEO nanocomposite film preparation on Si-wafer (1), calcination burnt the polymer leaving titania behind (2). Then PDMS homopolymer was spin-coated on these titania particles (3), and titania surface was cleaned from polymer by oxygen plasma (4), with SEM view from top (a) and side view of a crack formed during plasma etching (b).*
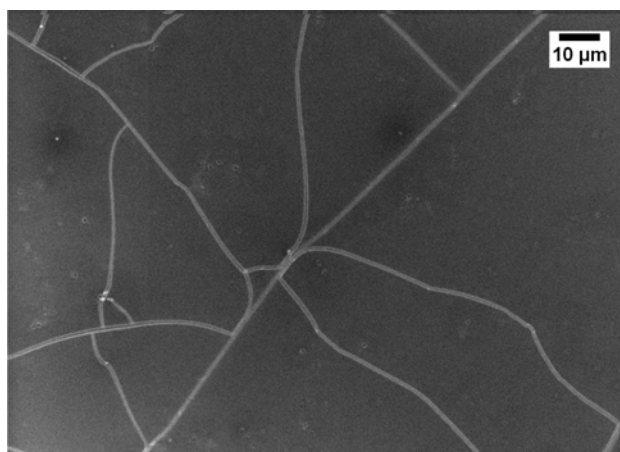
Figure 5.2. *SEM image from top of the cracks occurred after plasma etching on PDMS film.*

The effect of plasma etching time on PDMS film thickness is shown in Figure 5.3; longer plasma treatment etched away more polymer and film thickness decreased. 15 minutes of plasma treatment was enough to see the particles reappear from below the PDMS film (Figure 5.1-4a).
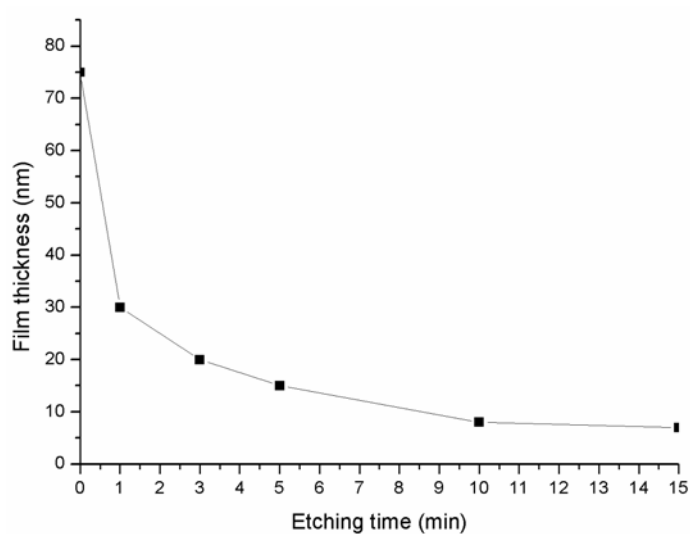
Figure 5.3. *PDMS film thickness versus plasma etching time graph showing the decrease in polymer content with increased plasma cleaning thus resulting in thinner films.*

The crack formation did not change the morphology of the titania nanoparticles since they were already bound to the Si wafer by chemical bonds which were formed between hydroxyl groups on Si wafer surface and titania nanoparticles during spin-coating and fixed upon heat

65

treatment. The covalent fixation of the nanoparticles over large surface areas was further investigated by μGISAXS measurements. The 2D scattering image in Figure 5.4-a corresponds to the scattering from as prepared titania/PS-b-PEO nanocomposite films (Figure 5.1-1). Figure 5.4-b shows the scattering from uncovered titania particles after calcination (Figure 5.1-2). The scattering from PDMS coating removal by 3 min 45 s plasma and 15 min plasma treatment are shown in Figure 5.4-c,d respectively. To qualitatively analyze the scattering images, horizontal cuts at the critical angle of TiO_2 are shown in Figure 5.4-e. Each cut corresponds to an individual sample of the same morphology. The structure peak marked by the solid line in each sample remains at the same q_y position. This indicates that the ordering of the titania particles does not change upon PDMS coating and its removal by different plasma exposure times. In two dimensional x-ray scattering patterns, the peaks on either side of the Yoneda peak corresponding to titania particles become more pronounced after calcination (Figure 5.4-b) since the difference in scattering length density increases. Further coverage by a PDMS coating decreases the difference in scattering length leading to decreased peak intensity. However, cleaning PDMS over the titania nanoparticles again increases the intensity of the peak. Although the intensity of the peak changed before and after PDMS coating, the morphology of the titania nanoparticles did not change which is obvious from the constant structure peak position.

The effect of PDMS coating and its subsequent removal on the photophysical properties of titania nanoparticles were investigated by measuring their photoluminescence (PL). PL spectroscopy depends on electronic excitations and gives information about the electro-optic and photoelectric properties of materials. The PL spectra of bare titania particles, PDMS coated titania particles and plasma cleaned PDMS coated particles are shown in Figure 5.5. The spectra indicate totally different surface photophysical properties after plasma etching of PDMS coating. Bare and PDMS coated titania nanoparticles do not show any considerable peak indicating any photo activity upon illumination. These particles reappeared below from the PDMS film, and there is considerable increase in the intensity of the peak which can be assigned to self-trapped excitons localized on TiO_6 octahedra (peaks at 398nm and 470 nm) and surface defects (peak at 431 nm)[27]. Since both types of exciton traps appear after plasma treatment, it is reasonable to conclude that both of them are present in the surface near regions of the nanoparticles layer.
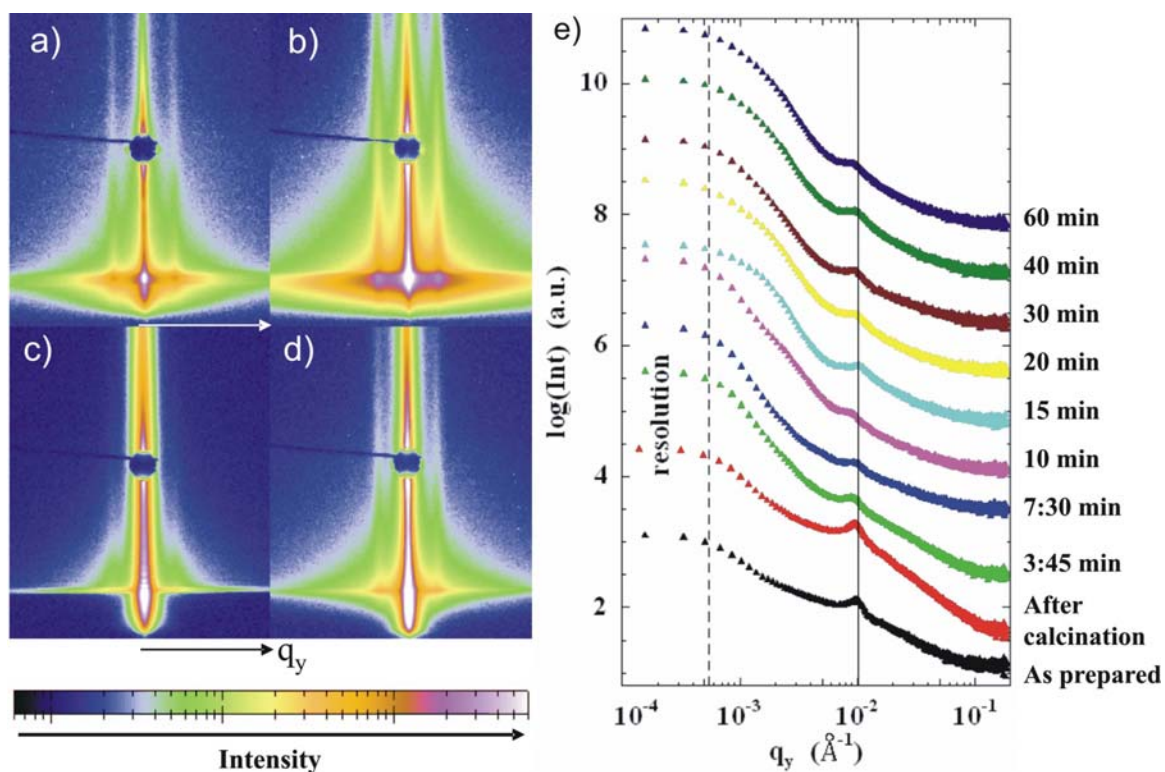
Figure 5.4. *Typical two-dimensional µGISAXS scattering patterns are shown in (a-d) corresponding to block copolymer-titania nanocomposite films in (a), bare TiO₂ nanoparticles in (b), TiO₂ nanoparticles+PDMS after 3min 45 sec plasma etching in (c), and TiO₂ nanoparticles+PDMS after 15 min plasma etching in (d). The intensity is shown on a logarithmic scale (blue = low and purple/white = high intensity).Horizontal cuts at the critical angle of TiO₂ shown in (e), display the logarithm of intensity versus horizontal momentum transfer q_y in log-scale for the samples from bottom to top as in (a-d) and continuing with increasing etching times. Each cut corresponds to an individual sample. The vertical line marks a position of a well defined lateral structure. The dashed line indicates the resolution limit. All curves are shifted along the y-axis for clarity.*
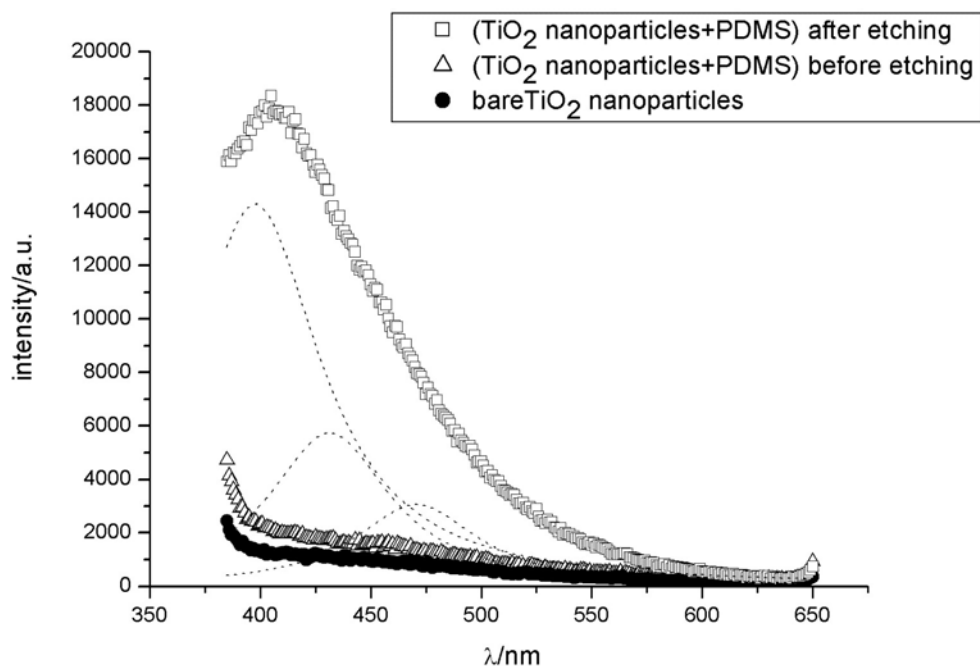
Figure 5.5. *PL spectra of bare, PDMS coated and PDMS coating plasma cleaned TiO₂ nanoparticles[97].*

Plasma treatment step is crucial to prevent complete insulation of the titania surface. As presented above plasma cleaning resulted in desired cleaning of titania surface from PDMS. However the crack formation is observed in PDMS homopolymer films upon plasma treatment.

Titania nanoparticles and PDMS coating were combined in particle preparation step via the synthesized PDMS containing amphiphilic block copolymers. Titania nanoparticles were prepared using these amphiphilic block copolymers as templating agents via sol-gel chemistry. The sol-gel solution was spin coated on pre-cleaned Si wafers, and the titania/block copolymer nanocomposite films were formed. Titania nanoparticles' surface was uncovered from any polymer prior to annealing. Contrary to the PDMS homopolymer coating and subsequent plasma etching, no cracks on the nanocomposite film were observed after plasma treatment and further heating (Figure 5.6). In titania/(PEO)MA-PDMS-MA(PEO) nanocomposite films crosslinking of PDMS occurred via the titania nanoparticles. The stress caused by the crosslinking in the film was absorbed before resulting in any deformation through the film. Thus, uniform nanocomposite films were obtained.
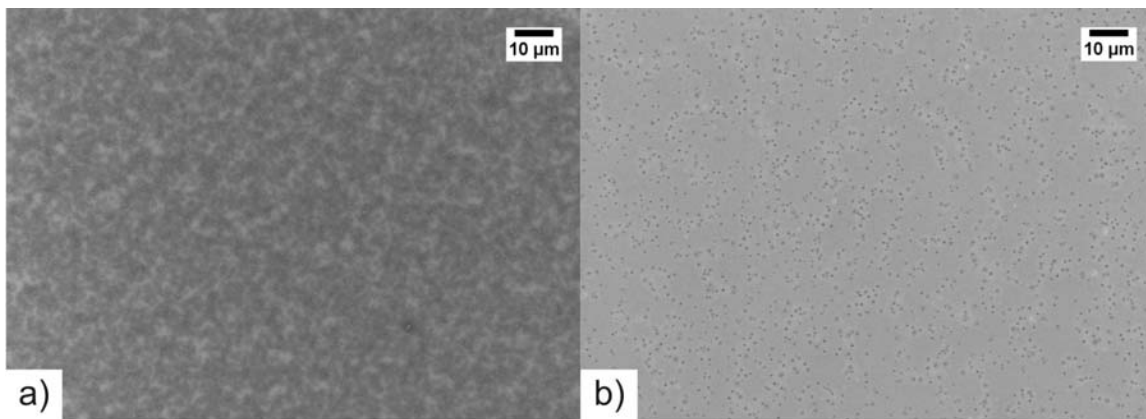
Figure 5.6. *SEM image of titania/(PEO)MA-PDMS-MA(PEO) nanocomposite films after plasma treatment (a) and plasma treatment/annealing at 450°C.*

Scheme 5.2 shows the treatment applied to the nanocomposite films after they are spin-coated on substrates. Plasma treatment was followed by heating to 450°C, 600°C and 1000°C under nitrogen to observe the effect of the heating temperature on titania nanoparticles and polymeric derived ceramic. Detailed explanation of the titania nanocomposite film preparation and characterization is given in the following sections.
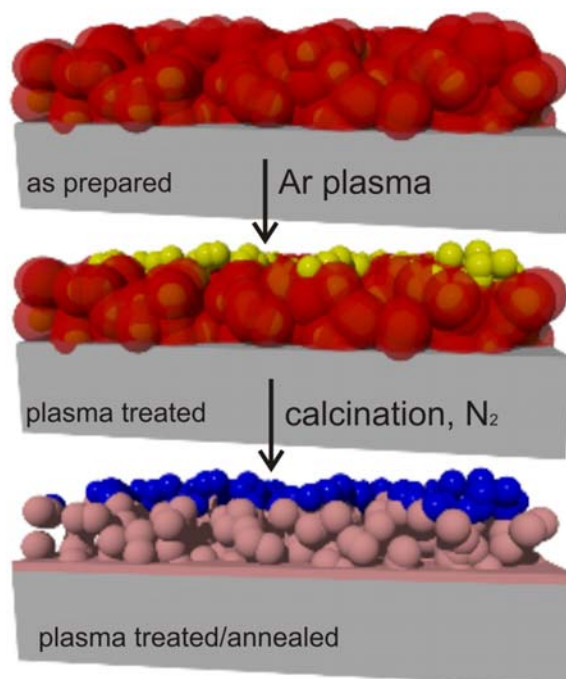
Scheme 5.2. *Schematic representation of the treatment applied to the nanocomposite films (not drawn to scale). Plasma etching uncovers the titania surface from polymer, and annealing under N$_2$ results in polymer derived ceramic SiOC with anatase titania[98].*

5.1 Preparation

5.1.1 (PEO)MA-PDMS-MA(PEO)/Titania Nanocomposite Films

Sample solutions were prepared by dissolving 40.5 mg of (PEO)MA-PDMS-MA(PEO) block copolymer in 3004 mg THF and 1008 mg isopropanol. 45 mg TTIP and 47 mg HCl were added and stirred for 1 hour at ambient temperature. These amounts were for 1% HCl, 1% TTIP and 1% block copolymer by weight over the total components. The amount of HCl was varied to 3% and 5% of the total amount. In a typical experiment, component amounts were 43.8 mg of (PEO)MA-PDMS-MA(PEO) block copolymer, 3007 mg THF, 1004 mg isopropanol, 43.8 mg TTIP, 84.6 mg HCl for 3% HCl and 42.4 mg of (PEO)MA-PDMS-MA(PEO) block copolymer, 3006 mg THF, 1002 mg isopropanol, 45.5 mg TTIP, 140.7 mg HCl for 5% HCl. Block copolymer amount was also varied to 2% by weight; 92.6 mg of (PEO)MA-PDMS-MA(PEO) block copolymer, 3021 mg THF, 1013 mg isopropanol, 42.2 mg TTIP, 43.8 mg HCl. Titania precursor amount was varied to 2% by weight; 40.2 mg of (PEO)MA-PDMS-MA(PEO) block copolymer, 3016 mg THF, 1017 mg isopropanol, 82.6 mg TTIP, 40 mg HCl.

The formation of micellar structures in the sol-gel was investigated by dynamic light scattering (Figure 5.1.1-a,b). Sample solution was prepared as the same as 1%HCl composition. After stirring for one hour, DLS measurements were performed between 30°-150° scattering angles at room temperature. The correlation function exhibits a two step decay shape. The inset of Figure 5.1.1-b shows the diffusive rate Γ as a function of scattering vector q. Both processes exhibit a slope of 2 following the diffusive rate of $\Gamma=Dq^2$. The fast process of q-independent intensity is assigned to the diffusion of a single titania precursor with a hydrodynamic size of 2.3 nm. The appearance of the second process is due to the favorable titania precursor-PEO interactions leading to the formation of micellar structures with a hydrodynamic radius of 110 nm. As expected from the size, the time average intensity $I(q)$ was found to be q-dependent (Figure 5.1.1-b). However more information about the micellar structures could not be obtained since the form factor is needed. Moreover to examine the colloidal stability, DLS measurements were performed for the same system 24 hours after the preparation, and exactly the same behavior was observed.
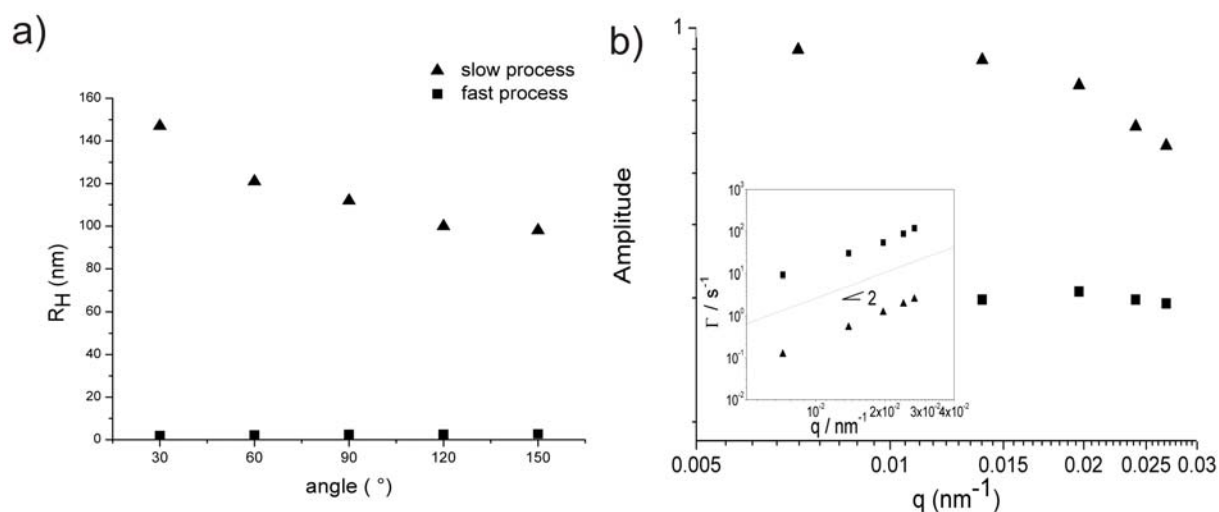
Figure 5.1.1. Hydrodynamic radius of aggregates in 1%HCl composition measured at different angles by DLS (a) and corresponding relative amplitude versus q plot (b).

Nanocomposite films were prepared on Si(100) substrates by spin coating for 60 s using a Süss MicroTec Delta 80 spin coater under ambient conditions (temperature, 21°C; relative humidity, 35-45%; rotation speed of 2000 rpm; acceleration speed of 2000 rpm/s). Si wafers were cleaned prior to spin-coating by heating to 80°C in the hydrogen peroxide-ammonium-water mixture for 15 min, followed by dilution with Millipore water, 15 min ultrasonication in hydrochloric acid-water mixture method and dilution with Millipore water.

To uncover the surface of the titania particles argon plasma treatment was applied by TECHNICS Plasma-Processor 200-6 at 300 Watt for 10 min. Plasma etched titania nanocomposite films were heated up to 450°C, 600°C and 1000°C separately under nitrogen atmosphere with a heating rate of 6.25°C/min starting from room temperature and kept at these temperatures for 4 h. After calcination the samples were cooled to room temperature in the furnace.

The annealing step is required for titania/amphiphilic block copolymer nanocomposite films to convert initially amorphous titania into crystalline anatase polymorph and decompose the templating block copolymer[23]. In prepared nanocomposite films conversion of PDMS to a ceramic material is also desired. The effect of temperature on (PEO)MA-PDMS-MA(PEO) and a high molecular weight PDMS (22k) was investigated by TGA with a heating rate of 1°K/min under nitrogen (Figure 5.1.1.1). PDMS homopolymer started to decompose at 290°C and was 1.6% by weight at 360°C and 1.6% at 1000°C. (PEO)MA-PDMS-MA(PEO) started

decomposing around 150°C but at a rate much slower that that of the homopolymer. The triblock copolymer was 46% by weight at 360°C, 3% at 560°C and at 1000°C. Titania needs to be heated at 450°C for 4 hours to completely be in anatase polymorph. TGA measurement of (PEO)MA-PDMS-MA(PEO) with same the same heat treatment (6.25°K/min to 450°C, and keeping at his temperature for 4h) applied to nanocomposite films showed 4.9% of polymer derived ceramic (SiOC) at the end of the treatment (Figure 5.1.1.2).
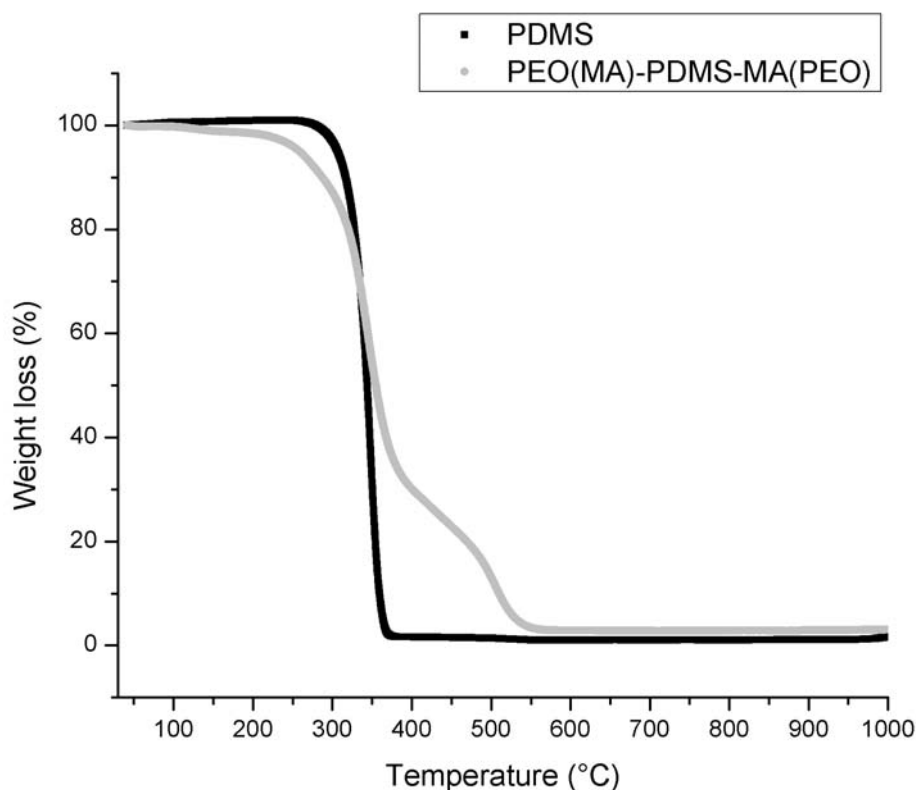
Figure 5.1.1.1. *TGA thermograms of PDMS and (PEO)MA-PDMA-MA(PEO).*
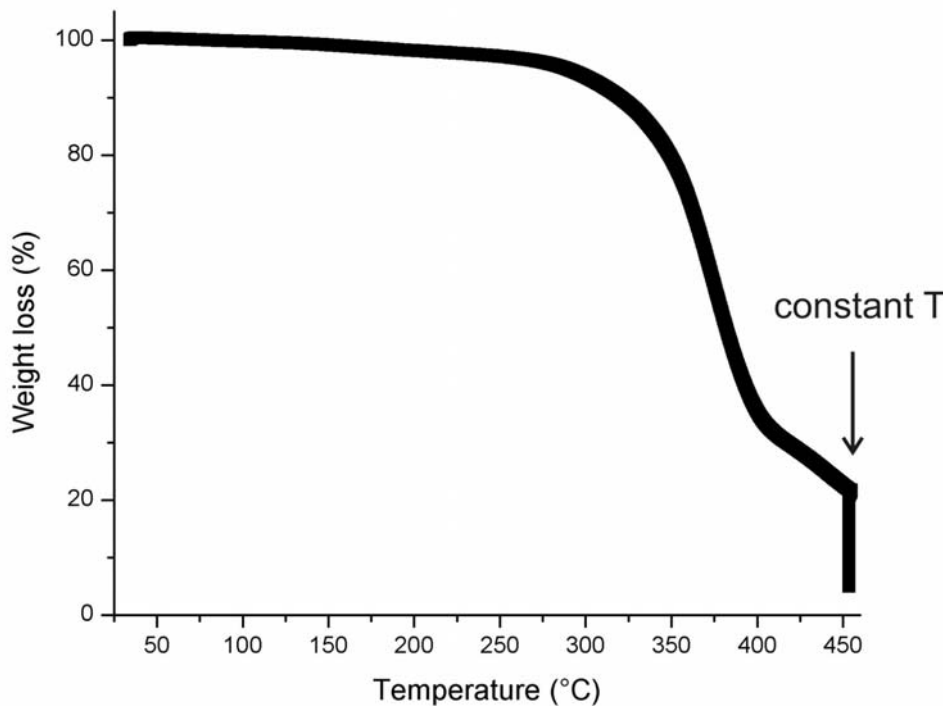
Figure 5.1.1.2. *TGA thermogram of (PEO)MA-PDMA-MA(PEO) with heating rate of 6.25°/min and keeping at 450°C for 4h.*

Heat treatment that is applied to nanocomposite films is enough to convert almost all of (PEO)MA-PDMS-MA(PEO) into a SiOC type ceramic material. The photograph of only (PEO)MA-PDMS-MA(PEO) after heating with the same procedure as applied to the nanocomposite films is shown in Figure 5.1.1.3. The white color of the residue indicates negligibly small amount of carbon.

Figure 5.1.1.3. *Photograph of (PEO)MA-PDMS-MA(PEO) block copolymer derived ceramic, SiOC, on a Si wafer after annealing at 450°C under nitrogen, shows white color of the residue.*

5.1.2 PDMS-MA(PEO)/Titania Nanocomposite Films

Different molecular weight PDMS-MA(PEO) block copolymers were used as the templating agents. Sample solutions for PDMS(5000)-MA(PEO) were prepared by dissolving 44 mg of block copolymer in 3043 mg THF and 1019 mg isopropanol. 40 mg TTIP and 43 mg HCl were added and stirred for 1 hour at ambient temperature. Samp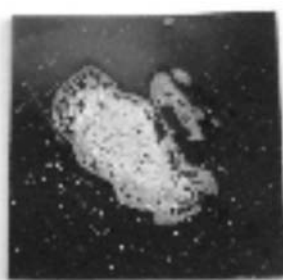le solutions for PDMS(10000)-MA(PEO) were prepared by dissolving 44 mg of block copolymer in 3049 mg THF and 1038 mg isopropanol. 43 mg TTIP and 49 mg HCl were added and stirred for 1 hour at ambient temperature. These amounts were for 1% HCl, 1% TTIP and 1% block copolymer by weight over the total components.

Nanocomposite films were prepared on Si(100) substrates by spin coating for 60 s using a Süss MicroTec Delta 80 spin coater under same conditions as on 5.1.1. 10 min of Argon plasma treatment at 300 Watt was followed by the heating step up to 450°C, 600°C and 1000°C separately under nitrogen atmosphere with a heating rate of 6.25°C/min starting from room temperature and kept at these temperatures for 4 h. After calcination the samples were cooled to room temperature in the furnace.

5.1.3 PEO-MA(PDMS)/Titania Nanocomposite Films

Sample solution for was prepared by dissolving 41 mg of PEO-MA(PDMS) block copolymer in 3051 mg THF and 1026 mg isopropanol. 72.8 mg TTIP and 65 mg HCl were added and stirred for 1 hour at ambient temperature. These amounts were for 1% HCl, 1% TTIP and 1% block copolymer by weight over the total components.

Nanocomposite films were prepared on Si(100) substrates by the same conditions as in 5.1.1. Oxygen plasma treatment was applied by TECHNICS Plasma-Processor 200-6 at 300 Watt for 10 min. Plasma etched titania nanocomposite films were heated up to 450°C, 600°C and 1000°C separately under nitrogen atmosphere with a heating rate of 6.25°C/min starting from room temperature and kept at these temperatures for 4 h. After calcination the samples were cooled to room temperature in the furnace.

5.2 Characterization

5.2.1 (PEO)MA-PDMS-MA(PEO)/Titania Nanocomposite Films

The morphology and topography of the nanocomposite films were investigated by SEM and SFM. Figure 5.2.1.1 shows the SFM height images on (a) and SEM images on (b), for (1) as prepared, (2) plasma treated, (3) plasma treated/annealed at 450°C, (4) plasma treated/annealed at 600°C, and (5) plasma treated/annealed at 1000°C for 1%HCl series. All scale bars correspond to a length of 1μm. The color scale correspondence of height images and scale in phase images for all sample series are given in Table 5.2.1.1.

Integrated blocking layer for solar cell applications require plasma treatment and annealing at 450°C. The effect of temperature on the morphology of the titania particles was investigated by heating the nanocomposite films further to 600°C and 1000°C. As a reference a pristine sample (film thickness 47±4 nm) was imaged without any treatment prior to the measurement (Figure 5.2.1.1-a1). Without plasma treatment the free film surface has a big height contrast. 10 min of plasma treatment resulted in a characteristic surface morphology consisting of circular pits (Figure 5.2.1.1-b1, film thickness 28±3 nm) which are the result of a liquid/liquid phase separation during spin coating[99]. The color contrast in as prepared and plasma treated samples show the height difference on the surface. X-ray reflectivity measurement of these samples did not show any noticeable Kiessig fringes due to the high surface roughness. Heat treatment reduces surface roughness; thus height difference in SFM images decreases (Figure 5.2.1.1-c1-e1), however the pits remain present at the surface. Corresponding x-ray reflectivity curves showed Kiessig fringes enabling thickness calculation of the films after heating by the difference of two maxima using Eqn.3.2.9.10 (Figure 5.2.1.2), giving 18±1 nm after 450°C, 19±1 nm after 600°C, and 3±0.5 nm after 1000°C heat treatments. Also the film thicknesses were fitted using a parrat formalism (Parratt32, HMI)[100].The integrated blocking layer is composed of titania and polymer derived SiOC. From the fit, the thickness of the plasma treated/annealed at 450°C layer can be seen as 18.5 nm. All values for the film thicknesses are given above with error bar representing the difference between the value obtained from the modeling and the value calculated by using the difference of the two q_{max}. However since the layers are not composed of a single material and the titania nanoparticles have a porous structure, the modeling of the experiment is not used to yield more insight on the roughness and scattering length density of the film.

Sample name	Height image	Phase image
1%HCl-as prepared	30.0 nm	3.0 °
1%HCl-plasma	25.0 nm	15.0 °
1%HCl-plasma+450°C	10.0 nm	8.0 °
1%HCl-plasma+600°C	10.0 nm	5.0 °
1%HCl-plasma+1000°C	12.0 nm	15.0 °
3%HCl-as prepared	50.0 nm	8.0 °
3%HCl-plasma	35.0 nm	15.0 °
3%HCl-plasma+450°C	10.0 nm	3.0 °
3%HCl-plasma+600°C	20.0 nm	10.0 °
3%HCl-plasma+1000°C	20.0 nm	35.0 °
5%HCl-as prepared	40.0 nm	7.0 °
5%HCl-plasma	30.0 nm	2.0 °
5%HCl-plasma+450°C	20.0 nm	5.0 °
5%HCl-plasma+600°C	10.0 nm	5.0 °
5%HCl-plasma+1000°C	15.0 nm	35.0 °
2%polymer-as prepared	50.0 nm	20.0 °
2%polymer-plasma	20.0 nm	3.0 °
2%polymer-plasma+450°C	35.0 nm	10.0 °
2%polymer-plasma+600°C	20.0 nm	30.0 °
2%polymer-plasma+1000°C	20.0 nm	30.0 °
2%TTIP-as prepared	60.0 nm	40.0 °
2%TTIP-plasma	30.0 nm	10.0 °
2%TTIP-plasma+450°C	35.0 nm	5.0 °
2%TTIP-plasma+600°C	25.0 nm	3.0 °
2%TTIP-plasma+1000°C	35.0 nm	15.0 °

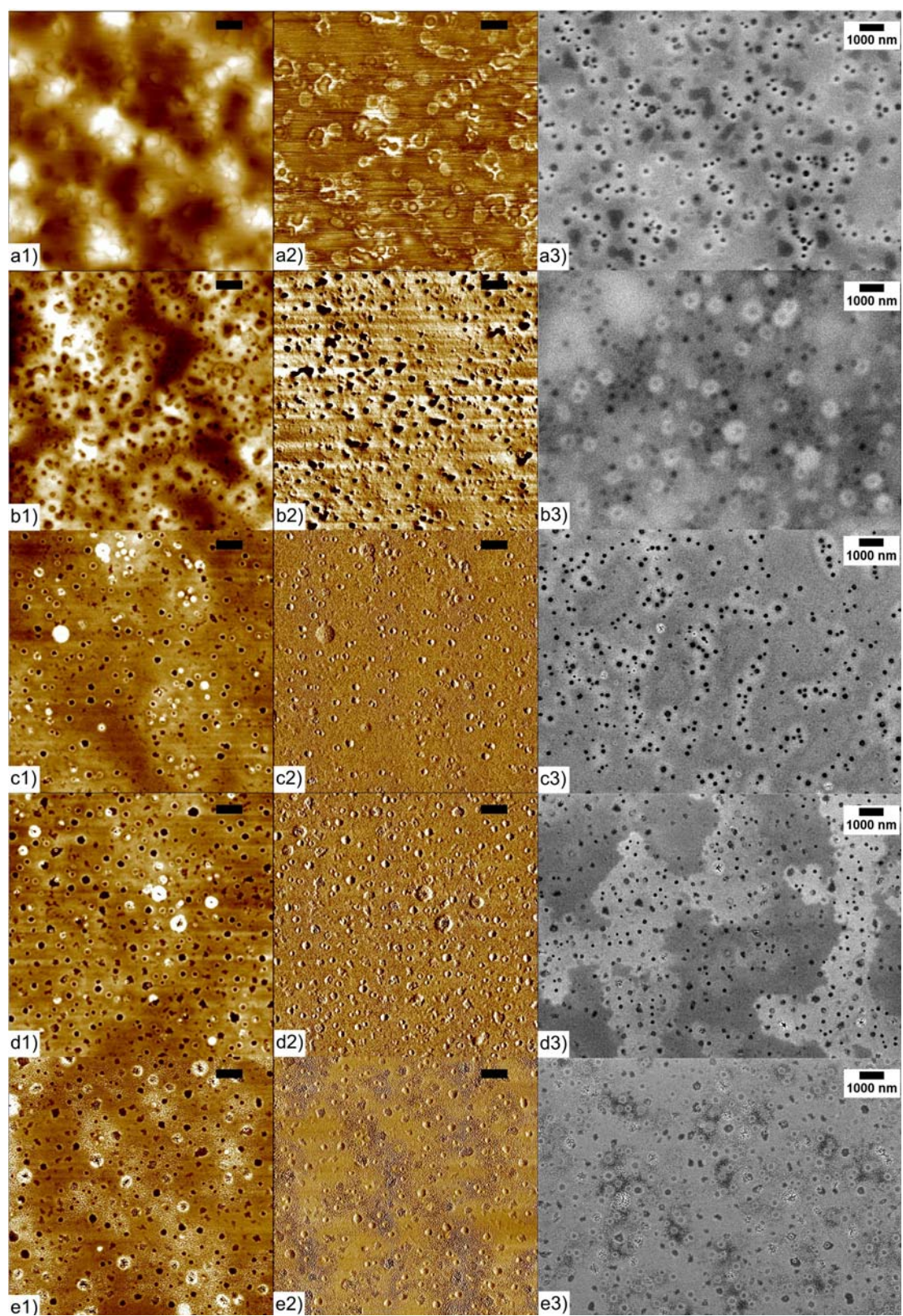***Table 5.2.1.1.*** *Color scale correspondence in height and phase images for all samples.*

Figure 5.2.1.1. *SFM height images on (1), phase on (2) and SEM images on (3) for (a) as prepared, (b) plasma treated, (c) plasma treated/heated to 450°C, (d) plasma treated/heated to 600°C, and (e) plasma treated/heated to1000°C of 1%HCl series.*
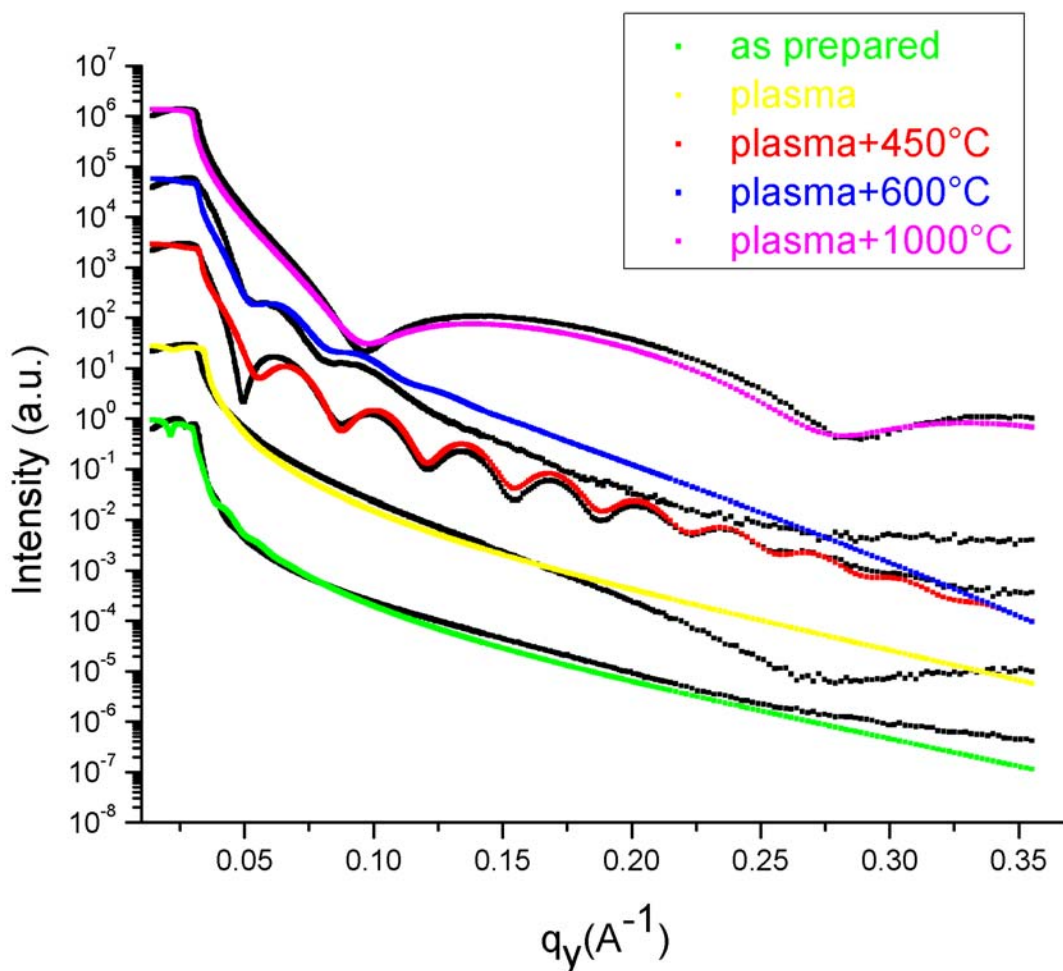
77

Figure 5.2.1.2. *X-ray reflectivity curves (black) with their fits from Parratt for as prepared (green), plasma treated (yellow), plasma treated/annealed at 450°C (red), plasma treated/annealed at 600°C (blue), plasma treated/annealed at 1000°C (pink) samples.*

The contrast between titania and the surrounding polymer layer which was enhanced by the Image J software in SEM images in pristine and plasma treated samples results from surface roughness of the films (Figure 5.2.1.1-a3-b3). After heating, decreased polymer content in the interaction volume of the electron beam enabled generated secondary electrons to escape from the surface easily. Thus sharper images with SEM could be obtained (Figure 5.2.1.3-b), especially in the sample heated to 1000°C, with the thinnest polymeric derived ceramic film. Within the surface depressions that are formed during spin-coating due to liquid-liquid miscibility gap, smaller titania particles are again present as observed by SFM and SEM (Figure 5.2.1.3).
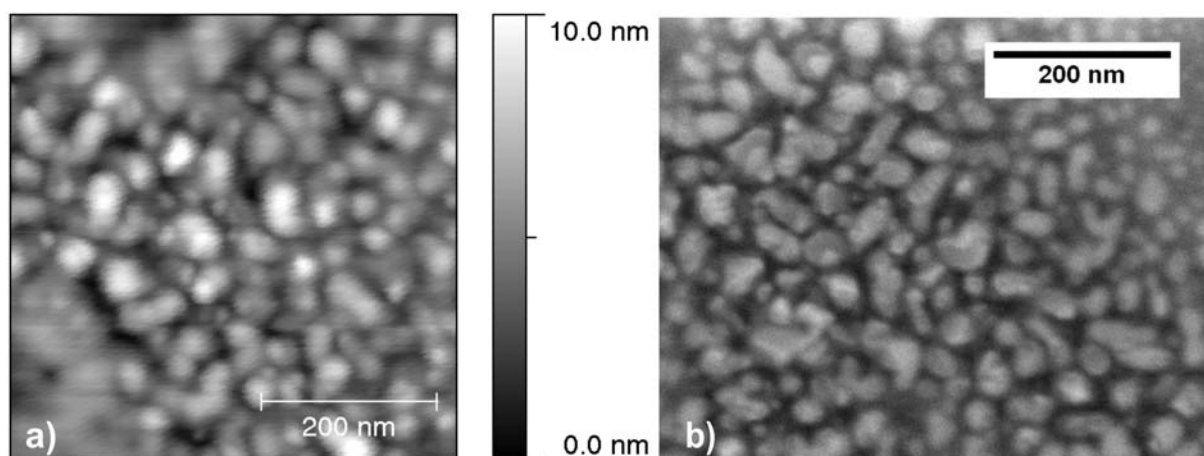
Figure 5.2.1.3. SFM height (a) and SEM (b) images of plasma treated/annealed at 1000°C sample showing the presence of titania in the circular pits present on the nanocomposite film.

The electronic behavior of the integrated blocking layer, titania/(PEO)MA-PDMS-MA(PEO) nanocomposite films, was investigated by conducting probe SFM and scanning Kelvin probe microscopy. SKPM is a derivative of scanning force microscopy. It measures the contact potential difference between the surfaces of two materials with nanometer range resolution[101]. A comparative study by SFM and SKPM was performed for as prepared and plasma treated/annealed at 450°C samples as shown in Figure 5.2.1.4. Thirty seconds of argon plasma was applied prior to the measurement of as prepared samples to prevent contamination of the tip and enable imaging of titania domains in the unheated areas. The topography of the as prepared sample (Fig.5.2.1.4-1a; roughness on $(500\,nm)^2$ RMS = 0.6 nm) remained unchanged after annealing (Fig.5.2.1.4-2a; roughness on $(500\,nm)^2$ RMS = 0.6 nm). Even 30 seconds of plasma treatment took away most of the polymer for these measurements resulting in the same surface roughness after heating. The phase contrast in SFM imaging sometimes allows distinguishing different material behavior[102]. While conventional SFM experiments show no change in phase contrast between the as prepared and plasma treated/annealed samples (Fig.5.2.1.4-1b and 2b), SKPM revealed a property change upon plasma treatment/annealing, the absolute value of the sample work function was shifted from 4.0±0.1 eV to 4.6±0.1 eV, respectively (Fig.5.2.1.4-1c and 2c). In all as prepared samples, the work function changed during scanning, i.e. from top to bottom in this case (Fig.5.2.1.4-1c). This decrease in work function can be attributed to the gradual contamination of the SFM-tip by the soft (PEO)MA-PDMS-MA(PEO) during scanning[62]. Such a pronounced decrease in surface potential was not observed in plasma treated/annealed samples, which additionally
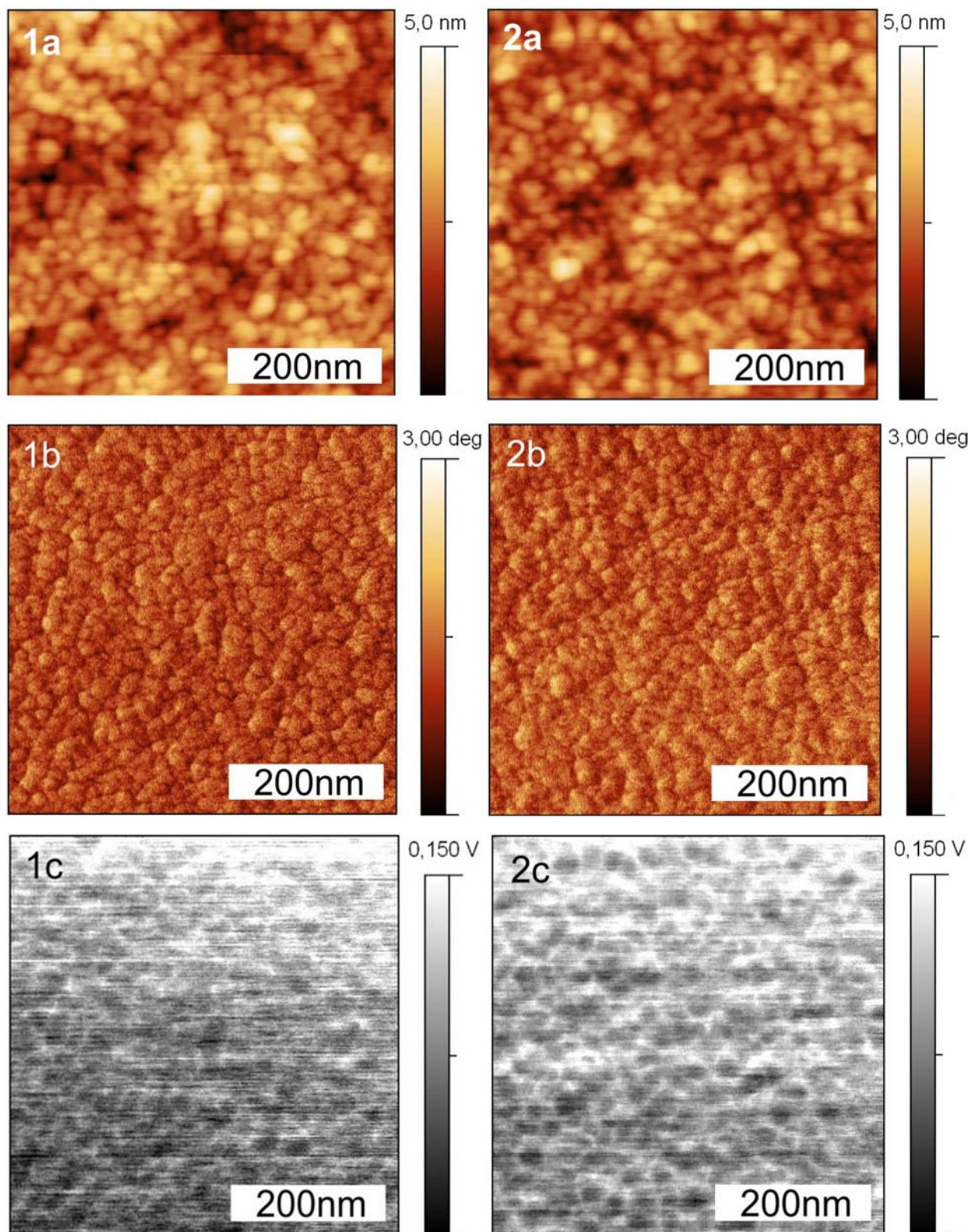
Figure 5.2.1.4. *Comparison of samples as prepared (1) and plasma treated/annealed at 450°C (2) titania/(PEO)MA-PDMS-MA(PEO) nanocomposite films, topography (a), phase (b), potential (c) images. 1a) roughness on (500 nm)^2 RMS = 0.6 nm, 2a) roughness on (500 nm)^2 RMS = 0.6 nm. Additionally, the absolute work function was shifted from 4.0±0.1eV for the as prepared sample (1c) to 4.6±0.1eV for the plasma treated/annealed sample (2c).*

indicated the conversion of the soft (PEO)MA-PDMS-MA(PEO) at the sample surface into hard inorganic materials.

Since the annealing was done under inert atmosphere at 450°C, all (PEO)MA parts decomposed leaving titania behind and PDMS turned into a silicon oxycarbide matrix meanwhile titania changed from amorphous phase into crystallographic anatase phase resulting in the increase in absolute value of the work function. The x-ray diffractogram of titania particles for as prepared and after annealing is presented in Figure 5.2.1.5, showing typical anatase peaks[103] of TiO_2 for annealing at 450°C and 600°C. After annealing at 1000°C, rutile phase is also observed besides anatase as the extra peaks compared to other annealed samples.

The PDMS block of the templating block copolymer acts as precursor for the insulating polymer derived ceramics[29]. The electronic properties of "SiOC" type ceramics are strongly influenced by the presence or absence of carbon precipitates. The white appearance of the polymeric residue after annealing (Figure 5.1.1.3) shows that no carbon precipitation is evident and the polymer derived ceramic SiOC can be expected to act as an insulator.

Investigation of the surface electrical properties of integrated blocking layer (plasma treated/annealed at 450°C samples) showed the predominant presence of titania on the surface. The existence of charge percolation pathways through the blocking layer was investigated by conductive probe scanning force microscopy (CPM). In order to measure current images the conductive tip of CPM was used as a movable electrode to contact the surface of the nanocomposite films[104, 105]. Samples for CPM measurement were prepared on 50 nm Pt sputtered on Si wafer with 2% titania precursor composition. Figure 5.2.1.6-a1 shows conducting titania parts though which a current >15 pA flows, embedded in an insulating matrix (SiOC). Corresponding topography shows a granular structure with a typical grain diameter of 10-15 nm attributed to titania nanoparticles.
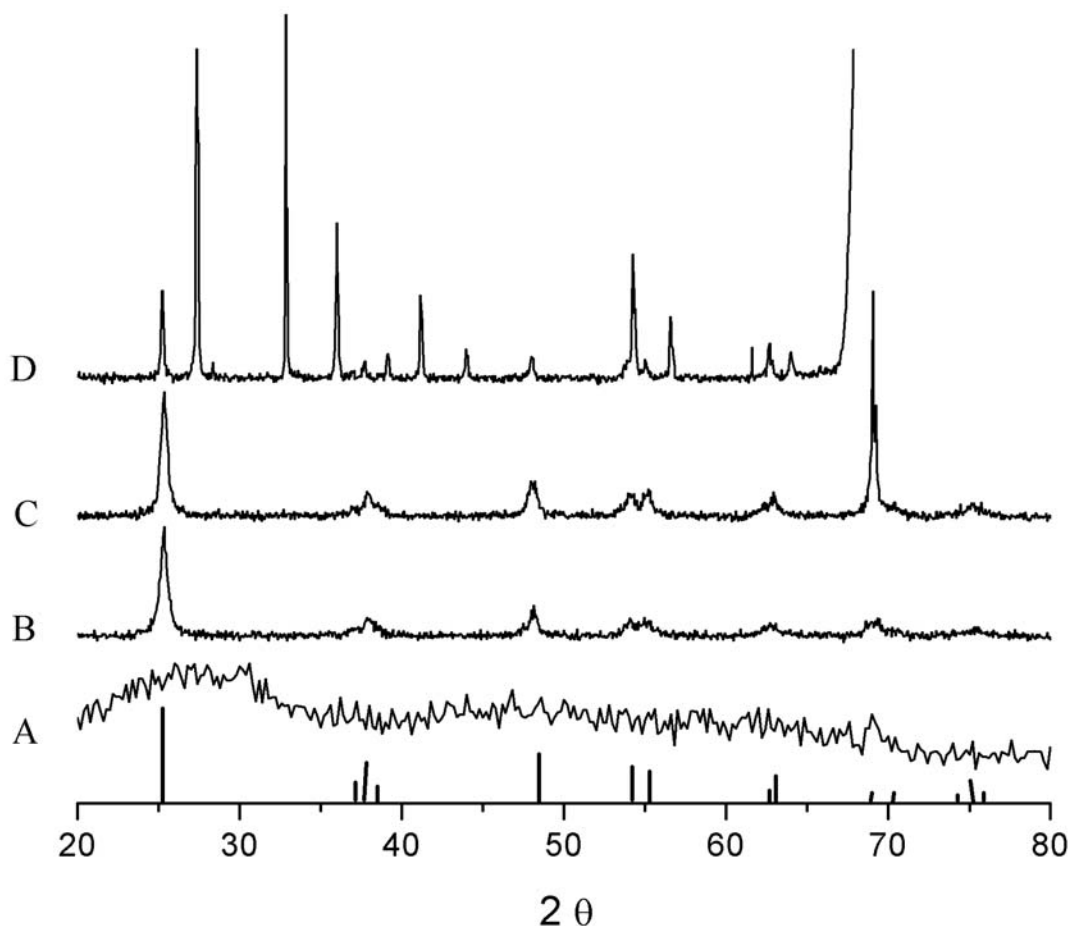
Figure 5.2.1.5. XRD diffractogram of titania/(PEO)MA-PDMS-MA(PEO) nanocomposite films prepared by drop-casting a sol-gel containing 5% titania precursor on Si (100) substrate, (A) as prepared, (B) after annealing at 450°C, (C) after annealing at 600°C and (D) after annealing at 1000°C under nitrogen. The standard anatase TiO_2 diffraction lines[103] are drawn below the observed peaks. Next to (220) peak of TiO_2 at 68.7°, a peak at 69.1° for Si substrate exists. Si peak was very intense after heating at 1000°C, because of this diffractogram ends at that peak for (D). After heating at 1000°C, rutile phase peaks are observed as the extra peaks.

A control measurement on annealed polymer film showed no current flow through the polymer film. In the polymer film holes with a diameter of 100-200 nm diameter and depth of 10 nm were observed (Figure 5.2.1.6-b2). Corresponding conductivity map showed a current flow on the order of nA through these holes which is typical for pinholes in polymer films, i.e. shortcut between CPM tip and the Pt electrode (Figure 5.2.1.6-b1). Since the short cut current is two orders of magnitude larger than the peak current in our integrated barrier layer, we can exclude conductivity via nA sized short cuts as an explanation for the imaged conduction parts. From the CPM experiments we conclude that we were successfully prepared an

integrated blocking layer consisting of a conductive network of titania nanoparticles which are embedded in an insulating polymer matrix.
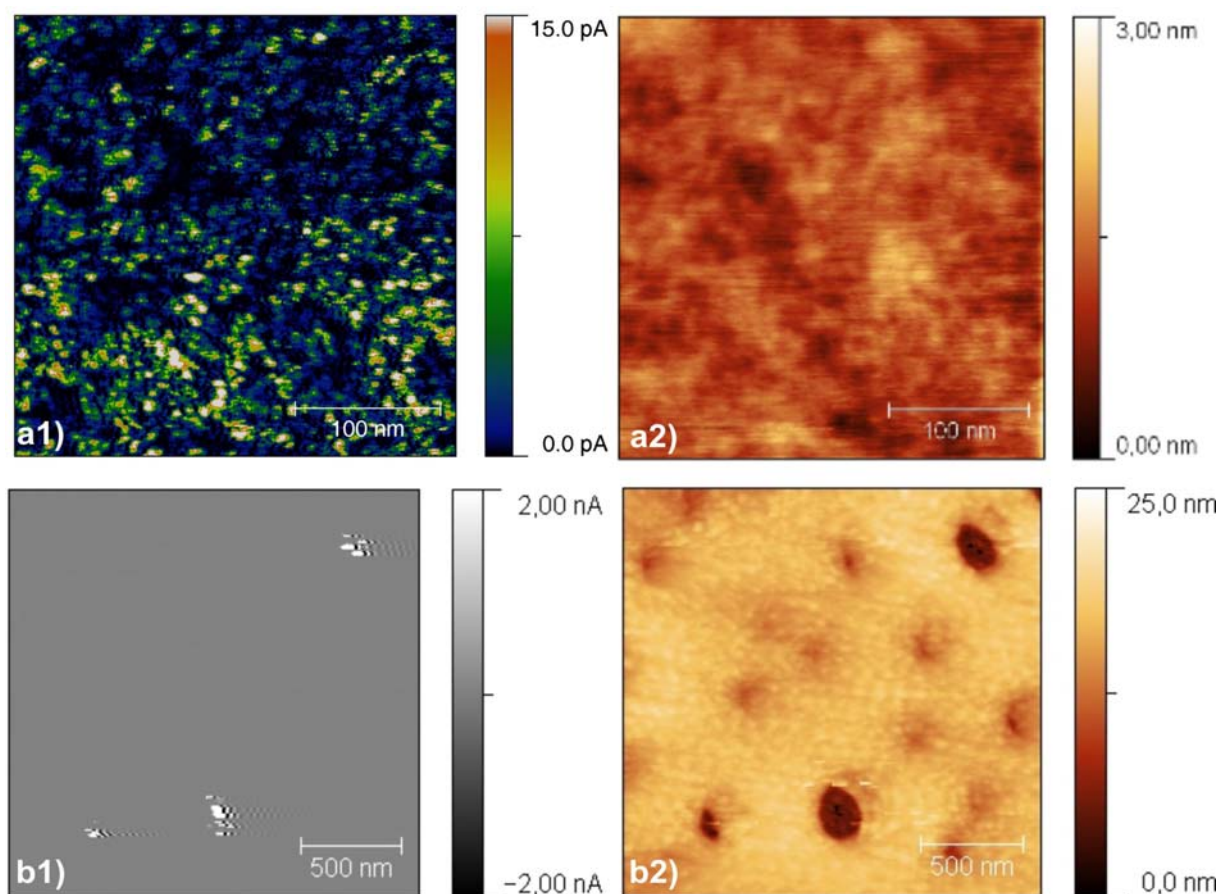

Figure 5.2.1.6. *CPM images of integrated blocking layer (plasma treated/annealed at 450°C).(a) and control sample (PEO)MA-PDMS-MA(PEO) polymer film after annealing at 450°C (b) with potential (1) and topography (2). Current values >15 pA for titania particles and no current flow observed through SiOC matrix (a1). Short circuit current of nA (b1) is observed for the defects (holes) (b2) in the polymer film, where the tip was in direct contact with the substrate. The conductivity in integrated blocking layer is achieved by percolation pathways, excluding short circuit currents which are two orders of magnitude larger, typical for pinholes in polymer films, i.e. a shortcut between CSFM tip and the Pt electrode.*

Microscopy techniques are restricted to an investigation in the μm^2 range. To prove the uniformity of the titania morphology, and to investigate the lateral structure of the titania particles μGISAXS measurements were performed. μGISAXS scattering patterns yield averaged structural information of the illuminated sample spots. In our case this sample spot

was of a size of 1781 x 32 μm^2. This is a consequence of the enlarged footprint at the chosen incident angle of 0.74° and is 225000 times larger than the surface area imaged in Figure 5.2.1.6. Out of plane cuts at an exit angle equal to the critical angle of titania, α_c=0.28°, were performed (Fig. 5.2.1.7), enabling us to obtain averaged structure information about the percolating titania structures in a range from several nanometers up to ~200nm.

For a closer data analysis, the out of plane cuts presented in Figure 5.2.1.7 were fitted according to the Unified Fit Model[106-108]. This model was successfully applied to various scattering experiments in transmission geometry for different applications[107-113]. Lenz et.al. have recently showed that the Unified Fit Model can also be applied to diffuse surface scattering from film samples using grazing incidence geometry[114]. This model describes the structure of the material in structural levels, from single particles to clusters. Each level contains a Guinier regime which describes the size and a power-law regime giving the integral properties of the structure. The Porod regime provides information about particle shape. The power-law exponent, P, gives information about the packing and character of the particles. A value of P=4 corresponds to compact, centro-symmetric particles with low anisotropy, whereas a Gaussian polymer chain in bulk or on a substrate gives a P value of 2.

Starting from the high q-regime, experimental data shows a Porod regime indicated by the constant slope in the log-log plot from q > 0.05 Å^{-1}. This power law regime is followed by a shoulder like Guinier regime until q ≈ 0.012 Å^{-1}. Scattering of this first structural level is followed by another Porod and Guinier regime. The low-q resolution limit resulting from the size of the primary beam at the CCD detector was q < 0.0056 Å^{-1}. Therefore, scattering from the second Guinier regime is limited by the resolution limit. However, the resolution limit was small enough to derive meaningful values for the radius of gyration, R_g, of the second level. The curve progression did not substantially change for the pristine and plasma treated/annealed at 450°C samples indicating the stability of the structure of the titania particles in the polymer matrix upon plasma and heat treatment at 450°C[98]. Table 5.2.1.2 shows the obtained values of the Unified Fit for 1%HCl series.
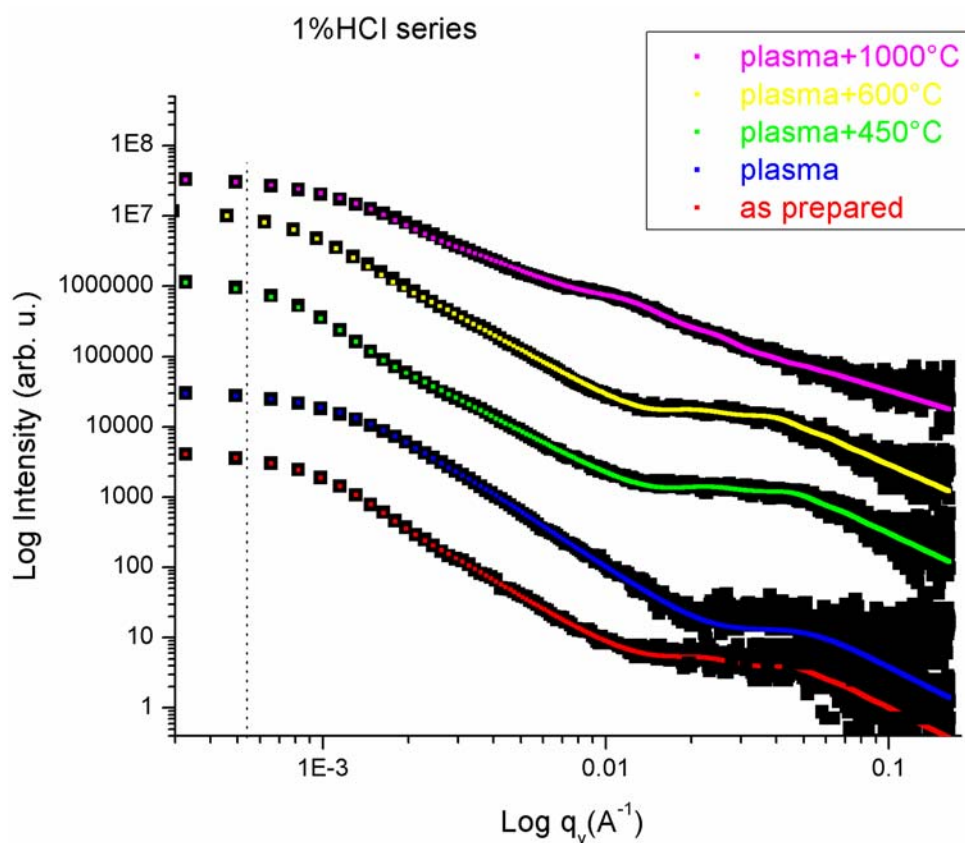
Figure 5.2.1.7. *Double-logarithmic plots of the out-of-plane cuts of the 2d intensity as a function of the q_y component of the scattering vector. The solid lines are the fits from the Unified Fit Model for determining the prominent in-plane length scales. For clarity, the curves are shifted along the intensity axis. The dashed line indicates the resolution limit of the GISAXS experiment. Colored lines are the fits corresponding to the scattering data, in black, below them. From bottom to top, the curves correspond to the as prepared, plasma etched, plasma treated/heated to 450°C, plasma treated/heated to 600°C and plasma treated/heated to 1000°C samples from 1%HCl concentration composition.*

	as prepared	plasma	plasma+450°C	plasma+600°C	plasma+1000°C
Level 1					
P	1.9±0.3	2±0.1	1.9±0.1	1.7±0.1	1.7±0.1
R_g (nm)	7±0.7	6.6±0.3	8±0.3	9±0.2	8±0.5
Level2					
P	2.4±0.1	2.7±0.1	2.1±0.1	2.2±0.1	1.7±0.1
R_g (nm)	170±1.7	127±1.5	214±1.3	192±1.2	131±1.1

Table 5.2.1.2. *Values from the Unified fit model for 1%HCl series.*

The smallest structures obtained from the fits corresponding to the high-q region (q>0.05 Å^{-1}) are the same within the experimental errors for pristine and plasma treated/annealed at 450°C samples. Therefore, the smallest observed titania substructures with R_g of ~7 nm did not change after plasma and heat treatment. For compact spherical particles, P is expected to be 4. The power-law exponent of ~1.9 obtained from the fit is far away from the power-law exponent of compact spherical particles. This can be explained by primary titania particles consisting of a solid titania core covered by a rough titania shell with integrated PEO chains. Ulrich et.al.[25] reported that the metalalkoxide particles prepared by sol-gel chemistry show rough surfaces with incorporated PEO blocks. The PEO chains decompose during heating, leaving porous titania behind. SFM image of nanocomposite films annealed to 1000°C (Figure 5.2.1.3) shows polydisperse particles of a diameter 20 nm without uniform shape in agreement with the x-ray analysis. The second level from the Unified fit model has a size of R_g = 170 nm in the pristine sample and R_g = 214 nm for the plasma treated/annealed at 450°C sample. These values match with the sizes of the circular regions observed in Figure 5.2.1.1-a,c for as prepared and plasma treated/annealed at 450°C samples.

The signal to noise ratio is the highest in plasma treated sample as seen from the experimental data. Therefore, values obtained for the smallest structural level from the fit are not reliable for plasma treated sample. The slope in the middle-q region (0.002<q<0.05 Å^{-1}) increases after plasma treatment compared to as prepared sample, giving a higher P value. This corresponds to more compact particles. After plasma cleaning polymer covering the surface of the particles is removed away. The polymer among the particles is retained at the bottom. The scattering length density of titania and the triblock copolymer is slightly different. When the polymer is removed by plasma cleaning the difference in the electron density of the titania particles and surroundings (less polymer) increases, resulting in a different scattering than the as prepared sample. Heat treatment decomposes the polymer and turns initially amorphous titania into crystalline anatase polymorph. The decrease in the polymer content further increases the electron density difference between titania nanoparticles and surrounding polymer derived ceramic. The change in the material composition results in a different scattering than the plasma treated sample. Although titania changes its phase, the smallest structures do not change, as observed from the fit data. However structures corresponding to second structural level start to form smaller clusters. Annealing at 1000°C decomposes the polymer matrix completely resulting in polymer derived ceramic material as a residue. Meanwhile besides anatase titania, some titania turn into rutile phase. Again change in the

material composition results in change in the scattering. Also this elevated heating decomposes all the polymeric matrix where it was very thin, and smaller clusters form from previous domains. The packing of the clusters decrease thus giving a smaller P value from the fit. In summary, μGISAXS data analysis by the Unified Fit model confirmed that features observed by microscopy techniques accurately represent the structure of 1% HCl titania/(PEO)MA-PDMS-MA(PEO) nanocomposite films over large areas.

5.2.1.1 Effect of sol-gel composition on titania/(PEO)MA-PDMS-MA(PEO) morphology

The effect of sol-gel composition change on morphology of titania/(PEO)MA-PDMS-MA(PEO) nanocomposite films were investigated by changing the amount of the sol-gel components. HCl concentration was raised to 3% and the same plasma and heat treatment were applied. SFM and SEM images of 3% HCl series is shown in Figure 5.2.1.1.1. Color scale correspondence in height and phase images is given in Table 5.2.1.1. μGISAXS experimental data with corresponding fits from the Unified Fit model are given in Figure 5.2.1.1.2.

The number of circular pits decreased with increase in their size compared to 1%HCl series. Pristine sample has a rough surface as seen from different of surface height. Plasma treatment reduces the difference in surface height and circular pits resulting from the miscibility gap during spin-coating appear. Heat treatment does not change the morphology of the film by decreasing the height difference of the structures on the surface. Scattering analysis shows that smallest structures do not change upon plasma treatment and heating at 450°C. These structures form clusters that increase in size by plasma and heating steps with a decrease in their packing. Plasma treatment enlarges the radius of gyration by forming a bridge through primary particles resulting in less packed clusters. This trend is more pronounced after heating at 450°C to 600°C. Packing decreases a lot, by forming larger clusters. Primary structure has R_g of ~9.4 nm in as prepared sample and does not change upon plasma treatment and annealing up to 600°C. The morphology of the structural levels changes gradually by each step. Heating at 1000°C results in a new peak in the middle q regime corresponding to another structural level in between. Heating at 1000°C breaks the binding polymeric residual matrix, and results in smaller clusters with R_g=9.4±2.8nm. These form the bigger cluster of R_g~166nm.
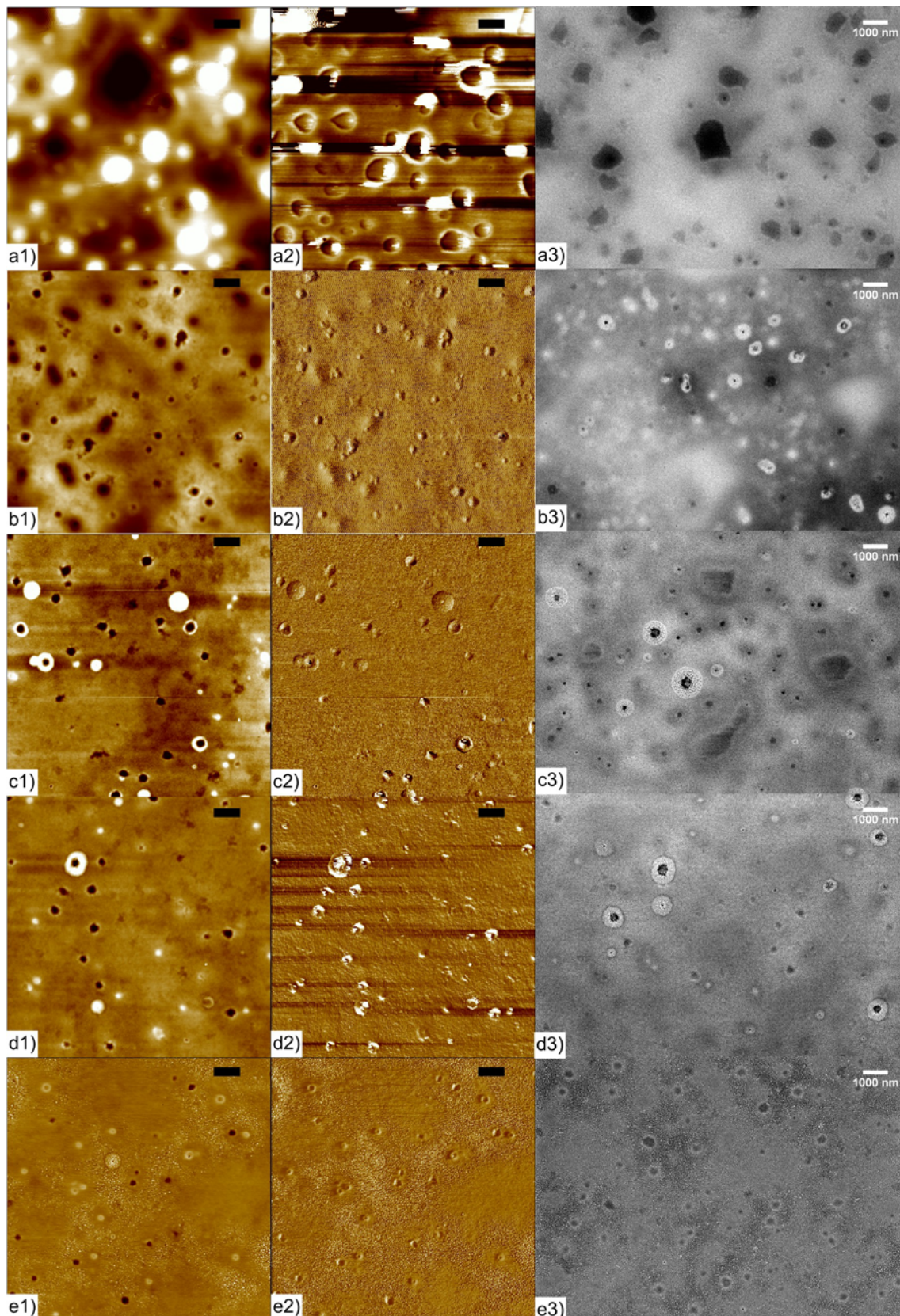
Figure 5.2.1.1.1. *SFM height images on (1), phase on (2) and SEM images on (3) for (a) as prepared, (b) plasma treated, (c) plasma treated/heated to 450°C, (d) plasma treated/heated to 600°C, and (e) plasma treated/heated to 1000°C of 3% HCl series.*
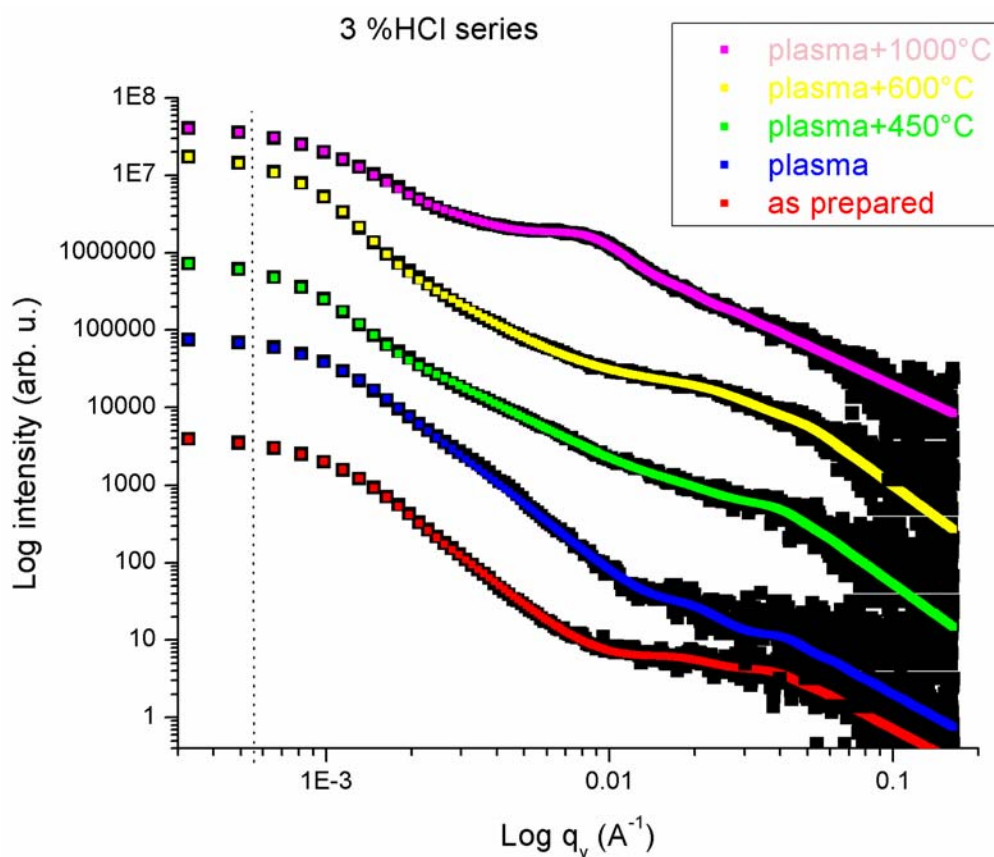
Figure 5.2.1.1.2. *Double-logarithmic plots of the out-of-plane cuts of the 2d intensity as a function of the q_y component of the scattering vector. The solid lines are the fits from the Unified Fit Model for determining the prominent in-plane length scales. For clarity, the curves are shifted along the intensity axis. The dashed line indicates the resolution limit of the GISAXS experiment. Colored lines are the fits corresponding to the scattering data, in black, below them. From bottom to top, the curves correspond to the as prepared, plasma etched, plasma treated/heated to 450°C, plasma treated/heated to 600°C and plasma treated/heated to 1000°C samples from 3%HCl concentration composition.*

	as prepared	plasma	plasma+450°C	plasma+600°C	plasma+1000°C
Level 1					
P	1.9±0.1	2±0.2	2.6±0.1	2.7±0.3	3.8±0.5
R_g (nm)	9.5±0.8	9.4±0.8	9.4±0.7	8.2±0.1	6.2±0.1
Level2					
P	3±0.1	2.8±0.1	1.9±0.1	2.2±0.1	2.1±0.3
R_g (nm)	152±0.9	158±1.1	202±1.5	211±0.9	166±0.1

Table 5.2.1.1.1. *Values from the Unified fit model for 3%HCl series.*

The HCl concentration was raised to 5% in another series. SFM and SEM images of 5% HCl series is shown in Figure 5.2.1.1.3. Color scale correspondence in height and phase images is given in Table 5.2.1.1. µGISAXS experimental data with corresponding fits from the Unified Fit model are given in Figure 5.2.1.1.4. As prepared sample has a rough surface but circular pits are observed. Plasma cleaning makes the pits apparent and heating decreases the surface roughness, and further heating does not affect the morphology according to microscopy techniques. There is a difference with lower HCl series; a larger gap between clusters of circular pits. Plasma treatment changes the scattering in high q region, since it is very noisy no structural information could be obtained. The assumption for 1%HCl series also holds here. Covering matrix removal shrinks the particles to each other and increases the packing with increase in R_g. Heating at 450°C reverses the situation and clusters increase in size and become less dense. At 1000°C a new peak appears again by breaking of the glue among the clusters resulting in smaller one with R_g=19.3±1 nm.

HCl concentration increase does not change the primary structures but affect the clusters. As HCl concentration increases cluster size increases, and since the amount of precursor is the same density or packing of the clusters decrease.
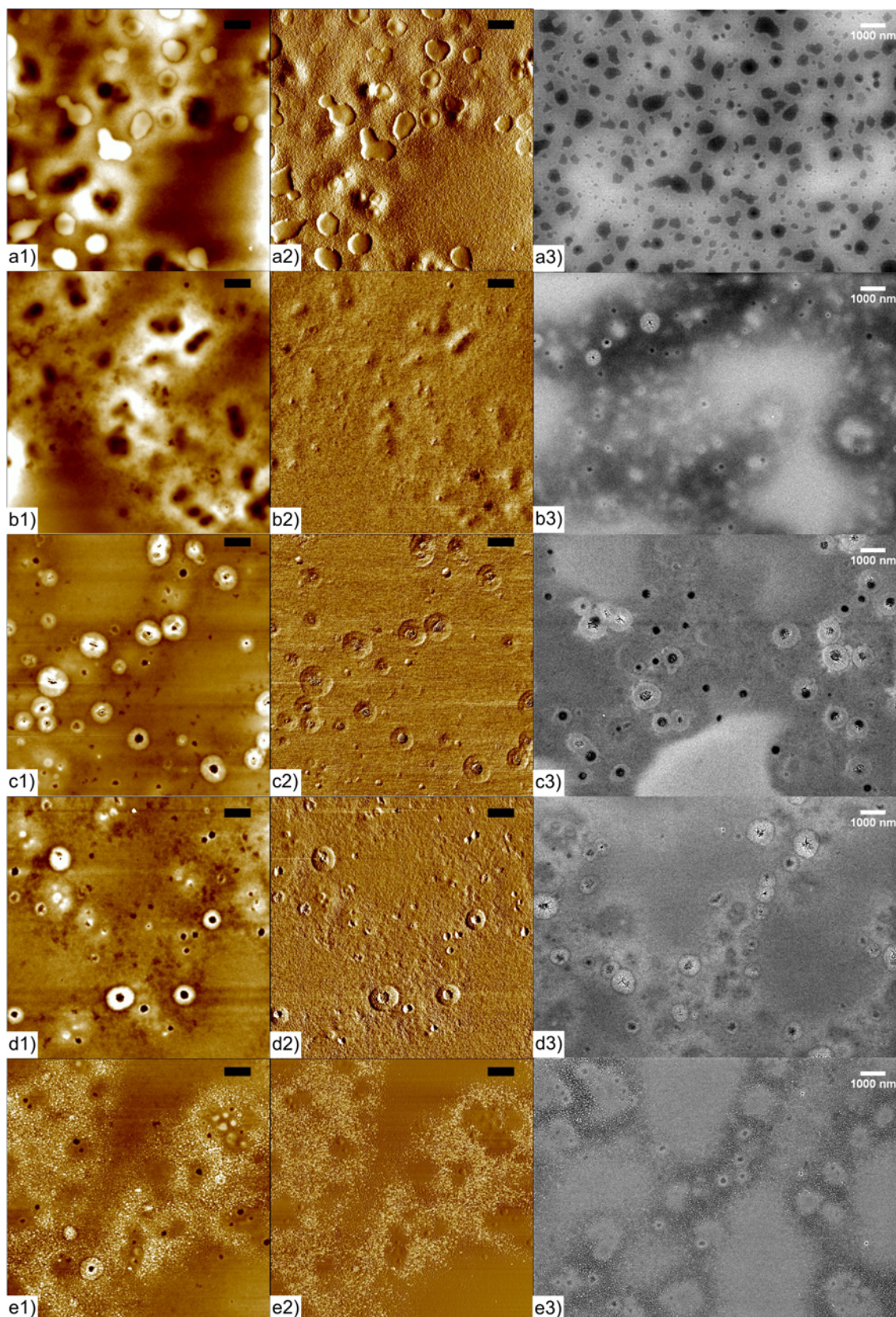
Figure 5.2.1.1.3. *SFM height images on (1), phase on (2) and SEM images on (3) for (a) as prepared, (b) plasma treated, (c) plasma treated/heated to 450°C, (d) plasma treated/heated to 600°C, and (e) plasma treated/heated to 1000°C for 5 % HCl series.*
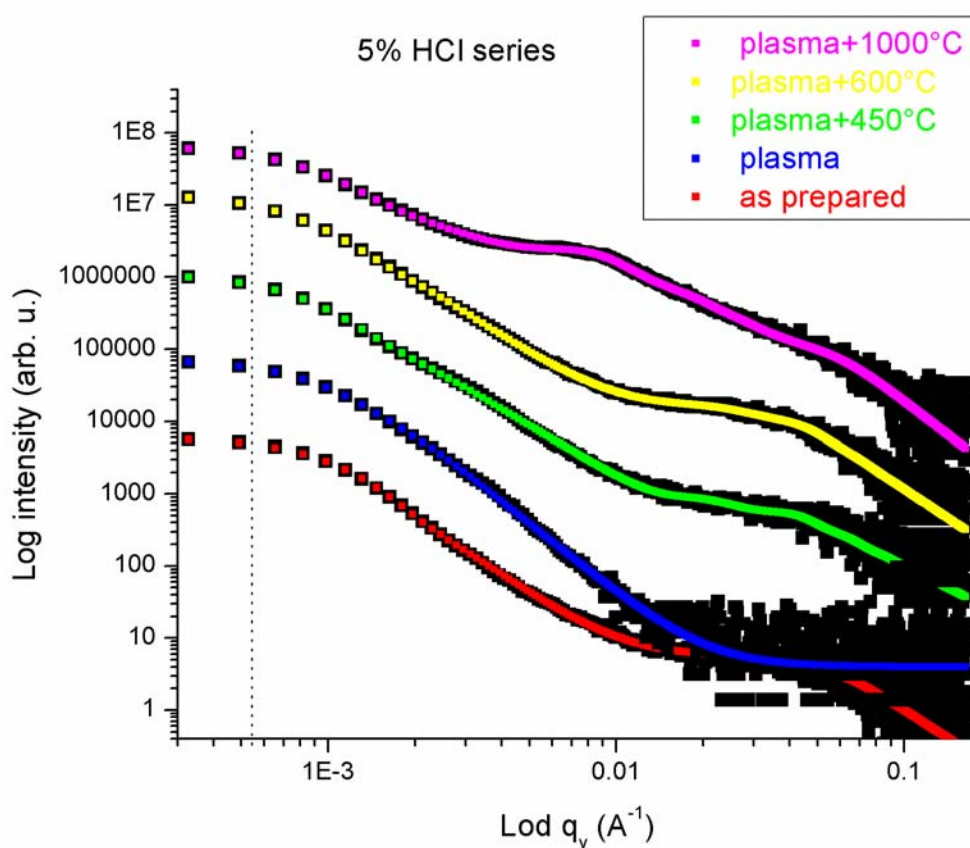
Figure 5.2.1.1.4. *Double-logarithmic plots of the out-of-plane cuts of the 2d intensity as a function of the q_y component of the scattering vector. The solid lines are the fits from the Unified Fit Model for determining the prominent in-plane length scales. For clarity, the curves are shifted along the intensity axis. The dashed line indicates the resolution limit of the GISAXS experiment. Colored lines are the fits corresponding to the scattering data, in black, below them. From bottom to top, the curves correspond to the as prepared, plasma etched, plasma treated/heated to 450°C, plasma treated/heated to 600°C and plasma treated/heated to 1000°C samples from 5%HCl concentration composition.*

	as prepared	plasma	plasma+450°C	plasma+600°C	plasma+1000°C
Level 1					
P	2.3±0.3		2.4±0.2	2.6±0.2	3.8±2.5
R_g (nm)	6.7±0.9		7.9±0.5	9±0.6	7.8±0.1
Level2					
P	2.8±0.1	3.3±0.1	2.3±0.1	2.6±0.1	2.1±0.5
R_g (nm)	160±1.2	173±1.6	203±1.5	208±1.5	192±2

Table 5.2.1.1.2. *Values from the Unified fit model for 5%HCl series.*

The effect of polymer concentration was investigated by doubling the triblock copolymer amount. SFM and SEM images of 2% polymer series are shown in Figure 5.2.1.1.5. Color scale correspondence in height and phase images is given in Table 5.2.1.1. μGISAXS experimental data with corresponding fits from the Unified Fit model are given in Figure 5.2.1.1.6. From images the change of the nanocomposite morphology compared to 1% polymer containing HCl series is seen. Polymer increase results in worm like aggregates. Increased polymer amount enables reordering of the aggregates formed in 1% polymer concentration into cylinder micelles which result in worm like aggregates. Circular pits occurring from liquid/liquid phase separation during spin coating also occur here (Figure 5.2.1.1.7), but they are smaller. Changing the block copolymer amount alters the resultant titania morphology significantly. This is clearly observed by imaging techniques. Besides x-ray scattering reveals different morphology and packing of the particles. μGISAXS and corresponding fits give primary structures of radius ~6nm and clusters of radius ~210nm for as prepared sample. Upon plasma treatment the scattering curve changes, indicating more compact clusters. Heating breaks connections between these large clusters and smaller ones appear. 1000°C heating results in a new peak in medium q range corresponding to R_g of ~47 nm. The radius obtained for clusters, 170nm, also corresponds to the inter distance of worm like structures in the nanocomposite film. These measurements indicate the necessity for further investigation of polymer concentration effect on titania morphology.
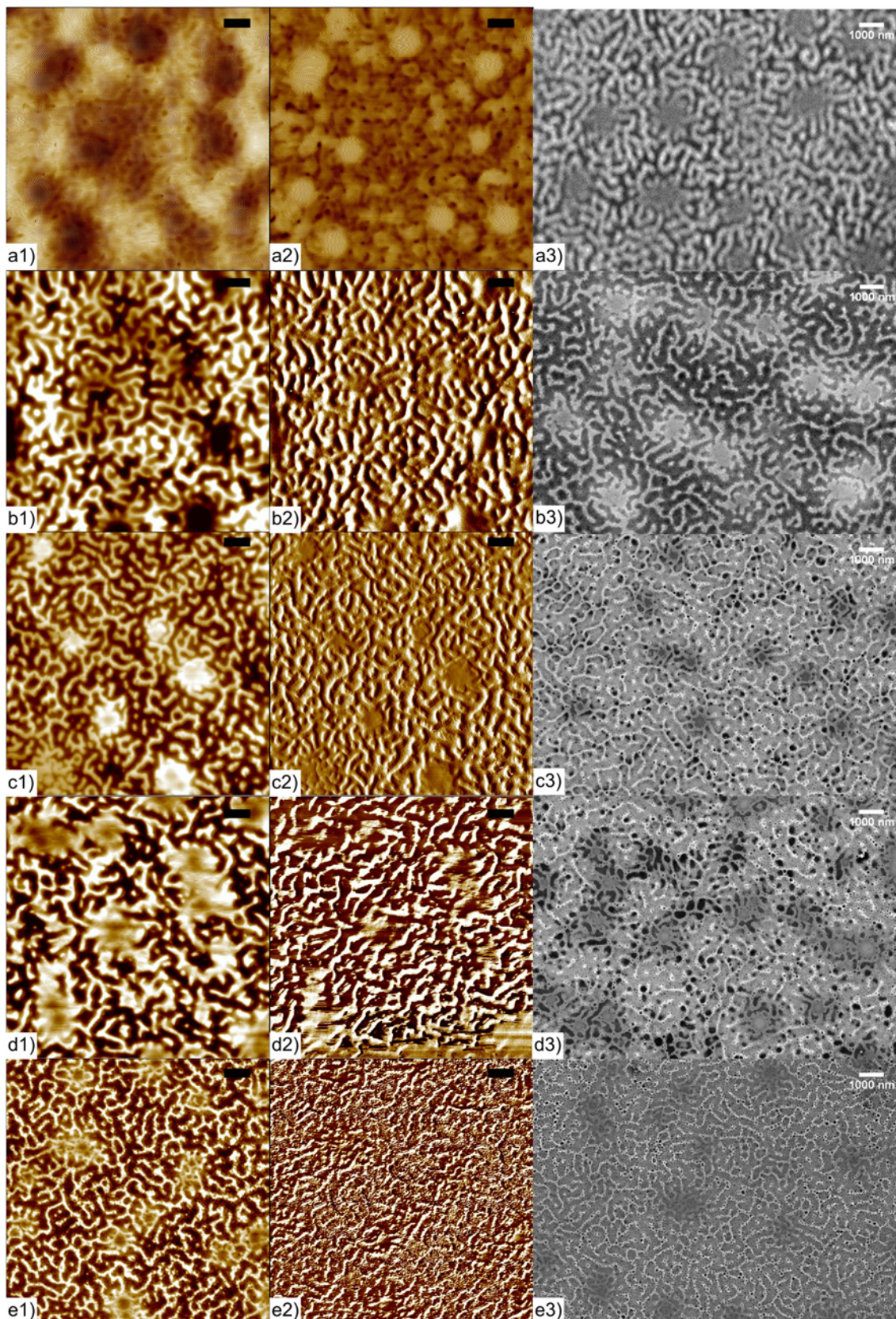
Figure 5.2.1.1.5. *SFM height images on (1), phase on (2) and SEM images on (3) for (a) as prepared, (b) plasma treated, (c) plasma treated/heated to 450°C, (d) plasma treated/heated to 600°C, and (e) plasma treated/heated to 1000° of 2%polymer series.*
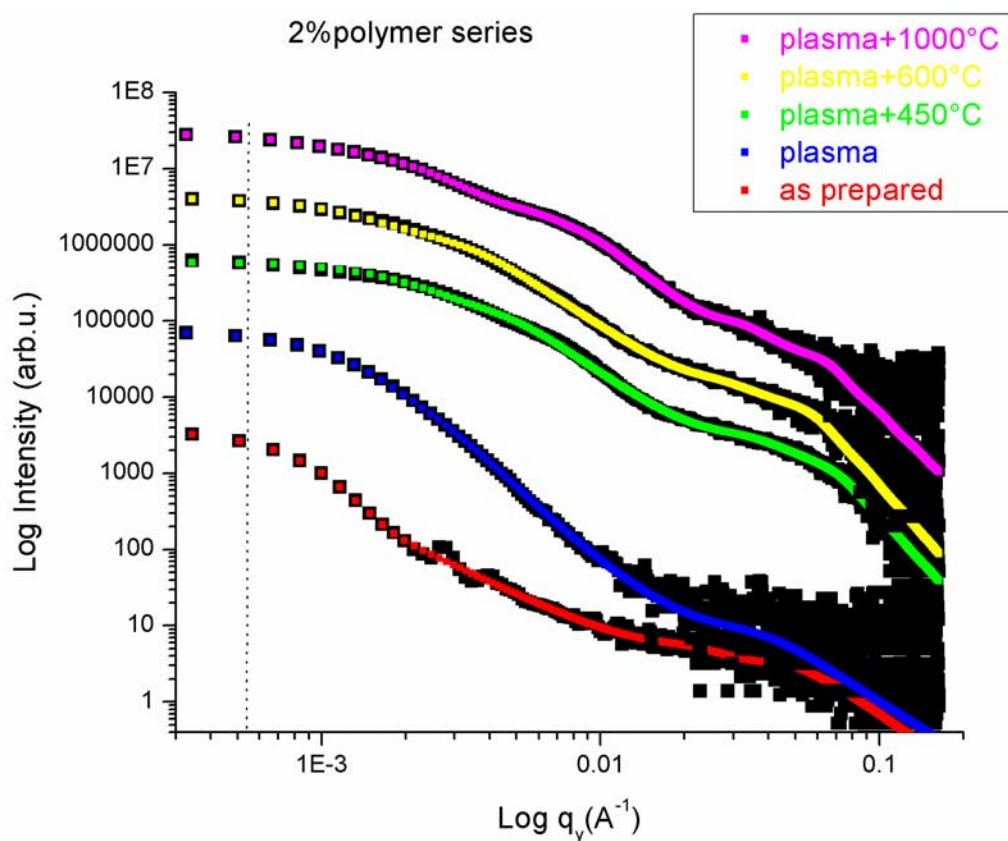
Figure 5.2.1.1.6. *Double-logarithmic plots of the out-of-plane cuts of the 2d intensity as a function of the q_y component of the scattering vector. The solid lines are the fits from the Unified Fit Model for determining the prominent in-plane length scales. For clarity, the curves are shifted along the intensity axis. The dashed line indicates the resolution limit of the GISAXS experiment. Colored lines are the fits corresponding to the scattering data, in black, below them. From bottom to top, the curves correspond to the as prepared, plasma etched, plasma treated/heated to 450°C, plasma treated/heated to 600°C and plasma treated/heated to 1000°C samples from 2%polymer concentration composition.*

	as prepared	plasma	plasma+450°C	plasma+600°C	plasma+1000°C
Level 1					
P	2.5±0.4	2±0.1	4±0.1	4.2±0.3	3.9±2.8
R_g (nm)	6.4±0.6	3.3±0.5	6±0.2	7±0.3	6.5±1.6
Level2					
P	1.8±0.1	4±0.1	2.5±0.1	2.3±0.1	1.5±0.4
R_g (nm)	212±2.1	114±1.3	75±0.8	106±2	171±11

Table 5.2.1.1.3. *Values from the Unified fit model for 2%polymer series.*
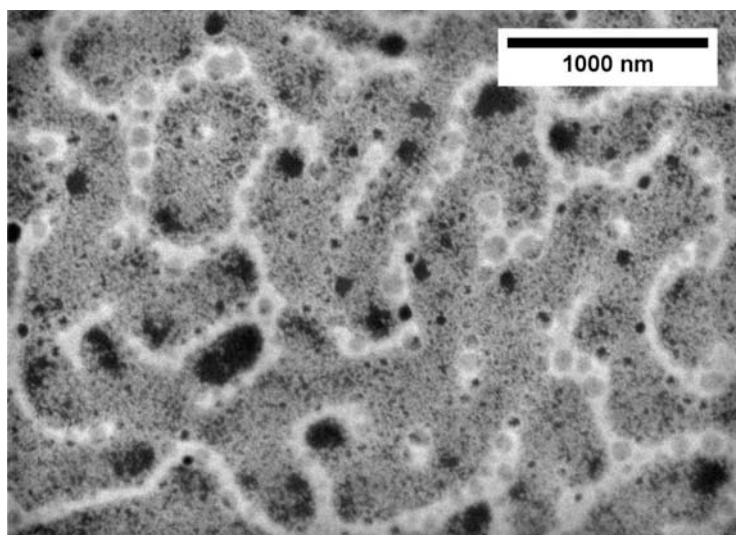
Figure 5.2.1.1.7. *SEM image of 2% polymer plasma treated/annealed at 450°C sample.*

Titania precursor concentration was also increased to 2% by weight. SFM and SEM images of 2% TTIP series are shown in Figure 5.2.1.1.8. Color scale correspondence in height and phase images is given in Table 5.2.1.1. µGISAXS experimental data with corresponding fits from the Unified Fit model are given in Figure 5.2.1.1.9. Microscopy images show similar morphology to HCl concentration series since both have the same disturbing effect as the poor solvent to PDMS part of the block copolymer to the sol-gel. Plasma treatment results in shrinkage of clusters to each other increasing the packing, but again heating acts in the reverse direction. Packing decreases with larger cluster formation. However, primary structures show high packing with P close to 4. Although this decreases after heating at 600°C, it increases to the same value after heating to 1000°C. Heat treatment at 1000°C also results in a new peak in middle q regime with R_g=19.4±1.6 nm indicating smaller cluster formation. The circular pit formation during spin coating resulted in reverse pits in some of this series (Fig.5.2.1.1.10). Instead of circular pits circular hills are formed. This may be due to higher titania content resulting in denser regions where liquid-liquid phase separation occurs. Quick drying results in freezing of these structures before they collapse into circular pits.
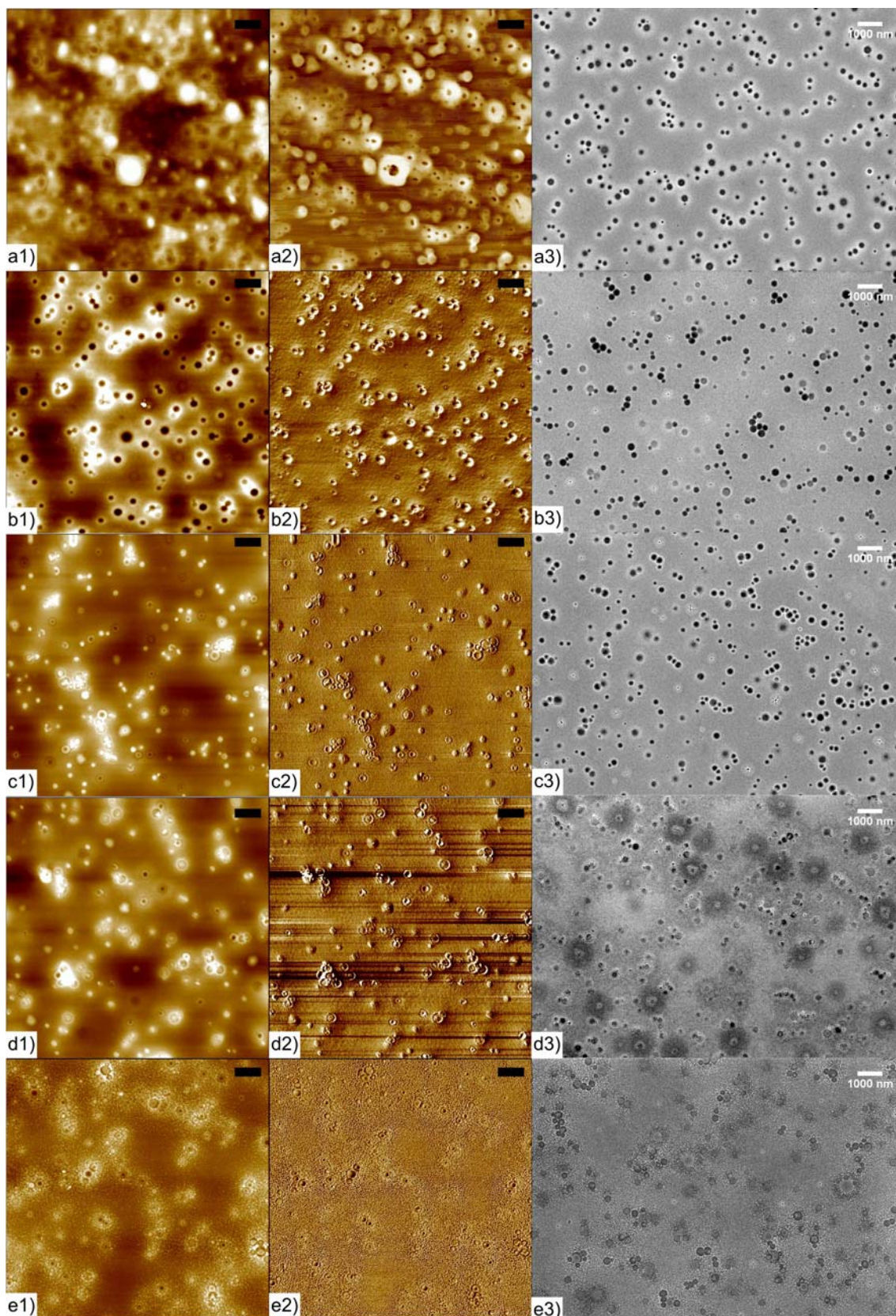
Figure 5.2.1.1.8. *SFM height images on (1), phase on (2) and SEM images on (3) for (a) as prepared, (b) plasma treated, (c) plasma treated/heated to 450°C, (d) plasma treated/heated to 600°C, and (e) plasma treated/heated to 1000°C of 2%TTIP series.*
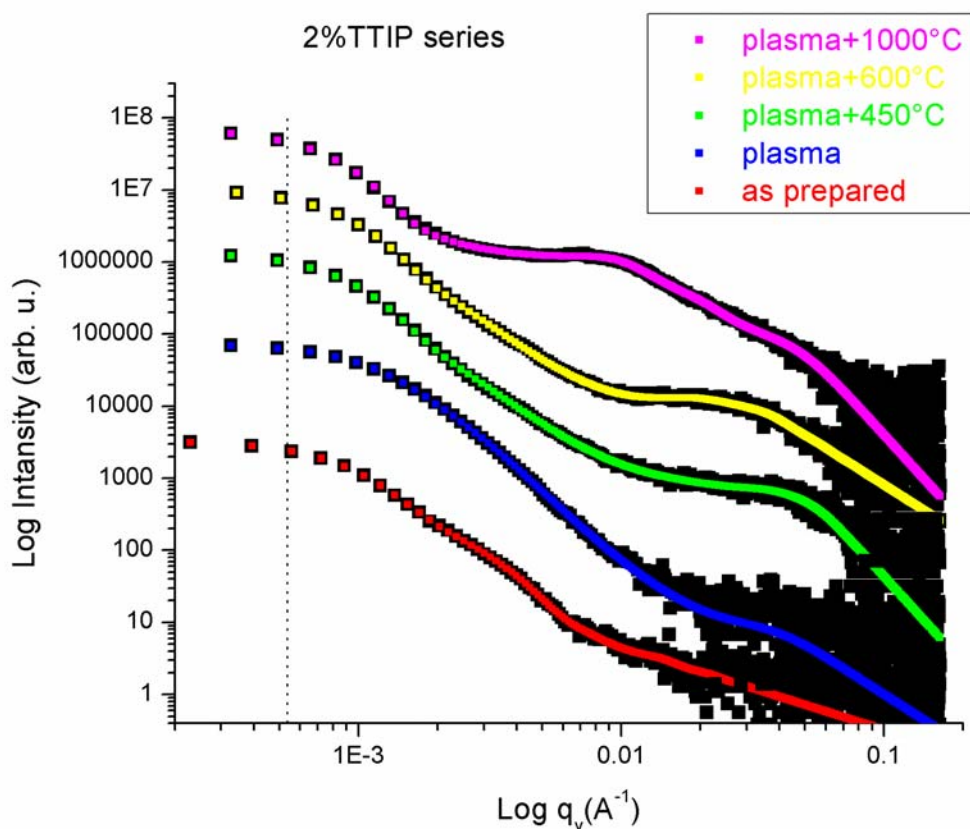
Figure 5.2.1.1.9. *Double-logarithmic plots of the out-of-plane cuts of the 2d intensity as a function of the q_y component of the scattering vector. The solid lines are the fits from the Unified Fit Model for determining the prominent in-plane length scales. For clarity, the curves are shifted along the intensity axis. The dashed line indicates the resolution limit of the GISAXS experiment. Colored lines are the fits corresponding to the scattering data, in black, below them. From bottom to top, the curves correspond to the as prepared, plasma etched, plasma treated/heated to 450°C, plasma treated/heated to 600°C and plasma treated/heated to 1000°C samples from 2%TTIP concentration composition.*

	as prepared	plasma	plasma+450°C	plasma+600°C	plasma+1000°C
Level 1					
P	1.5±0.3	2.5±1.9	4±0.4	2.3±0.2	4±0.2
R_g (nm)	6.4±0.7	5.6±1.2	7.3±0.5	11.7±0.8	7.7±0.4
Level2					
P	2.4±1.5	3.5±0.1	2.6±0.1	2.6±0.1	1.9±0.4
R_g (nm)	190±3.4	138±1.1	188±1	193±1.1	220±1.8

Table 5.2.1.1.4. *Values from the Unified fit model for 2%TTIP series.*
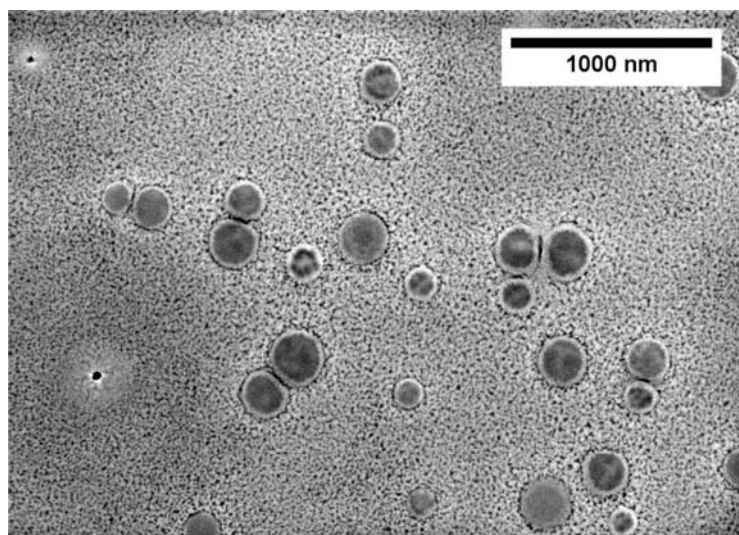
Figure 5.2.1.1.10. *SEM image of 2% TTIP plasma treated/annealed at 600°C sample.*

A side view of 2% TTIP plasma treated/annealed at 450°C was obtained by TEM (Fig. 5.2.1.1.11). For obtaining a TEM image of prepared nanocomposite films, focused ion beam is used. A lamella is cut through the film on Si wafer. Then this lamella was investigated by TEM. Since the lamella was thick, very sharp images could not be obtained. However crystalline TiO_2 particles as pointed by the arrows surrounded comparatively amorphous materials in the figure are seen. The dark region on the left of the crystals is Pt, and Si substrate on which the nanocomposite film was prepared is seen as thin line on the right of the crystals. The scale bar of the image corresponds to 20 nm and this is in correlation with the thickness of the films obtained from x-ray reflectivity for 1% titania precursor containing plasma treated/annealed at 450°C nanocomposite films (~18 nm). Since titania precursor amount is increased to 2% in this sample, slightly thicker nanocomposite film is expected as observed from the TEM image.
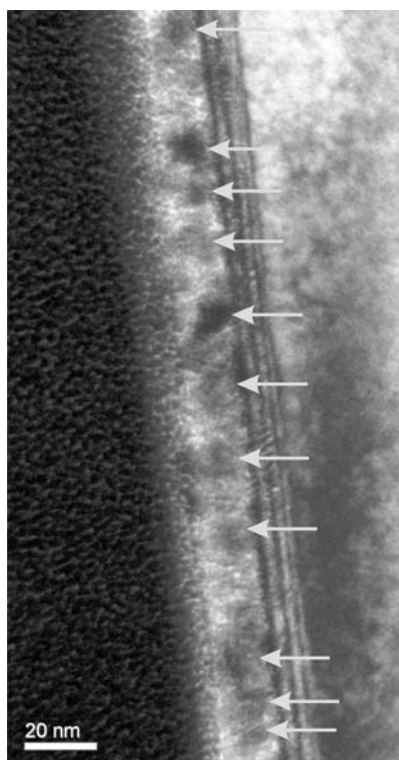
Figure 5.2.1.1.11. *TEM image of a lamella cut through the 2% TTIP plasma treated/annealed at 450°C by FIB. Dark regions indicate the crystalline particles.*

Changing the sol-gel components of our titania/(PEO)MA-PDMS-MA(PEO) system resulted in different morphologies. The change in the sol-gel composition was small, showing accordingly small changes in the nanocomposite morphology. Analysis of scattering experiments using the Unified fit model is summarized in Figure 5.2.1.19.

(PEO)MA-PDMS-MA(PEO) content increase from 1 to 2% resulted different morphology as also observed by microscopy imaging. Primary structures were smaller in 2% polymer series and they formed smaller clusters than other series. The reduction of primary titania particle size is very important for application in solar cells. Obtained primary titania particles are around 15 nm from 2% polymer series. The exciton diffusion length is around 10-20nm[115] and morphologically controlled reduction of the crystallite size is promising for further investigation for application in hybrid organic solar cells.

Altering the HCl concentration showed no significant change in size of primary particles, but only a slight increase the cluster size. TTIP increase resulted in the same morphology as HCl series since both act as the poor solvent for the PDMS part. Packing density of titania increases as the concentration of titania increased.
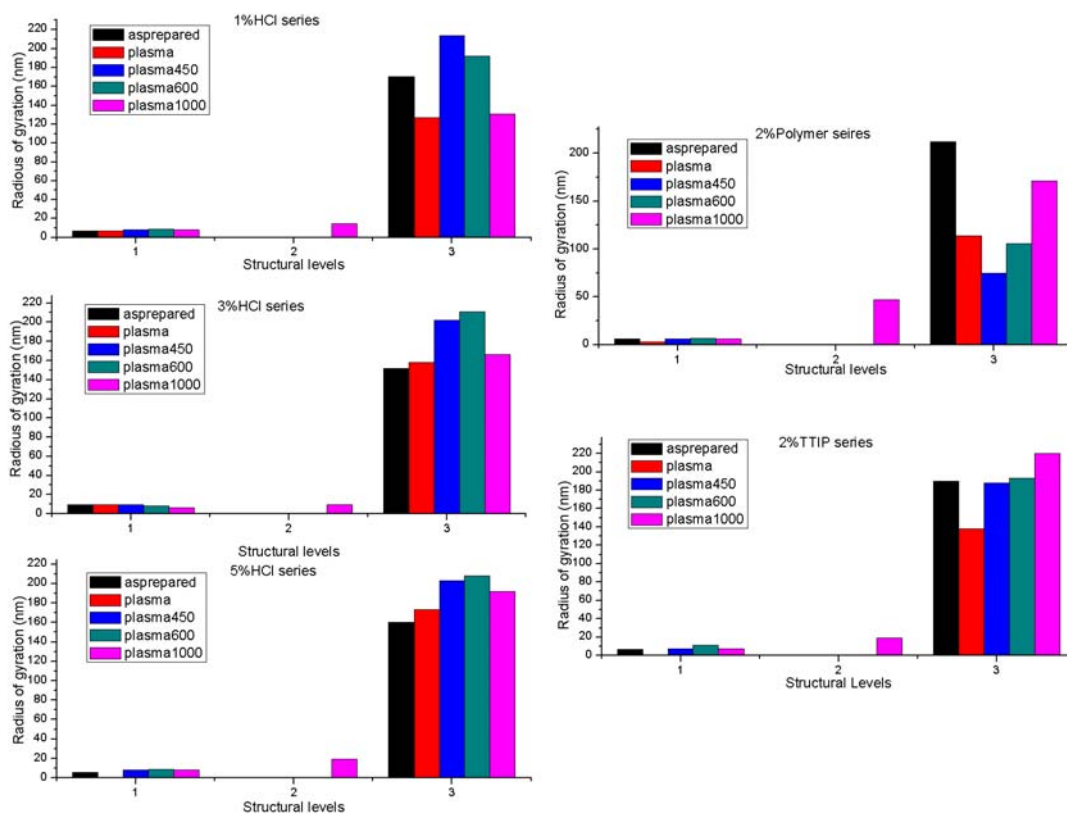
Figure 5.2.1.19. *Summary of structural level sizes obtained from fits by the Unified fit model for 1%HCl, 3%HCl, 5%HCl, 2%polymer and 2%TTIP series.*

Heat treatment converted the template from a soft polymer into a hard solid matrix. This resulted in smaller cluster formation on the expense of larger ones. The highest temperature application dramatically broke the binding material among clusters and a new corresponding peak in scattering experiments appeared in all series.

From these small set of investigations of the sol-gel composition effect on resultant titania morphology, further investigation by increasing the polymer content with increase in titania concentration will be helpful for obtaining controlled charge percolation pathways in desired density in the integrated blocking layer for hybrid organic solar cell applications.

The photoluminescence of the prepared series were also examined. Figure 5.2.1.10 shows the photoluminescence spectra for as prepared, plasma treated, plasma treated/annealed at 450°C, plasma treated/annealed at 600°C and plasma treated/annealed at 1000°C samples of 1%HCl, 3%HCl, 5%HCl. 2% polymer and 2%TTIP composition series. All samples show

101

considerable peaks indicating photo activity upon illumination. To obtain a closer analysis of the source of photo activity, each photoluminescence spectrum was analyzed by fitting with Lorentzian for four peaks located at ca. 398nm, 435nm, 469nm and 510 nm (Figure 5.2.1.11). The peaks can be assigned to self-trapped excitons localized either in TiO_6 octahedron (peak at 398nm), oxygen vacancies (peaks at 469 and 510nm) or surface defects (peak at 435 nm)[27, 116, 117]. The PL spectra of all samples showed the same defects from preparation, and these defects were conserved after plasma and heat treatments. However no further investigation for the defects and their effects on the conductivity of the titania was made.
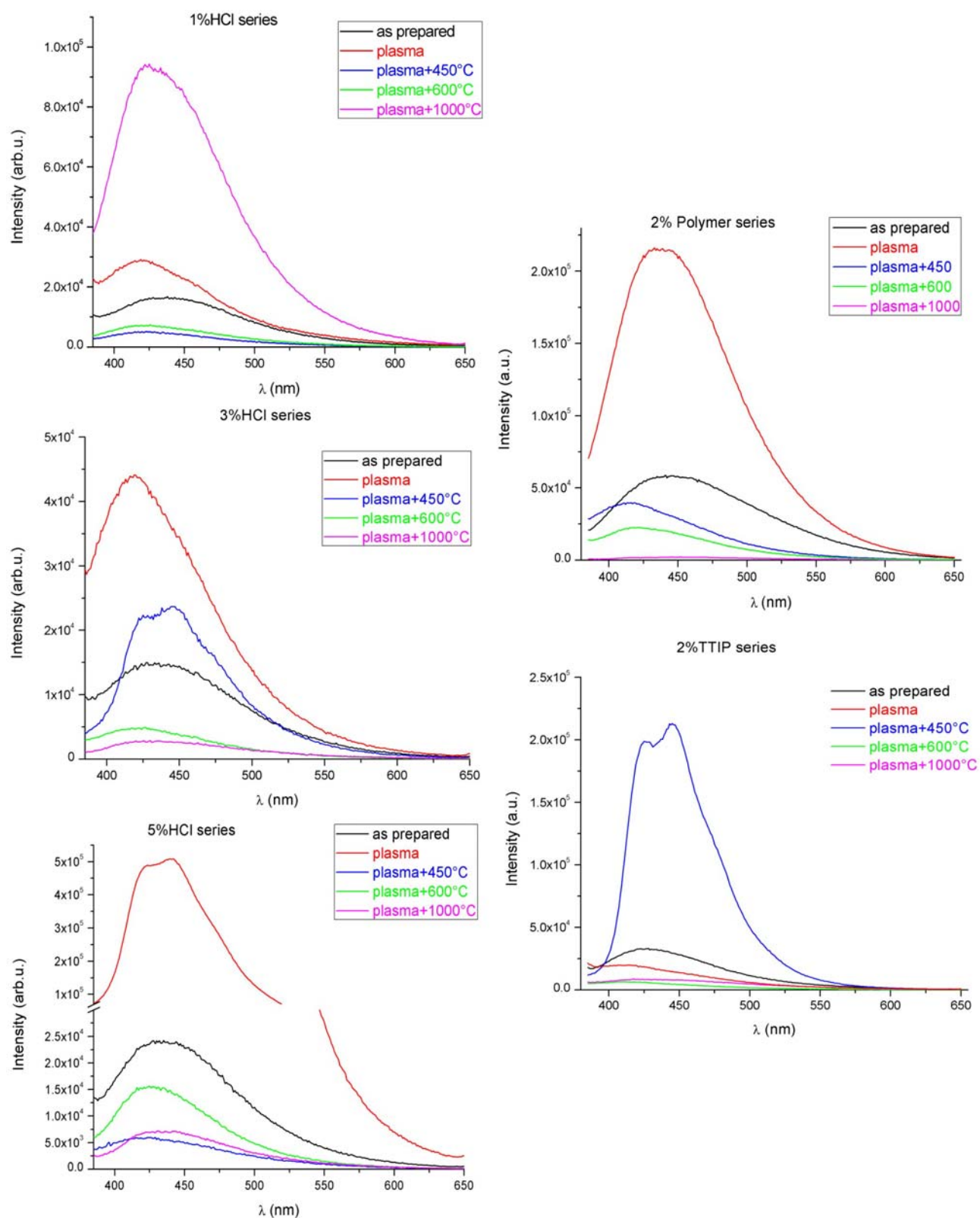
Figure 5.2.1.20. *PL spectra of as prepared, plasma treated, plasma treated/annealed at 450°C, plasma treated/annealed at 600°C, plasma treated/annealed at 1000°C samples of 1%HCl, 3%HCl, 5%HCl, 2%polymer and 2%TTIP series.*
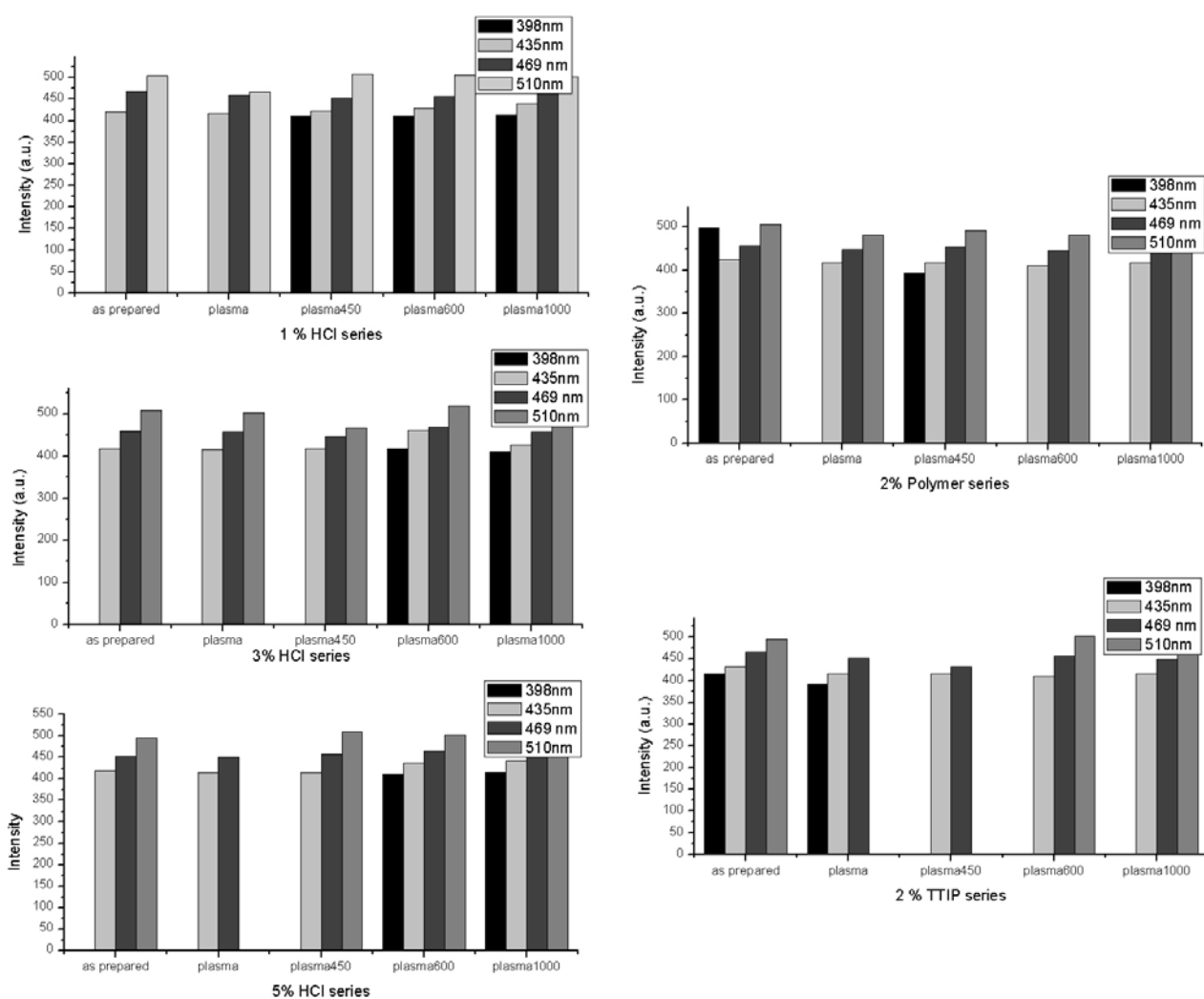
Figure 5.2.1.21. *Lorentzian fits of PL spectra of as prepared, plasma treated, plasma treated/annealed at 450°C, plasma treated/annealed at 600°C, plasma treated/annealed at 1000°C samples of 1%HCl, 3%HCl, 5%HCl, 2%polymer and 2%TTIP series for peaks at 398, 435, 469 and 510 nm..*

5.2.2 PDMS-MA(PEO)/Titania Nanocomposite Films

PDMS-MA(PEO) block copolymers with same molecular weight ratio (1:1) were used to prepare titania nanocomposite films in 1%HCl composition. Their morphology was investigated by SEM. Figure 5.2.2.1 and Figure 5.2.2.2 show the images obtained from PDMS(5000)-MA(PEO)/titania and PDMS(10000)-MA(PEO)/titania nanocomposite films, respectively. The same treatment steps of plasma and annealing were applied, and SEM images of plasma and heat treated samples are presented in the figures. Annealing at 1000°C enabled to obtain sharper images for seeing the titania clusters. Both series show similar morphologies mainly representing the circular pits which occurred due to liquid-liquid phase

separation during spin-coating[99]. The only difference between 1%HCl triblock copolymer series is the accumulation of the circular pits next to each other as the molecular weight increased in the diblock copolymer series. This may result from the difference of the triblock and diblock copolymer behavior in the sol-gel composition. There was not an apparent difference in the nanocomposite morphology from microscopy images. Thus, no further investigation on the sol-gel composition was performed.
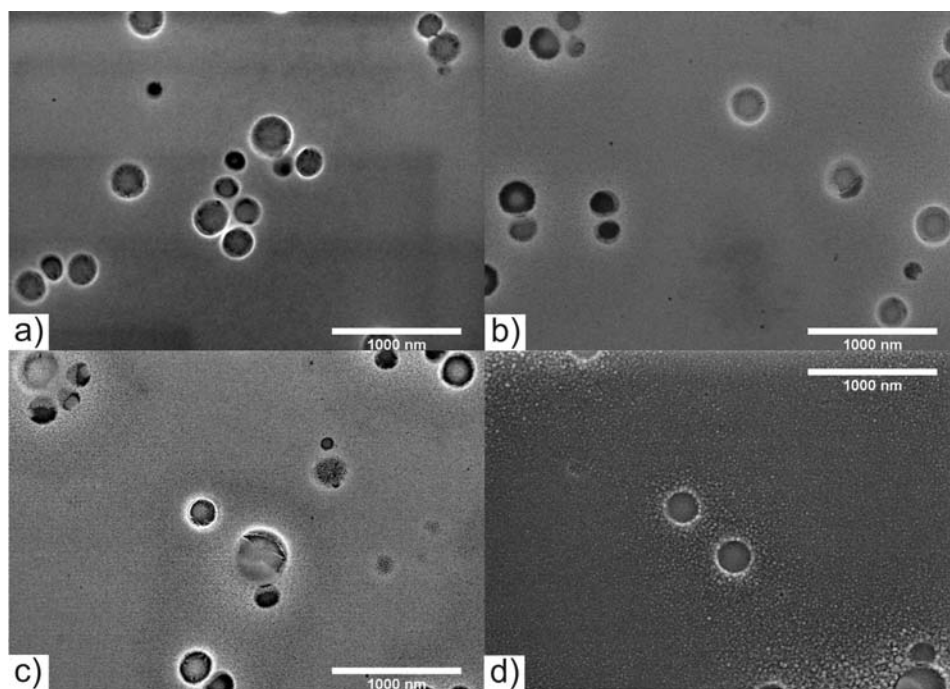
Figure 5.2.2.1. *SEM images of PDMS(5000)-MA(PEO) plasma treated (a), plasma treated/annealed at 450°C (b), plasma treated/annealed at 600°C (c), plasma treated/annealed at 1000°C (d).*
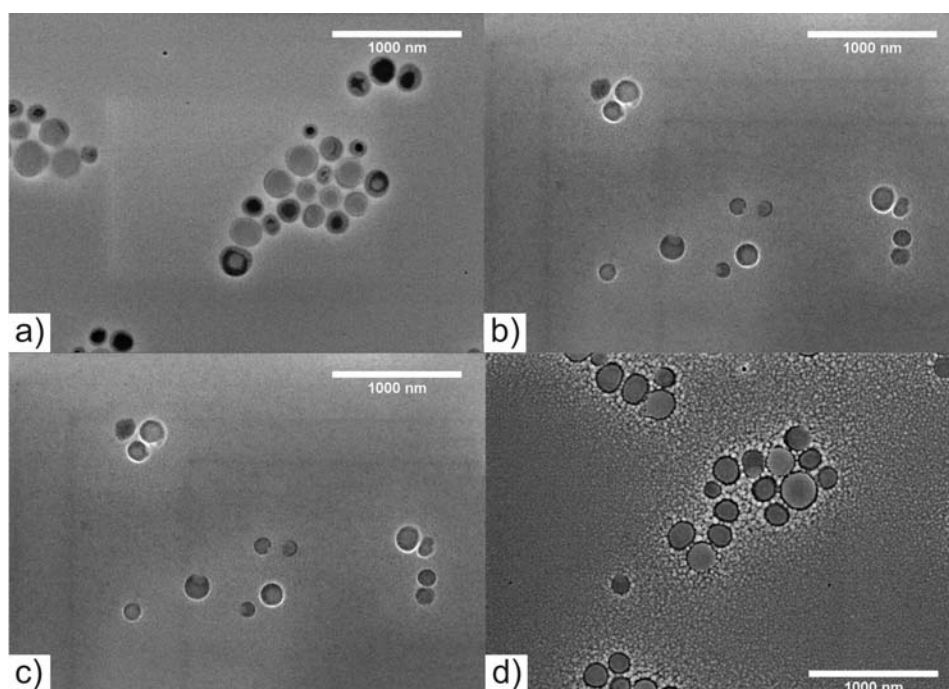
Figure 5.2.2.2. *SEM images of PDMS(10000)-MA(PEO) plasma treated (a), plasma treated/annealed at 450°C (b), plasma treated/annealed at 600°C (c), plasma treated/annealed at 1000°C (d).*

5.2.3   PEO-MA(PDMS)/Titania Nanocomposite Films

Titania nanocomposite films were prepared by PEO-MA(PDMS) diblock copolymer as the templating agent in 1%HCl composition and the same treatments were applied. Again the circular pits due to miscibility gap during fast drying process in spin-coating appeared as large distinctive features in microscope images (Fig.5.2.3.1). Heating to 450°C after plasma treatment enabled higher magnification imaging and foam like structure formation was observed (fFig.5.2.3.1-c).
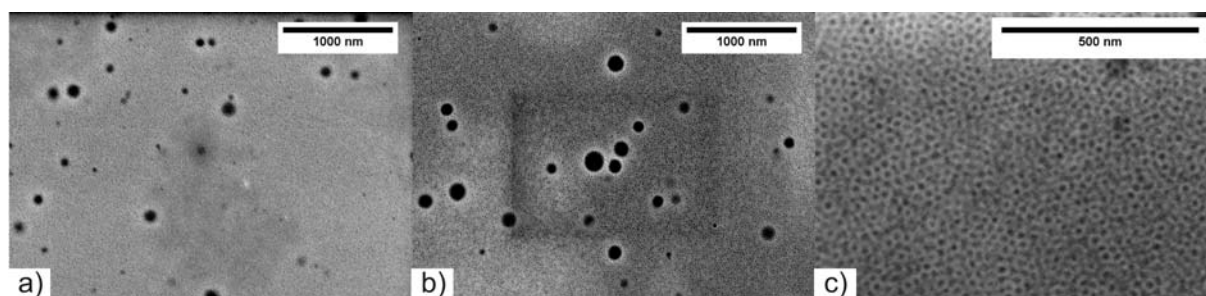

Figure 5.2.3.1. *SEM images of a) as prepared, b) plasma treated, c) plasma treated/annealed at 450°C titania/PEO-MA(PDMS) nanocomposite films.*

μGISAXS measurement showed sharper peaks compared to all (PEO)MA-PDMS-MA(PEO) series (Figure.5.2.3.1). This is an indication of ordered structure formation with less polydispersity in structure sizes. Two peaks are apparent in the as prepared sample around q~0.025 Å^{-1} and q~0.04 Å^{-1}. After plasma treatment these peaks stay at around same place and a new peak in lower q values ~0.013 Å^{-1} appear, and these peaks present after heating the plasma treated sample with a little shift to higher q values, indicating that structures get smaller. The q values where the peaks appear are listed in Table 5.2.3.1. Corresponding center to center distances were calculated by using Eqn. 3.2.9.10. After plasma treatment the polymer matrix on the surface is removed and this enabled the ~25nm distanced structures to make up a large cluster with the particles in ~50 nm distance. This shows a network formation among the structures. SEM image after plasma treatment and heating confirm a network of foam like particles.

To see the effect of further heating on the nanocomposite film morphology another batch of same composition was prepared. After plasma treatment samples were heated to 450°C, 600°C and 1000°C. Although the composition was the same, a little distorted foam morphology was observed (Figure 5.2.3.4-c). This may be due to the purity of the sol-gel components. Shelf life may have decreased the purity by increase in the water content of the components.
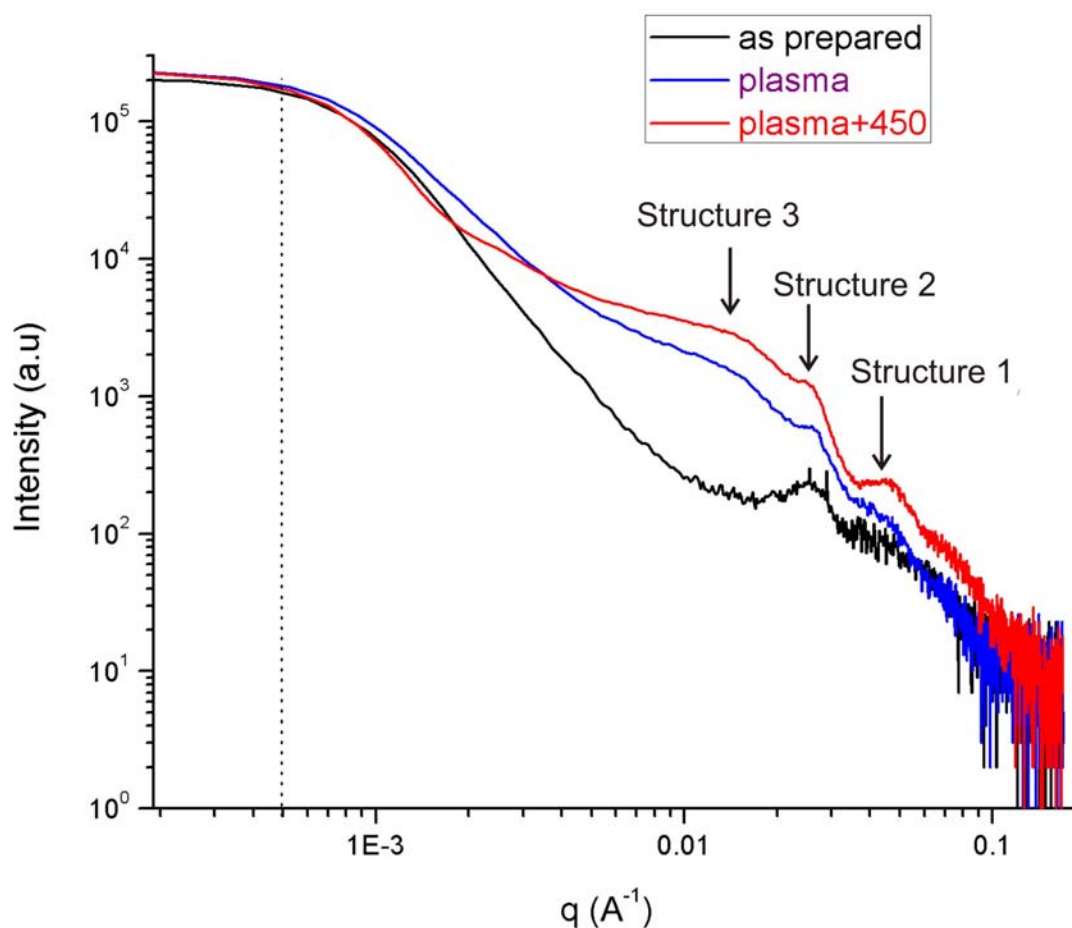
Figure 5.2.3.2. *Double-logarithmic plots of the out-of-plane cuts of the 2d intensity as a function of the q_y component of the scattering vector. The dashed line indicates the resolution limit of the GISAXS experiment. From bottom to top, the curves correspond to the as prepared (black), plasma treated (blue), plasma treated/heated to 450°C (red) samples from 1%HCl concentration of PEO-MA(PDMS) sol-gel.*

	Structure 1	Structure 2	Structure 3
as prepared	q=0.04 Å^{-1}→16±1 nm	q=0.025 Å^{-1}→25.3±2 nm	
plasma	q=0.04 Å^{-1}→16±1 nm	q=0.026 Å^{-1}→23.9±2 nm	q=0.013 Å^{-1}→50±4 nm
plasa+450	q=0.047 Å^{-1}→13.4±1 nm	q=0.04 Å^{-1}→24.2±2 nm	q=0.014 Å^{-1}→45±4 nm

Table 5.2.3.1. *Peaks obtained from GISAXS experiment data and corresponding center to center distance values.*
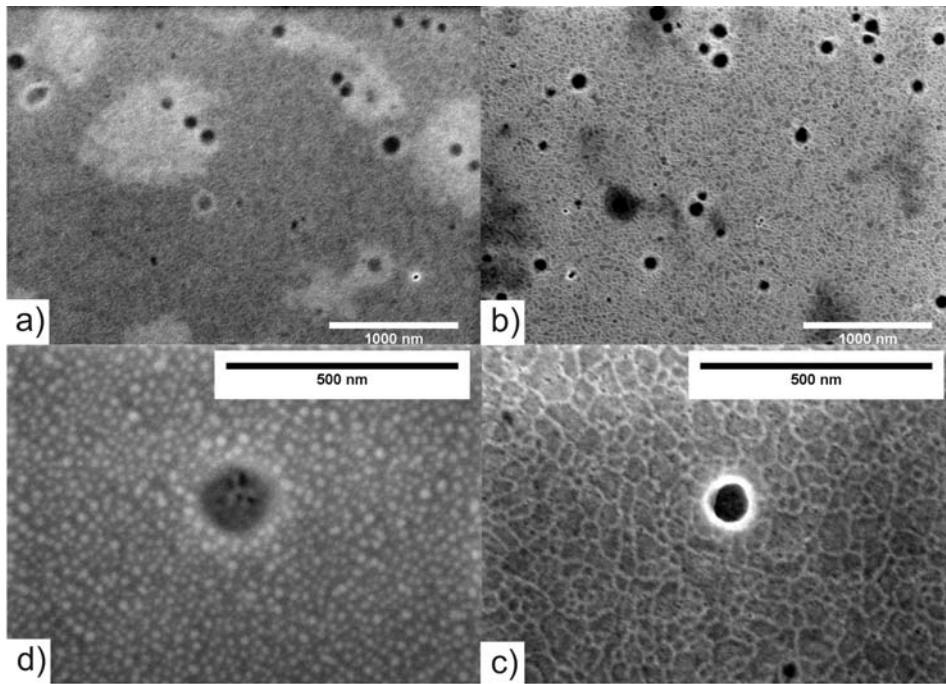
Figure 5.2.3.4. *SEM images of a) plasma treated, b) plasma treated/annealed at 450°C, c) plasma treated/annealed at 600°C, d) plasma treated/annealed at 1000°C titania/PEO-MA(PDMS) nanocomposite films.*

Heat treatment to 1000°C again enabled to see titania clusters by SEM, which are similar to all series' plasma treated/annealed at 1000°C samples.

Observation of comparatively ordered structures by using PEO-MA(PDMS) is due to the difference of the morphology and shape change of the polymers. Here, PEO is the linear block with PDMS as pendant groups. The synthesis of this polymer needs to be optimized to obtain higher yields for further investigation of the sol-gel composition difference effect on titania morphology. Then their application in hybrid solar cells as the integrated blocking layer could be investigated.

6   Application in Solar Cells

Technologies of the 21st century created an increasing demand for energy that increased the need for new forms of energy conversion. Declining supply of fossil fuels and their waste contribution to environmental pollution, whose affects are seen in global warming, made alternative renewable energy production the primary subject of the world. Methods for converting wind, hydroelectric and solar energy into electrical energy are explored to solve the world's energy problem[118]. The abundance and consistency of sunlight makes the solar energy very attractive. Therefore, inorganic semiconductors and organic based solar cells have been explored to develop efficient and inexpensive method for conversion of sunlight into energy.

After the first fabrication of dye sensitized mesoporous TiO_2 solar cells[1] with energy conversion efficiencies up to 10%, solid state dye sensitized photovoltaic devices using p-type semiconductors instead of the liquid electrolyte are of great interest yielding excess of 3%[8, 119] efficiencies. Crystalline TiO_2 is well known as a wide-gap semiconductor, which is transparent for visible light, and as an n-type semiconductor with a large electron affinity, which is suitable for photocatalysis[120]. In dye-sensitized photovoltaic devices, TiO_2 serves as a transparent electron-acceptor and electron transporting layer[121]. Solid state organic photovoltaic devices containing an n-type TiO_2 layer have the potential to become alternative materials for producing solar energy converters[8, 119, 122, 123]. In the electrolyte cells charges are transferred by ionic transport which is controlled by diffusion, whereas electronic transport is influenced by conductivity and charge transport mobility in p-type semiconductor cells. Another important difference between these two cells exists at the interface between the hole transport medium and the transparent working electrode FTO. In the electrolyte cell, the iodine/iodide has a strong overpotential at this interface. To prevent the photo generated charges from recombination at the boundary a barrier layer exists. In the solid state cell, low molecular weight spiro compounds such as spiro-OMeTAD or hole conducting polymers such as poly (3-hexylthiophene) (P3HT) and FTO form an ohmic contact resulting in charge recombination at this interface. Therefore a blocking layer is required to avoid short circuiting and current loss through recombination at the FTO electrode. A compact TiO_2 layer between FTO and nanocrystalline TiO_2 layer has been applied and its effect as increase in some orders of magnitude in efficiency has been observed[8, 9].

A solid state Grätzel solar cell representing its different layers is shown in Scheme 6.1. In this cell, FTO is the conducting electrode which is transparent to let the light reach dye-TiO_2 junctions. The compact TiO_2 layer acts as the blocking layer to prevent holes formed in the dye or hole transport layer from reaching the lower FTO which would otherwise short circuit the cell. Nanocrystalline TiO_2 layer has a porous structure that enlarges the surface area. Thus, most of the light can be absorbed, reflected and absorbed again, resulting in maximum light harvesting. Moreover, nanocrystalline TiO_2 layer is a network enabling the transferred electrons to reach the anode. A molecular layer of ruthenium dye (Ru-dye) is chemisorbed on nanocrystalline TiO_2 surface. A heterojunction is formed, and functions as the interface for separation of charges from formed excitons. Charge separation occurs at this interface, electron is transferred to TiO_2 and the hole in dye is compensated by electron transfer from hole transport layer, as depicted in enlarged drawing in Scheme 6.1.
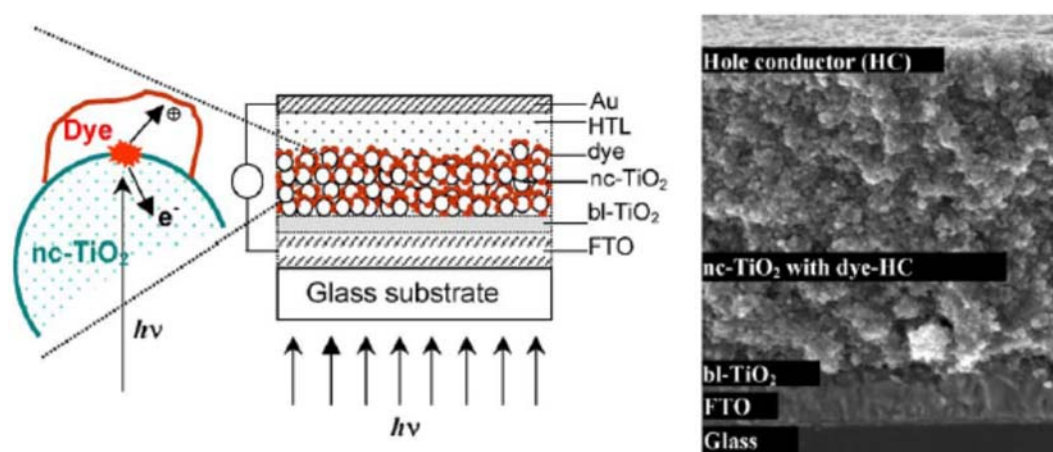
Scheme 6.1. *Schematic description (left) and SEM cross-section (right) of different layers in a solid state dye sensitized nanocrystalline TiO_2 solar cell. Transparent anode FTO is covered by a blocking TiO_2 layer (bl- TiO_2) to avoid recombination and short circuiting. Nanocrystalline TiO_2 layer (nc-TiO_2) has a large surface area where a mono molecular layer of Ru-dye is chemisorbed, and light harvesting and charge separation occurs at this heterojunction. Separated electrons and holes are conducted through TiO_2 to the FTO-anode and through the organic hole transport layer (HTL) to the Au-cathode, respectively[13].*

Our aim is to replace the compact TiO_2 blocking layer in solid state dye sensitized solar cells. In Chapter 5.2.1, it is shown that our integrated blocking layer functions as desired; charge percolation pathways exist with insulating SiOC parts in between. With this blocking layer,

nanocrystalline TiO_2 layer and TiO_2 blocking layer are combined in one, and tested in prepared solar devices. Our solar device is shematicly described in Scheme 6.2.
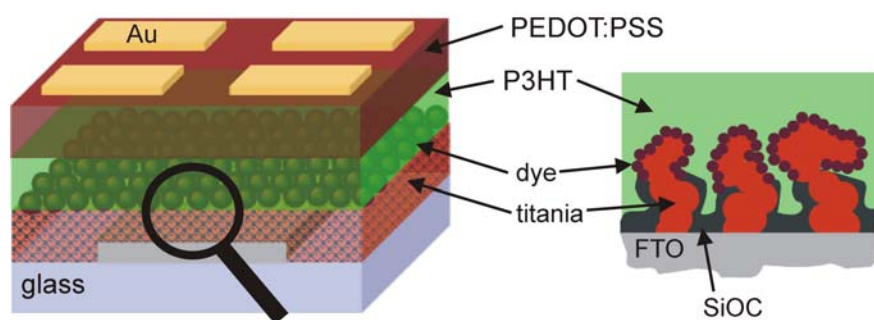
Scheme 6.2. *Schematic description of our solid state dye sensitized solar cell[124].*

6.1 Solar device preparation

Solar device preparation starts from FTO anode and proceeds layer by layer to Au cathode. FTO on glass substrate is cleaned in several steps. First the substrate is rinsed with a cleaning detergent-water mixture (Alconox-water) followed by rinsing with de-ionized water in order to remove any residual Alconox. Afterwards, the substrate is rinsed successively with acetone, ethanol and isopropanol and put for 15 minutes in isopropanol in an ultrasonic bath. The substrate is then dried with an argon-jet. The final cleaning step is performed in an oxygen-plasma chamber for 10 minutes.

After cleaning of FTO, preparation proceeded step by step as schematically presented in Scheme 6.1.1. The solution for the spin-coating of the titania/(PEO)MA-PDMS-MA(PEO) nanocomposite film was prepared by the following the same procedure of 1 % HCl containing series (Chapter 5.1.1). The prepared solution was stirred for one hour. The titania/(PEO)MA-PDMS-MA(PEO)nanocomposite film was prepared on top of the pre-cleaned FTO by spin-coating the solution for 60 s at 2000 rpm rotational speed under ambient conditions, resulting in 40 nm thick nanocomposite film. Argon plasma treatment was applied at 0.2 mbar and 300 W for 10 minutes. The calcination of the film was carried out at 450°C for 4 h in nitrogen atmosphere at a heating rate of 6.25°C/min. After calcination, the sample was left inside the furnace to cool down, and the thickness of the integrated blocking layer was 20 nm.

In the next step, the titania nanostructures were dye-coated by immersing them into a 0.3 mmol l^{-1} solution of dye Z-907 in CH$_3$CN and t-butanol (volume ratio 1:1) at room temperature for 12 hours[125]. The remaining solution was removed from the surface and before spin-coating poly(3-hexylthiophene) (P3HT) (American Dye Source Inc.) the samples were washed with ethanol. With spin-coating of P3HT and subsequent annealing at 200°C for 2h the photoactive layer of the device is prepared. The P3HT thickness was determined to be 40 nm. In the final steps poly(3,4-ethylenedioxythiophene):poly(styrenesulfonate) (PEDOT:PSS) (Baytron P., Bayer) is spin-coated on the underlying P3HT and also annealed at 100°C for 15 min. A PEDOT:PSS thickness of 87 nm was obtained. At last, gold layer with a thickness of 100 nm was deposited on top of the PEDOT:PSS layer by thermal evaporation (Leybold-Heraeus Univex 300 evaporator). PEDOT:PSS layer was put to block any electron migration to the counter Au electrode.

After each preparation step samples were imaged by SEM (Figure 6.1.1).
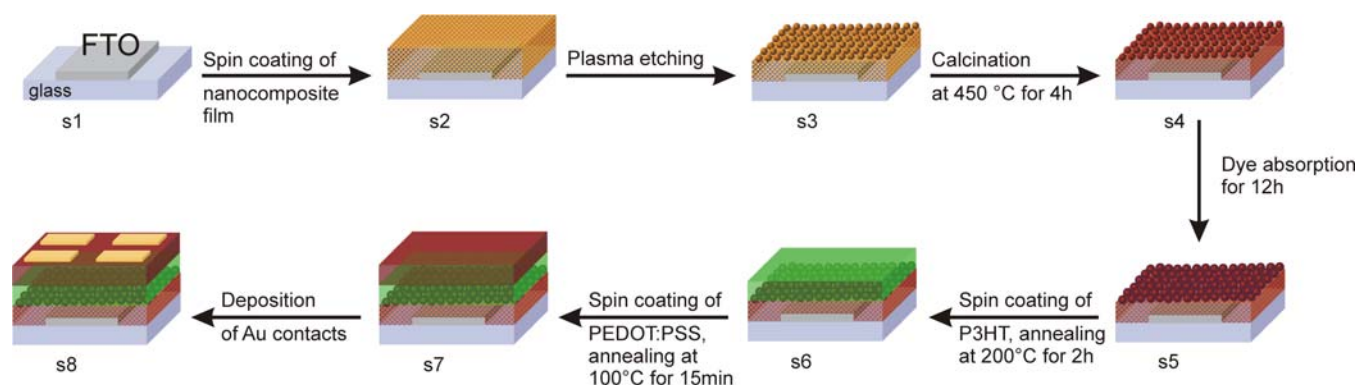
Scheme 6.1.1. *Preparation steps of solid state dye sensitized solar cell. Bare FTO (s1), titania/(PEO)MA-PDMS-MA(PEO) nanocomposite film (s2), after plasma treatment (s3), after annealing at 450°C under nitrogen (s4), after dye absorption (s5), after P3HT coating and annealing (s6), after PEDOT:PSS coating and annealing (s7)[124].*
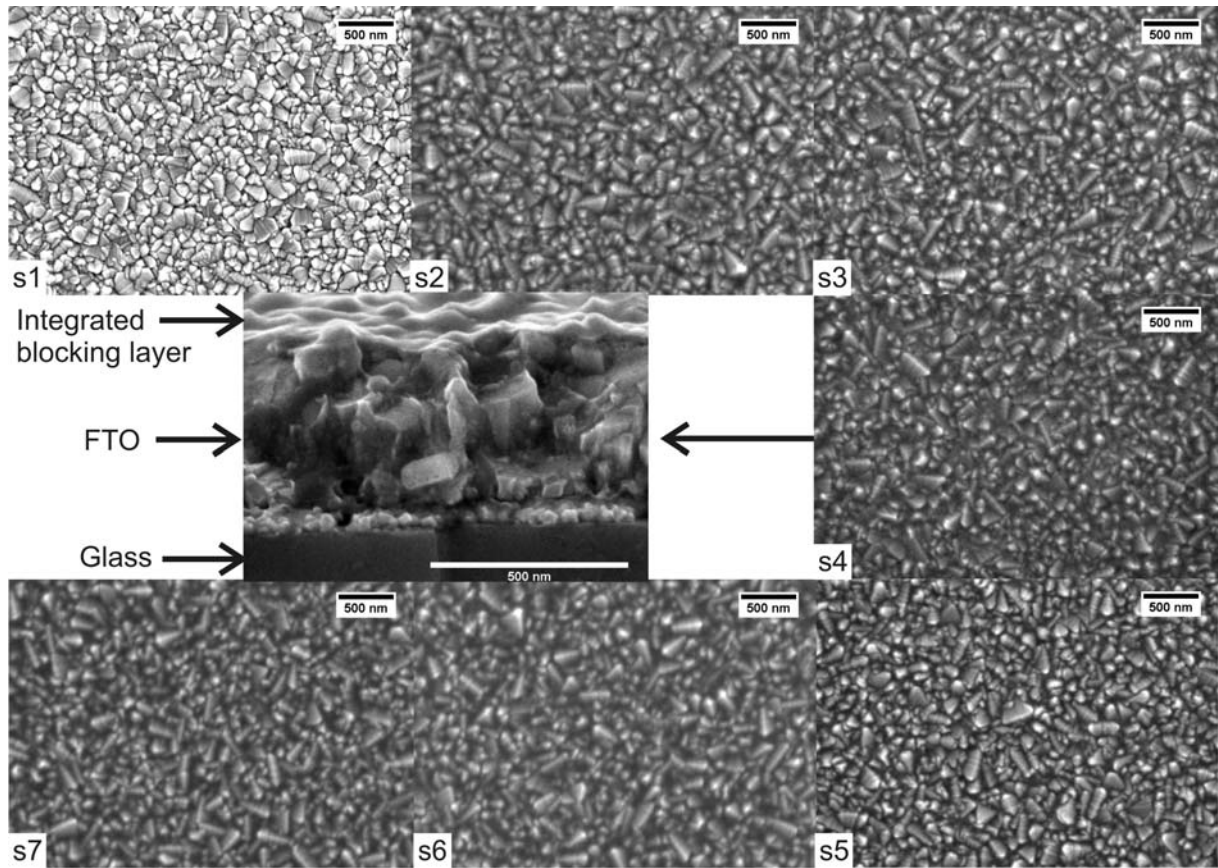
Figure 6.1.1. SEM images (top view) of bare FTO (s1), titania/(PEO)MA-PDMS-MA(PEO) nanocomposite film (s2), after plasma treatment (s3), after annealing at 450°C under nitrogen (s4), after dye absorption (s5), after P3HT coating and annealing (s6), after PEDOT:PSS coating and annealing (s7). Next to (s4), SEM image from side view of (s4)-integrated blocking layer is seen as a continous layer over FTO.

Tin oxide crystals resulting in the rough surface of FTO, (s1), can be recognized below the titania/(PEO)MA-PDMS-MA(PEO) nanocomposite film of thickness 40 nm (s2). Plasma etching and calcination reduce the thickness to 20 nm, and dye is absorbed as a monolayer; view from top does not change (s3), (s4), (s5), respectively. Comparatively thicker layers of P3HT (40 nm) and PEDOT:PSS (85 nm) do not alter the view from above (s6), (s7). The side view of the integrated blocking layer on FTO is shown next to its top view. Blocking layer forms a continuous layer on FTO following the structure of tin oxide crystals. Glass substrate below FTO is also pointed to correlate schematic representation with the corresponding SEM image.

A closer image of the integrated blocking layer was obtained by making a cut by FIB, and imaging the cut by SEM (Figure 6.1.2). To protect the thin film from any possible damage

115

during milling by Ga^+ ions, 100 nm thick Pt was deposited. The cut was cleaned by milling with very low beam current, and the cut was imaged by SEM. Conducting Pt and FTO appear as bright on the image. Integrated barrier layer is darker compared to them. Some whitish parts can be seen along the barrier layer indicating semiconducting titania parts.
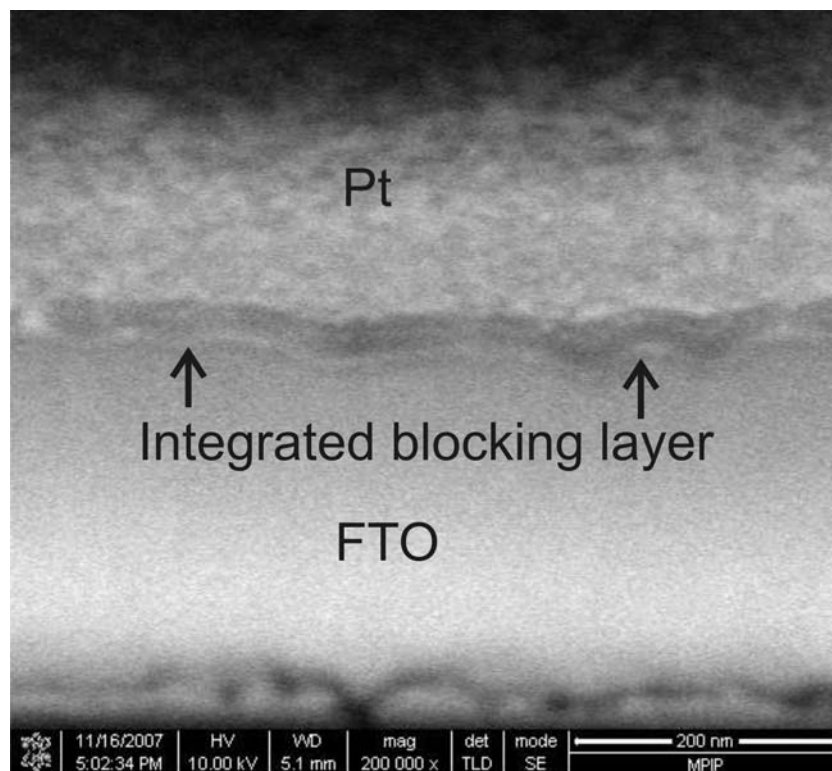
Figure 6.1.2. SEM image from a FIB cut in integrated blocking layer, (s4) in above illustrations. Continuous barrier layer on FTO is seen as grayish layer between FTO and Pt.

To compare our blocking layer with conventional compact TiO_2 blocking layer a series of solar devices was prepared. After each step samples were imaged by SEM (Fig. 6.1.2). Conventional compact TiO_2 blocking layer was prepared according to litearture[126], stirred for 3 days, spin coated and calcined at 450°C for 15 min. Then nanocrystalline TiO_2 layer (Tinanox-t, Solaronix) was blade coated and heated at 450°C for 15 min. The same procedure as previous series to prepare remaining P3HT, PEDT:PSS and Au layer was repeated. Conventional TiO_2 blocking layer was ~40 nm thick. Some surface defects are observed (Fig.6.1.2-b) through the blocking layer. Ti-Nanoxide-T nanocrystalline layer is seen in Figure 6.1.2-c, and since does not change after dye absorption (Fig.6.1.2-d). After P3HT coating some regions are observed darker (Fig.6.1.2-e). P3HT polymer is not small to penetrate

116

through crystalline it accumulated on some parts. Comparatively thicker PEDOT:PSS layer prevented seeing the nanocrystalline titania layer (Fig.6.1.2-f).
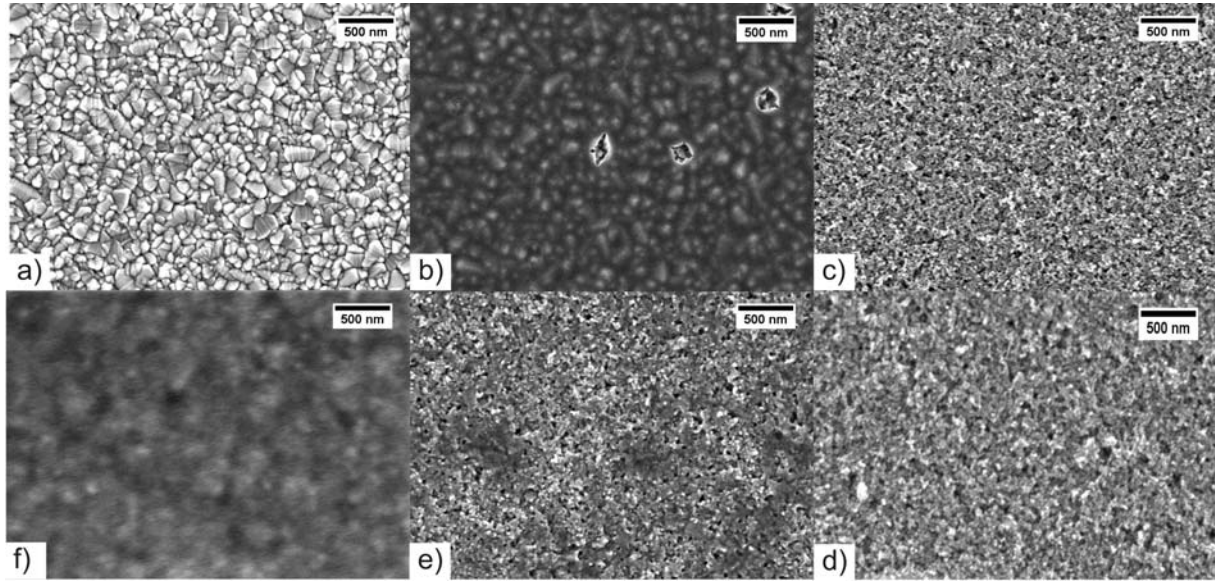
Figure 6.1.2. SEM images (top view) of bare FTO (a), after conventional TiO$_2$ blocking layer (b), after Ti-nanox-T nanocrystalline layer (c), after absorption of dye (d), after P3HT layer (e), after PEDOT:PSS layer(f).

6.2   Solar device performance measurement

The efficiency of solar cells is calculated from its current-voltage (*I-V*) measurement. *I-V* characteristics of a solar cell in the dark and under illumination are shown in Figure 6.2.1. There is almost no current flowing in the dark until the contacts start to inject at forward bias for voltages larger than the open circuit voltage (*V$_{oc}$*). Under illumination solar cell generates power between (a) and (b). The current and voltage product is largest at the maximum power point (MPP)[127].

Photovoltaic power conversion efficiency of a solar cell is determined by

$$\eta_e = \frac{V_{oc} \times I_{sc} \times FF}{P_{in}} \text{ with } FF = \frac{I_{mpp} \times V_{mpp}}{I_{sc} \times V_{oc}} \qquad \text{Eqn.6.2.1.}$$

where *V$_{oc}$* is the open circuit voltage, *I$_{sc}$* is the short circuit current, *FF* is the fill factor, *P$_{in}$* is the incident light power density, *I$_{mpp}$* and *V$_{mpp}$* are the current and voltage at the maximum power point. The light intensity is standardized at 1000 W/m^2 with a spectral intensity

117

distribution matching that of the sun on earth's surface at an incident angle of 48.2°, which is called the AM 1.5 spectrum[128].
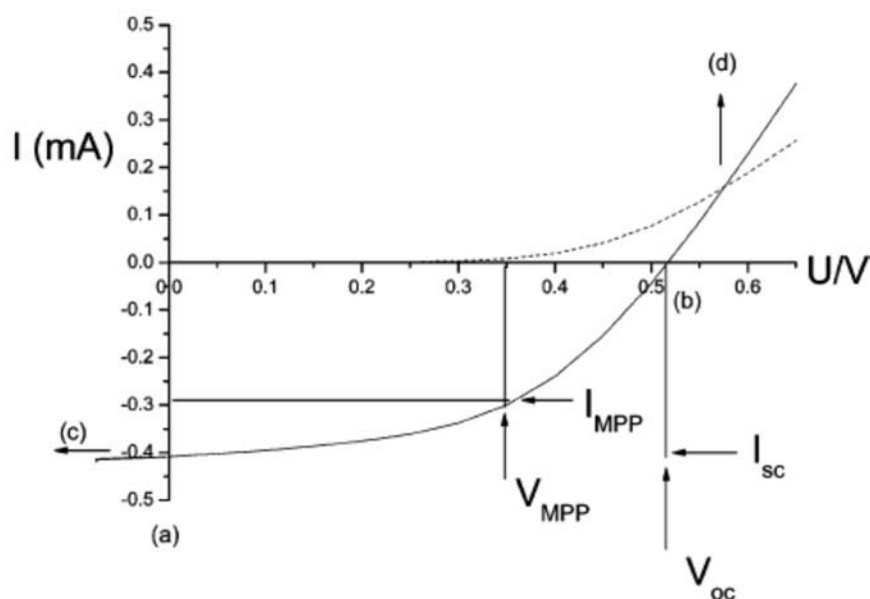
Figure 6.2.1. *Current-voltage (I-V) curves of an organic solar cell (dark-dots; illuminated-solid line). The intersection with the abscissa is the open circuit voltage (V_{oc}) and that with ordinate is the short circuit current (I_{sc}). The largest power output (P_{max}) is determined by the point where the product of voltage and current is maximized. Division of P_{max} by the product of I_{sc} and V_{oc} gives the fill factor FF[115].*

Although the V_{oc} of a metal-insulator-metal device is determined by the difference in work functions of the two metal cotacts[2], in a p-n junction V_{oc} is determined by the difference of the quasi Fermi levels of the two charge carriers; n-doped and p-doped semiconductor energy levels. In organic solar cells, V_{oc} depends on the highest occupied molecular orbital HOMO level of the donor (p-type semiconductor quasi Fermi level) and lowest unoccupied molecular orbital LUMO level of the acceptor (n-type semiconductor quasi Fermi level)[129, 130].

In ideal case when there is no loss at the contacts, the short circuit current, I_{sc}, is determined by the product of charge carrier density and the charge carrier mobility within the organic semiconductors;

$$I_{sc} = ne\mu E$$

Eqn.6.2.2.

where n is the charge carrier density, e is the elementary charge, μ is the mobility, and E is the electric field.

The incident photon to current efficiency or external quantum efficiency (EQE) is the number of electrons collected under short circuit conditions, divided by the number of incident photons,

$$EQE = \frac{1240 I_{sc}}{\lambda P_{in}}$$

Egn.6.2.3

where λ (nm) is the incident photon wavelength, I_{sc} ($\mu a/cm^2$) is the photocurrent of the device and P_{in} (W/m^2) is the incident power.

Prepared solar cells' performance was recorded with a Keithley 236 Source-Measure Unit. Light source was a Tungsten-halogen lamp generating monochromatic light in range 300-700 nm through a TRIAX 180 monochromator. Incident light intensity was determined by a calibrated silicon diode. The maximum intensity was 6 W/cm^2 at 600nm.

The open circuit values and corresponding efficiencies of solar devices prepared by our integrated blocking layer are measured for each pixel and given in Table 6.2.1. Preparation takes 7 steps as schematically shown in Scheme 6.1.1. Perlich et al. have recently showed perseverance of TiO_2 nanoparticle morphology after spin-coating of the integrated blocking layer (Scheme 6.1.1.s2-s8) by μGISAXS measurements[124]. Corresponding SEM images after each step (Fig. 6.1.1) also shows the uniformity of each layer. Although our solar cells were prepared by uniform and crack free layers, only 52% of the prepared pixels worked. For comparison of the blocking layers, solar cells were also prepared with conventional TiO_2 blocking layer, and performances of those devices are given in Table 6.2.2, where 42% of the pixels worked. The highest efficiency with highest open circuit voltage of integrated blocking layer device was 15 times larger than that of conventional blocking layer containing device. The *I-V* curves of these samples are shown in Figure 6.2.1.

The compared devices differ on type of blocking and crystalline TiO_2 layers. Integrated blocking layer contains both layers in a ~20 nm layer, whereas a micron thick nanocrystalline TiO_2 layer exists over conventional TiO_2 blocking layer (thickness ~40 nm). The difference in the nanocrystalline TiO_2 layer thickness can not be the reason for the poor behavior of conventional TiO_2 blocking layer containing solar cell since nanocrystalline TiO_2 layer is usually prepared in >2μm thickness. The drawback for both devices is that P3HT can not

119

penetrate in between nanocrystalline TiO_2 particles as a small molecule. This may result in a poor interface between nanocrystalline TiO_2/dye and the hole conducting polymer. However in our integrated blocking layer the thickness is thin enough for all titania/dye junctions to be covered by P3HT, since they are all on the surface, and these titania are connected to the FTO while there is insulation by SiOC to prevent the direct contact between FTO and P3HT.

V_{oc} (V)	η_e%	% pixels (out of 120)
0.42	0.003	3
0.07	0.0015	2
0.06	0.0003	2
0.05	0.00055	3
0.04	0.0005	3
0.02	0.0003	5
0.01	0.0003	6
0.01	0	28
did not work	-	48

Table 6.2.1. *Performance values of solar cells prepared by using integrated blocking layer.*

V_{oc} (V)	η_e%	% pixels (out of 60)
0.05	0.0002	3
0.01	0.0001	19
0.01	0	20
did not work	-	58

Table 6.2.2. *Performance values of solar cells prepared by usingconventional blocking layer.*
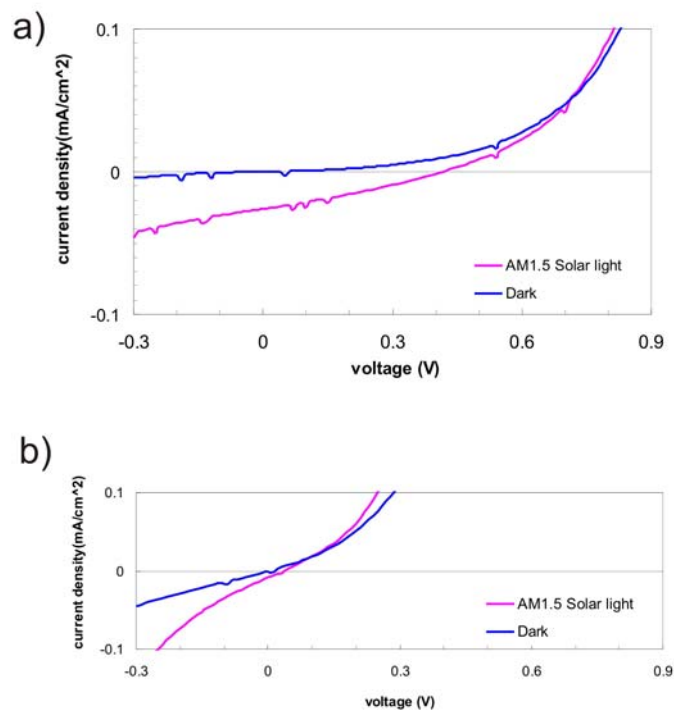
Figure 6.2.1. *I-V curves of solar cells prepared by integrated blocking layer (left) and conventional TiO$_2$ blocking layer (right).*

The interfaces are very important in solar cells. Charge separation occurs at the dye-nanocrystalline TiO$_2$ interface. Electrons move through TiO$_2$ to TiO$_2$-FTO interface, and then holes are compensated by the P3HT-dye interface behind which P3HT-PEDOT:PSS and PEDOT:PSS –Au interfaces exist. To make these interfaces more suitable for charge flow, effect of different solvent for preparation of each layer and different annealing temperatures can be tried.

We have shown in Chapter 5.2.1 that charge percolation pathways exist thorough our integrated blocking layer. The surface of our integrated blocking layer is predominantly composed of TiO$_2$ which is suitable for dye absorption in solar cell applications. In this Chapter, application in solar cells by comparing with conventional TiO$_2$ blocking layer is shown. Hybrid organic solar cells prepared by our integrated blocking layer showed 15 times higher efficiencies compared to conventional TiO$_2$ blocking layer solar cells. This points the great potential for application of our integrated blocking layer in hybrid organic solar cells.

7 Summary and Outlook

An integrated blocking layer for hybrid organic solar cells has been developed. The existence of an electrically conductive network of titania particles having an insulating layer in between has been shown by scanning conductive probe microscopy. Titania particles form charge percolation pathways from surface to the substrate while silicon oxycarbide matrix prevents direct contact of the anode (FTO) with hole conducting medium to avoid short circuiting and current loss through recombination at the FTO electrode. The surface of our integrated blocking layer is predominantly composed of TiO_2 as shown by scanning Kelvin probe force microscopy. This makes surface of the prepared blocking layer suitable for dye absorption thus forming the interface for charge separation. Application in solar devices by comparing with conventional TiO_2 blocking layer showed 15 times higher efficiencies. FIB cut through prepared blocking layer on FTO showed the continuous coverage of FTO surface by the blocking layer. µGISAXS interpretation with the Unified Fit model revealed presence of primary titania structures and clusters formed from these particles in correlation with microscopy images.

For the preparation of the integrated blocking layer a novel (PEO)MA-PDMS-MA(PEO) triblock copolymer has been synthesized. This triblock copolymer has a hexagonally packed cylindrical morphology at room temperature and preserves this ordered phase for a long temperature range as observed from rheology measurements. The cylindrical morphology in bulk is the good starting point for creating titania particles via sol-gel chemistry where the amphiphilic block copolymer is the templating agent to form the percolation pathways. Thus, titania particles have been prepared by spin coating the sol-gel where (PEO)MA-PDMS-MA(PEO) was the templating agent. Morphological properties of the nanocomposite films were investigated by microscopy techniques. In the film preparation step, during spin coating liquid-liquid miscibility gap occurred which resulted in circular pits on the films. The surface information was correlated with interior information obtained from µGISAXS experiments. Plasma etching uncovered the titania surface from polymers before the heating step. Annealing the nanocomposite films at 450°C under nitrogen was enough to obtain anatase polymorph of titania and (PEO)MA-PDMS-MA(PEO) derived ceramic confirmed by XRD measurements and visual imaging, respectively.

The effects of the sol-gel composition and heating temperature elavation on the morphology of resultant titania nanoparticles were investigated. The increase in polymer content from 1%

to 2% resulted in worm like morphology with smaller primary titania particles having a diameter of ~13-15 nm which is in the order of exciton diffusion lengths. HCl concentration increase from 1% to 5% did not alter the morphology with a little increase in the diameter of the circular pits that were formed during spin-coating. Titania precursor increase from 1% to 2% has the same effect with HCl on morphology, however more titania content increased the packing density. Crystalline titania particles were imaged by TEM of 2% titania containing nanocomposite films after plasma treatment and heating at 450°C.

PDMS-MA(PEO) and PEO-MA(PDMS) diblock copolymers were also synthesized and their templating effect on titania particles were investigated. PEO-MA(PDMS) resulted in highly ordered morphology as evidenced by the peaks observed in scattering measurements. Microscopy images also showed foam like morphology.

Although we have prepared an alternative integrated blocking layer for titanium dioxide solar cell applications, there is still need for research to modify the titania particles morphology in a controlled way and investigate their effect on device efficiencies.

Sol-gel composition with 2% triblock copolymer resulted in titania particles on the order of exciton diffusion length (~15 nm) whose effects needs to be further investigated. Titania precursor increase should be optimized for optimum charge percolation pathways through the blocking layer. Primary results on sol-gel composition change on titania morphology needs to be broadened to obtain a phase diagram of (PEO)MA-PDMS-MA(PEO) triblock copolymer to obtain more information on behavior of the triblock copolymer in used sol-gel composition, to gain insight for the miscibility gap occurring during spin-coating due to liquid-liquid phase separation.

PEO-MA(PDMS) diblock copolymer resulted in ordered titania structures. Synthesis of well defined PEO-PDMS block copolymers in different architectures with tunable block lengths will broaden the obtained titania morphology, thus charge percolation length density in the integrated blocking layer.

Combination of different material properties, i.e. conduction and insulation, by using the self assembly of block copolymers to pattern nanostructures has been achieved in this thesis. This is a first accomplishment in production of an alternative blocking layer for hybrid organic solar cells where different properties are combined in nanoscale by means of an easy and reproducible way. Besides application in the research for new energy conversion methods, this nanocomposite layer may be promising in for biological applications, too. Recently uniform

titania coating on PDMS has been used to control bacterial adhesion and growth on the polymer surface and reduced adhesion of both Gram-negative and Gram-positive bacteria to modified surface[131]. Thus biological properties of our titania/PDMS containing amphiphilic block copolymers may be investigated which can be applicabled on variety of surfaces with presented easy preparation.

References

1   B. Oregan, and M. Grätzel, *Nature* **353**, (6346), 737-740 (1991).

2   I. D. Parker, *Journal of Applied Physics* **75**, (3), 1656-1666 (1994).

3   A. J. Heeger, I. D. Parker, and Y. Yang, *Synthetic Metals* **67**, (1-3), 23-29 (1994).

4   M. Adachi, J. Jiu, and S. Isoda, *Current Nanoscience* **3**, (4), 285-295 (2007).

5   C. Jager, R. Bilke, M. Heim, D. Haarer, H. Karickal, and M. Thelakkat, *Synthetic Metals* **121**, (1-3), 1543-1544 (2001).

6   J. Hagen, W. Schaffrath, P. Otschik, R. Fink, A. Bacher, H. W. Schmidt, and D. Haarer, *Synthetic Metals* **89**, (3), 215-220 (1997).

7   M. Thelakkat, J. Hagen, D. Haarer, and H. W. Schmidt, *Synthetic Metals* **102**, (1-3), 1125-1128 (1999).

8   U. Bach, D. Lupo, P. Comte, J. E. Moser, F. Weissortel, J. Salbeck, H. Spreitzer, and M. Grätzel, *Nature* **395**, (6702), 583-585 (1998).

9   J. Kruger, R. Plass, L. Cevey, M. Piccirelli, M. Gratzel, and U. Bach, *Applied Physics Letters* **79**, (13), 2085-2087 (2001).

10   J. Bandara, and H. Weerasinghe, *Solar Energy Materials and Solar Cells* **85**, (3), 385-390 (2005).

11   T. Osada, T. Kugler, P. Broms, and W. R. Salaneck, *Synthetic Metals* **96**, (1), 77-80 (1998).

12   J. C. Scott, J. H. Kaufman, P. J. Brock, R. DiPietro, J. Salem, and J. A. Goitia, *Journal of Applied Physics* **79**, (5), 2745-2751 (1996).

13   B. Peng, G. Jungmann, C. Jager, D. Haarer, H. W. Schmidt, and M. Thelakkat, *Coordination Chemistry Reviews* **248**, (13-14), 1479-1489 (2004).

14   X. Wang, L. J. Zhi, and K. Mullen, *Nano Letters* **8**, (1), 323-327 (2008).

15   J. Xia, N. Masaki, K. Jiang, and S. Yanagida, *Journal of Physical Chemistry B* **110**, (50), 25222-25228 (2006).

16   M. Paulose, K. Shankar, O. K. Varghese, G. K. Mor, and C. A. Grimes, *Journal of Physics D-Applied Physics* **39**, (12), 2498-2503 (2006).

17   A. Suisalu, J. Aarik, H. Mandar, and I. Sildos, *Thin Solid Films* **336**, (1-2), 295-298 (1998).

18   K. Baba, and R. Hatada, *Surface & Coatings Technology* **136**, (1-3), 241-243 (2001).

19   L. Gao, and Q. H. Zhang, *Scripta Materialia* **44**, (8-9), 1195-1198 (2001).

20   M. Gratzel, *Nature* **414**, (6861), 338-344 (2001).

21   K. M. Coakley, and M. D. McGehee, *Applied Physics Letters* **83**, (16), 3380-3382 (2003).

22   Z. S. Wang, H. Kawauchi, T. Kashima, and H. Arakawa, *Coordination Chemistry Reviews* **248**, (13-14), 1381-1389 (2004).

23   Y. J. Cheng, and J. S. Gutmann, *Journal of the American Chemical Society* **128**, (14), 4658-4674 (2006).

24   M. Templin, A. Franck, A. DuChesne, H. Leist, Y. M. Zhang, R. Ulrich, V. Schadler, and U. Wiesner, *Science* **278**, (5344), 1795-1798 (1997).

25   R. Ulrich, A. Du Chesne, M. Templin, and U. Wiesner, *Advanced Materials* **11**, (2), 141-146 (1999).

26   Z. C. Sun, and J. S. Gutmann, *Physica a-Statistical Mechanics and Its Applications* **339**, (1-2), 80-85 (2004).

27   Z. C. Sun, D. H. Kim, M. Wolkenhauer, G. G. Bumbu, W. Knoll, and J. S. Gutmann, *Chemphyschem* **7**, (2), 370-378 (2006).

28   F. W. G. F. J. M. Zeigler, *Silicon-based polymer science*. American Chemical Society: Washington, 1990; Vol. 224.

29   C. G. Pantano, A. K. Singh, and H. X. Zhang, *Journal of Sol-Gel Science and Technology* **14**, (1), 7-25 (1999).

30   N. Hadjichristidis, *Block copolymers : synthetic strategies, physical properties, and applications*. Wiley-Interscience: Hoboken, 2003; p 419.

31   F. S. Bates, *Science* **251**, (4996), 898-905 (1991).

32   P. J. Flory, *Principles of polymer chemistry*. Cornell University Press: Ithaca, 1992; p 672.

33   E. A. Guggenheim, *Thermodynamics*. 7th ed.; North-Holland: Amsterdam, 1985; p 390.

34   L. Leibler, *Macromolecules* **13**, (6), 1602-1617 (1980).

35   G. H. Fredrickson, and E. Helfand, *Journal of Chemical Physics* **87**, (1), 697-705 (1987).

36   U. Krappe, R. Stadler, and I. Voigtmartin, *Macromolecules* **28**, (13), 4558-4561 (1995).

37   A. M. Mayes, and M. O. Delacruz, *Journal of Chemical Physics* **91**, (11), 7228-7235 (1989).

38   M. Szwarc, *Nature* **178**, (4543), 1168-1169 (1956).

39   M. Szwarc, M. Levy, and R. Milkovich, *Journal of the American Chemical Society* **78**, (11), 2656-2657 (1956).

40   N. Hadjichristidis, H. Iatrou, S. Pispas, and M. Pitsikalis, *Journal of Polymer Science Part a-Polymer Chemistry* **38**, (18), 3211-3234 (2000).

41   D. Greszta, D. Mardare, and K. Matyjaszewski, *Macromolecules* **27**, (3), 638-644 (1994).

42   A. Goto, and T. Fukuda, *Progress in Polymer Science* **29**, (4), 329-385 (2004).

43   H. Fischer, *Chemical Reviews* **101**, (12), 3581-3610 (2001).

44   W. Tang, N. V. Tsarevsky, and K. Matyjaszewski, *Journal of the American Chemical Society* **128**, (5), 1598-1604 (2006).

45   W. Tang, T. Fukuda, and K. Matyjaszewski, *Macromolecules* **39**, (13), 4332-4337 (2006).

46   K. Matyjaszewski, *Current Organic Chemistry* **6**, (2), 67-82 (2002).

47   M. K. Georges, R. P. N. Veregin, P. M. Kazmaier, and G. K. Hamer, *Macromolecules* **26**, (11), 2987-2988 (1993).

48   C. J. Hawker, A. W. Bosman, and E. Harth, *Chemical Reviews* **101**, (12), 3661-3688 (2001).

49   B. B. Wayland, G. Poszmik, S. L. Mukerjee, and M. Fryd, *Journal of the American Chemical Society* **116**, (17), 7943-7944 (1994).

50   K. Matyjaszewski, and J. H. Xia, *Chemical Reviews* **101**, (9), 2921-2990 (2001).

51   J. W. M. H. G. Barth, *Modern methods of polymer characterization*. Wiley: New York 1991; p 561.

52 http://pslc.ws/macrog/dsc.htm

53 www.simex.com.mx/PDFS/orthon/Thermal%20Gravimetric%20Analysis%20brochure.pdf

54   W. Schärtl, *Light scattering from polymer solutions and nanoparticle dispersions*. Springer: Berlin, 2007; p 191.

55   P. S. G. F. N. Hadjichristidis, *Block copolymers : synthetic strategies, physical propeties, and applications* Wiley-Interscience: Hoboken, 2003; p 419

56   G. Floudas, R. Ulrich, and U. Wiesner, *Journal of Chemical Physics* **110**, (1), 652-663 (1999).

57   http://rsb.info.nih.gov/ij/, last access 11.07.2008

58   G. Binnig, C. F. Quate, and C. Gerber, *Physical Review Letters* **56**, (9), 930-933 (1986).

59   T. R. Albrecht, S. Akamine, T. E. Carver, and C. F. Quate, *Journal of Vacuum Science & Technology a-Vacuum Surfaces and Films* **8**, (4), 3386-3396 (1990).

60   S. N. Magonov, and D. H. Reneker, *Annual Review of Materials Science* **27**, 175-222 (1997).

61   http://www.di.com, last access 11.07.2008

62   H. O. Jacobs, H. F. Knapp, and A. Stemmer, *Review of Scientific Instruments* **70**, (3), 1756-1760 (1999).

63   M. D. Uchic, L. Holzer, B. J. Inkson, E. L. Principe, and P. Munroe, *Mrs Bulletin* **32**, (5), 408-416 (2007).

64   http://www.fibics.com/FIBBasics.html

65   T. P. Russell, *Materials Science Reports* **5**, 171-271 (1990).

66   M. F. Birkholz, Paul F. , *Thin Film Analysis by X-Ray Scattering*. Wiley-VCH: Weinheim, 2006; p 356.

67   O. K. O. Glatter, *Small angle X-ray scattering* Academic Press: London, 1982; p 515.

68   P. Debye, **46**, (1915).

69   P. Debye, Bueche, A.M.J., *Appl. Phys.* **20**, 518 (1949).

70   G. Porod, *Kolloid-Z.* **124**, 83 (1951).

71   L. Li, in *Fach Chemie der Fakultät für Biologie, Chemie und Geowissenschaften*, Universität Bayreuth: Bayreuth, 2005; p 126.

72   P. Müller-Buschbaum, *Analytical and Bioanalytical Chemistry* **376**, (1), 3-10 (2003).

73   www.gisaxs.de

74   http://staff.chess.cornell.edu/~smilgies/gisaxs/GISAXS.php

75   S. V. Roth, R. Dohrmann, M. Dommach, M. Kuhlmann, I. Kroger, R. Gehrke, H. Water, C. Schroer, B. Lengeler, and P. Müller-Buschbaum, *Review of Scientific Instruments* **77**, (8), (2006).

76   O. Rheingans, N. Hugenberg, J. R. Harris, K. Fischer, and M. Maskos, *Macromolecules* **33**, (13), 4780-4790 (2000).

77   N. Husing, B. Launay, J. Bauer, G. Kickelbick, and D. Doshi, *Journal of Sol-Gel Science and Technology* **26**, (1-3), 609-613 (2003).

78   G. Kickelbick, J. Bauer, N. Husing, M. Andersson, and A. Palmqvist, *Langmuir* **19**, (8), 3198-3201 (2003).

79   G. Kickelbick, J. Bauer, N. Huesing, M. Andersson, and K. Holmberg, *Langmuir* **19**, (24), 10073-10076 (2003).

80   J. L. Yang, and G. Wegner, *Macromolecules* **25**, (6), 1791-1795 (1992).

81   R. Stoenescu, in *Physical Chemistry*, Basel University: Basel, 2004; Vol. M.Sc., p 137.

82   T. N. Khan, R. H. Mobbs, C. Price, J. R. Quintana, and R. B. Stubbersfield, *European Polymer Journal* **23**, (3), 191-194 (1987).

83   K. Kim, K. E. Plass, and A. J. Matzger, *Journal of the American Chemical Society* **127**, (13), 4879-4887 (2005).

84   M. Rubinstein, Colby, R.H. , *Polymer Physics*. Oxford Univ. Press Oxford, 2003; p 440.

85   A. Ramakrishnan, R. Dhamodharan, and J. Ruhe, *Macromolecular Rapid Communications* **23**, (10-11), 612-616 (2002).

86   K. Huan, L. Bes, D. M. Haddleton, and E. Khoshdel, *Journal of Polymer Science: Part A: Polymer Chemistry* **39**, 1833-1842 (2001).

87   J. I. Brandrup, E. H.; Grulke, E. A. , *Polymer handbook*. 4th ed.; Wiley: New York, 1999.

88   P. J. Flory, Jackson, J. G. , Wood, C. J. , *Statistical mechanics of chain molecules* Hanser: München, 1989; p 432.

89   P. J. Flory, *Statistical mechanics of chain molecules* Interscience Publ.: New York 1969; p 432.

90   T. Dollase, H. W. Spiess, M. Gottlieb, and R. Yerushalmi-Rozen, *Europhysics Letters* **60**, (3), 390-396 (2002).

91   C. D. Han, D. M. Baek, J. K. Kim, T. Ogawa, N. Sakamoto, and T. Hashimoto, *Macrmolecules* **28**, (14), 5043-5062 (1995).

92   J. H. Rosedale, and F. S. Bates, *Macromolecules* **23**, (8), 2329-2338 (1990).

93   F. S. Bates, J. H. Rosedale, and G. H. Fredrickson, *Journal of Chemical Physics* **92**, (10), 6255-6270 (1990).

94   G. Floudas, N. Hadjichristidis, H. Iatrou, T. Pakula, and E. W. Fischer, *Macromolecules* **27**, (26), 7735-7746 (1994).

95   G. Floudas, R. Ulrich, U. Wiesner, and B. Chu, *Europhysics Letters* **50**, (2), 182-188 (2000).

96   Synthesized by Maria C. Lechmann.

97   M. Memesa, Y. J. Cheng, J. Perlich, P. Müller-Buschbaum, and J. S. Gutmann, *Synthesis and Reactivity in Inorganic Metal-Organic and Nano-Metal Chemistry* **37**, (5), 315-320 (2007).

98   M. Memesa, S. Weber, S. Lenz, J. Perlich, R. Berger, P. Müller-Buschbaum, J.S. Gutmann, *submitted* (2008).

99   J. S. Gutmann, P. Müller-Buschbaum, and M. Stamm, *Faraday Discussions*, (112), 285-297 (1999).

100   http://www.hmi.de/bensc/instrumentation/instrumente/v6/refl/parratt_en.htm

101   R. Grover, B. M. Carthy, Y. Zhao, G. E. Jabbour, D. Sarid, G. M. Laws, B. R. Takulpalli, T. J. Thornton, and D. Gust, *Applied Physics Letters* **85**, (17), 3926-3928 (2004).

102   S. N. Magonov, and N. A. Yerina, *Langmuir* **19**, (3), 500-504 (2003).

103   P. D. Cozzoli, A. Kornowski, and H. Weller, *Journal of the American Chemical Society* **125**, (47), 14539-14548 (2003).

104   R. Viswanathan, and M. B. Heaney, *Physical Review Letters* **75**, (24), 4433-4436 (1995).

105   J. Ravier, F. Houze, F. Carmona, O. Schneegans, and H. Saadaoui, *Carbon* **39**, (2), 314-318 (2001).

106   G. Beaucage, *Journal of Applied Crystallography* **28**, 717-728 (1995).

107   G. Beaucage, *Journal of Applied Crystallography* **29**, 134-146 (1996).

108   G. Beaucage, S. Rane, S. Sukumaran, M. M. Satkowski, L. A. Schechtman, and Y. Doi, *Macromolecules* **30**, (14), 4158-4162 (1997).

109   S. Rathgeber, T. Pakula, and V. Urban, *Journal of Chemical Physics* **121**, (8), 3840-3853 (2004).

110   A. I. Norman, D. L. Ho, A. Karim, and E. J. Amis, *Journal of Colloid and Interface Science* **288**, (1), 155-165 (2005).

111   S. V. Chavan, P. U. Sastry, and A. K. Tyagi, *Scripta Materialia* **55**, (6), 569-572 (2006).

112   B. C. Tappan, M. H. Huynh, M. A. Hiskey, D. E. Chavez, E. P. Luther, J. T. Mang, and S. F. Son, *Journal of the American Chemical Society* **128**, (20), 6589-6594 (2006).

113   S. di Stasio, J. B. A. Mitchell, J. L. LeGarrec, L. Biennier, and M. Wulff, *Carbon* **44**, (7), 1267-1279 (2006).

114   S. Lenz, Bonini, M., Nett, S.H., Memesa, M., Timmann, A., Roth, S.V., Gutmann, J.S., (2008).

115   S. Gunes, H. Neugebauer, and N. S. Sariciftci, *Chemical Reviews* **107**, (4), 1324-1338 (2007).

116   R. Nakamura, T. Okamura, N. Ohashi, A. Imanishi, and Y. Nakato, *Journal of the American Chemical Society* **127**, (37), 12975-12983 (2005).

117   Y. J. Cheng, S. Y. Zhou, and J. S. Gutmann, *Macromolecular Rapid Communications* **28**, (13), 1392-1396 (2007).

118   L. B. Roberson, M. A. Poggi, J. Kowalik, G. P. Smestad, L. A. Bottomley, and L. M. Tolbert, *Coordination Chemistry Reviews* **248**, (13-14), 1491-1499 (2004).

119   J. Kruger, R. Plass, M. Gratzel, and H. J. Matthieu, *Applied Physics Letters* **81**, (2), 367-369 (2002).

120   A. Fujishima, T. N. Rao, and D. A. Tryk, *Electrochimica Acta* **45**, (28), 4683-4690 (2000).

121   E. Itoh, Y. Takamizawa, and K. Miyairi, *Japanese Journal of Applied Physics* **47**, (1), 509-512 (2008).

122   A. J. Breeze, Z. Schlesinger, S. A. Carter, and P. J. Brock, *Physical Review B* **6412**, (12), (2001).

123   J. Drechsel, B. Mannig, F. Kozlowski, D. Gebeyehu, A. Werner, M. Koch, K. Leo, and M. Pfeiffer, *Thin Solid Films* **451-52**, 515-517 (2004).

124   J. Perlich, Memesa, M., Diethert, A., Metwalli, E., Wang, W., Roth, S.V., Timmann, A., Gutmann, J.S., Müller-Buschbaum, P., *submitted* (2008).

125   P. Wang, Zakeeruddin, S. M., Moser, J. E., Nazeeruddin, M. K., Sekiguchi, T., Grätzel, M. , *Nature Materials* **2**, 402-408 (2002).

126   C. D. Grant, A. M. Schwartzberg, G. P. Smestad, J. Kowalik, L. M. Tolbert, and J. Z. Zhang, *Synthetic Metals* **132**, (2), 197-204 (2003).

127   H. Hoppe, and N. S. Sariciftci, *Journal of Materials Research* **19**, (7), 1924-1945 (2004).

128 J. Rostalski, and D. Meissner, *Solar Energy Materials and Solar Cells* **63**, (1), 37-47 (2000).

129 C. J. Brabec, A. Cravino, D. Meissner, N. S. Sariciftci, T. Fromherz, M. T. Rispens, L. Sanchez, and J. C. Hummelen, *Advanced Functional Materials* **11**, (5), 374-380 (2001).

130 M. C. Scharber, D. Wuhlbacher, M. Koppe, P. Denk, C. Waldauf, A. J. Heeger, and C. L. Brabec, *Advanced Materials* **18**, (6), 789-+ (2006).

131 O. Girshevitz, Y. Nitzan, and C. N. Sukenik, *Chemistry of Materials* **20**, (4), 1390-1396 (2008).

Declaration / Erklärung

English

I hereby declare that the thesis at hand has been written by myself without any impermissible help of others, that it contains no material of any other publications, and that due reference is made to all resources and literature.

Deutsch

Ich erkläre hiermit, daß die vorliegende Dissertation vor mir selbst und ohne unzulässige Hilfe Dritter verfaßt wurde, daß sie auch in Teilen keine Kopie anderer Arbeiten darstellt und die benutzten Hilfsmittel sowie die Literatur volständig angegeben sind.

Mainz, 17.09..2008

_____

Mine Memeşa